# Temperature Dependent Electrical Properties of Kesterite Monograin Layer Solar Cells

MATI  DANILSON

TALLINN UNIVERSITY OF TECHNOLOGY
Faculty of Chemical and Materials Technology
Department of Materials Science
Chair of Semiconductor Materials Technology

Dissertation was accepted for the defence of the degree of Doctor of Philosophy in Natural and Exact Sciences on May 24, 2016

**Supervisor:**     Professor Jüri Krustok, Department of Materials Science, Tallinn University of Technology, Estonia

**Opponents:**     Dr. Michael V. Yakushev, Department of Physics, University of Strathclyde, Glasgow, U.K.

Dr. Souhaib Oueslati, crystalsol OÜ, Tallinn, Estonia

**Defence:**     May 24, 2016, at 11.00
Lecture hall: U06A-201
Tallinn University of Technology,
Ehitajate tee 5, Tallinn

Declaration: Hereby I declare that this doctoral thesis, my original investigation and achievement, submitted for the doctoral degree at Tallinn University of Technology, has not been submitted for doctoral or equivalent academic degree.

Mati Danilson

# Kesteriitsete monoterakihiliste päikesepatareide elektriliste omaduste temperatuursõltuvused

MATI  DANILSON

# TABLE OF CONTENTS

## LIST OF PUBLICATIONS

The thesis is based on the following papers, which are referred to in the text by Roman numerals **I-III**:

I.   J. Krustok, R. Josepson, M. Danilson, D. Meissner, Temperature dependence of $Cu_2ZnSn(Se_xS_{1-x})_4$ monograin solar cells, Solar Energy 84 (2010) 379-383.
II.  J. Krustok, R. Josepson, T. Raadik, M. Danilson, Potential fluctuations in $Cu_2ZnSnSe_4$ solar cells studied by temperature dependence of quantum efficiency curves, Physica B 405 (2010) 3186-3189.
III. M. Danilson, E. Kask, N. Pokharel, M. Grossberg, M. Kauk-Kuusik, T. Varema, J.Krustok, Temperature dependent current transport properties in $Cu_2ZnSnS_4$ solar cells, Thin Solid Films 582 (2015) 162-165.

## AUTHOR'S OWN CONTRIBUTION

The contribution by the author to the papers included in the thesis is as follows:

- Temperature and light dependent current-voltage measurements, analysis, minor part of writing
- Temperature dependent quantum efficiency measurements, analysis, minor part of writing
- Temperature dependent current-voltage and quantum efficiency measurements, analysis, major part of writing

Materials, devices, chemical and thermal treatments, SEM, XRD, EDX, PL and Raman spectroscopic measurements were done by co-workers.

# LIST OF ABBREVIATIONS AND SYMBOLS

| | |
|---|---|
| AM1.5G | air mass 1.5 global |
| CIGS | $Cu(In,Ga)(S,Se)_2$ |
| CZTS | $Cu_2ZnSnS_4$ |
| CZTSe | $Cu_2ZnSnSe_4$ |
| CZTSSe | $Cu_2ZnSn(S_xSe_{1-x})_4$ |
| $E_A$ | activation energy |
| EDX | energy dispersive X-ray analysis |
| $E_g$ | band gap energy |
| $E_g^*$ | effective band gap energy |
| ES-VRH | Efros-Shklovskii variable-range hopping |
| EQE | external quantum efficiency |
| $FF$ | fill factor |
| $G$ | generation rate, shunt conductance |
| $J_0$ | saturation current density |
| $J_{00}$ | saturation current density prefactor |
| $J_D$ | diode current density |
| $J_{MPP}$ | current density at the point of maximum power |
| $J_{ph}$ | photo-generated current density |
| $J_{sc}$ | short-circuit current density |
| J-V | current density-voltage |
| $k$ | Boltzmann constant |
| MGL | monograin layer |
| M-VRH | Mott variable-range hopping |
| $n$ | ideality factor |
| NNH | nearest-neighbour hopping |
| $P_{AM1.5}$ | incident light power at AM1.5 illumination |
| $P_{MPP}$ | maximum output power |
| PV | photovoltaic |
| $q$ | elementary charge |
| $R_S$ | series resistance |
| $R_{sh}$ | shunt resistance / parallel resistance |
| $T$ | temperature |
| $V_{oc}$ | open-circuit voltage |
| $V_{MPP}$ | voltage at the point of maximum power |
| XRD | X-ray diffraction analysis |
| $\gamma$ | average depth of potential fluctuations |
| $\eta$ | efficiency |
| $\lambda$ | wavelength |
| $\Phi$ | integral of the quantum efficiency |
| $\sigma$ | steepness parameter, conductivity |

# INTRODUCTION

There is a growing need for energy in the world and since the traditional energy sources based on fossil fuels are limited and will be exhausted in the future, solar energy conversion by photovoltaic (PV) is considered as a promising candidate for an energy source. One way of solar energy direct conversion into electricity is by using the photovoltaic effect in a semiconductor device that is called a solar cell. A basic process behind the photovoltaic effect, on which the operation of solar cells is based, is the generation of the electron-hole pairs due to the absorption of visible or other electromagnetic radiation by a semiconductor material, also called as an absorber material. The generated electron-hole pairs are then separated by the *p-n* junction.

The main obstacle for broad solar energy use is the price of the solar cells. However, in today's conditions, the abundance of elements to be contained in the materials used to produce solar cells is of essential importance. As the share of the PV energy among the traditional world's energy sources grows, more material is needed to produce PV modules for large-scale terrestrial applications. To reduce the amount of active material in a cell, from the late 1970s, thin film technologies have been introduced. There are three main thin film technologies commercially available: cadmium telluride (CdTe), copper indium gallium diselenide (CIGS), and amorphous thin film silicon (a-Si). Regardless of thin film technology advances, the conventional crystalline silicon technology is dominating at 93% of the market-share and is projected to remain through 2019 [1]. Though a majority of thin film panels have 2 – 3 percentage points lower conversion efficiencies than crystalline silicon, the usage of rare elements as tellurium and indium may also become a limiting factor to the industrial scalability of CdTe and CIGS. For that reason, new cost-effective processes and materials are needed. One of the alternatives could be so-called kesterite based solar cells: $Cu_2ZnSn(S_xSe_{1-x})_4$ ($0 \leq x \leq 1$). A promising approach for the production of the kesterite absorber materials for solar cell applications is the monograin layer (MGL) solar cell technology. The principle of using unisize powder particles to form a single layer membrane for the PV application was proposed almost 50 years ago by the studies of the Philips company [2, 3]. The MGL consists of a thick layer of monograin powder grains embedded into an organic resin. The MGL solar cell technology combines the advantages of high quality absorber material production and device assembly with continuous throughput capability by using roll-to-roll technology [4]. The main advantages of MGL solar cell technology are relatively low production costs and the potential of covering unlimited areas [5].

Regardless of efforts, the performance of current kesterite solar cells lags essentially behind its predecessor and the main competitive material CIGS. Narrow phase stability, existence of competitive secondary phases and defects are reported as the main factors that constrain the target efficiency of $Cu_2ZnSn(S_xSe_{1-x})_4$ solar cells. As a result, structural inhomogeneity, local

fluctuations of open-circuit voltage and high carrier recombination rate finally lead to poor device performance and repeatability issues [6]. Almost all basic solar cell parameters are limited by recombination and parasitic losses. It is known that several semiconductor properties as well as semiconductor junction properties are dependent on temperature.

For deeper understanding of these different influences on the PV properties of kesterite MGL solar cells, detailed investigations of the current-voltage and quantum efficiency temperature and light intensity dependences have been conducted in this thesis. Quantum efficiency can be used to determine optical losses, optical enhancements, and voltage-dependent photocurrent mechanisms. Current-voltage measurements can be used to separate diode and parasitic effects.

The studied compounds are $Cu_2ZnSn(S_{0.7}Se_{0.3})_4$ [I], $Cu_2ZnSnSe_4$ [II] and $Cu_2ZnSnS_4$ [III]. In papers [I, III], temperature and illumination intensity dependent current-voltage analysis were performed to evaluate the dominating recombination processes and the behaviour of solar cell parameters as a function of temperature. In papers [II, III], we used temperature dependent external quantum efficiency to evaluate effective band gap energy and its temperature behaviour and also to study spatial potential fluctuations in compensated absorber materials.

# 1. LITERATURE REVIEW AND AIM OF THE STUDY

## 1.1 Solar cells

Solar cells are the only devices capable of direct light energy conversion into electricity without any interim steps. Solar cells are also called photovoltaic cells according to the phenomenon called photovoltaic effect. Photovoltaic effect is a physical phenomenon whereby voltage or electric current is created in a material upon exposure to light [7]. The conversion is accomplished by absorbing light and generating either electron-hole pairs or excitons. Then the generated charge carriers of opposite types will be separated by internal built in the electric field. Finally, those separate charge carriers are extracted to an external circuit.

Solar cell technology has some very attractive features [8]:

+ Solar resource, the total amount of solar energy available, is abundant.
+ No pollutants are emitted during operation.
+ Solar cells are quiet. There are no moving mechanical parts in a solar cell.
+ Solar cells are durable; 20-year warranty is standard today.
+ The technology is modular and scalable.

But solar electricity is also facing some important challenges:

− Relatively large areas are needed because solar energy is not highly concentrated. However, only ~10 $m^2$ *per capita* would be needed to satisfy the total world need for electricity.
− Electricity is produced only when the sun is shining. This implies a need for energy storage or combination with other sources to meet electricity demand all around the day. In *off-grid* applications, energy storage, such as batteries, is needed.
− The cost of solar electricity is high, in an order of 0.55€/kWh [9].
− PV generates direct current: special DC inverters are needed.

Solar cells can be made from single crystals, polycrystalline and amorphous semiconductors. PV cell technologies can be classified into first, second and third generation, depending on the basic material used and the level of commercial maturity. The first generation cells—also called conventional, traditional or wafer-based cells—are made of crystalline silicon. This is the commercially predominant PV technology, which includes materials such as single crystalline silicon and multi-crystalline silicon. Second generation PV systems are based on thin film solar cells, which include three main families: amorphous and micromorph silicon, CdTe and CIGS cells. Second generation solar cells are commercially significant in utility-scale photovoltaic power stations, building integrated photovoltaics or in small stand-alone power systems. The third generation of PV systems, often described as emerging

photovoltaics, includes novel technologies such as concentrating PV technology, dye-sensitized solar cells, organic solar cells, quantum dot solar cells, and inorganic solar cells that are still under demonstration or have not yet been widely commercialized. According to National Renewable Energy Laboratory classification, kesterites belong to emerging inorganic solar cells [10, 11].

## 1.2 Chalcopyrite and kesterite solar cells and absorber materials

Solar cells based on chalcogenide films, such as CdTe and CIGS, are at the forefront in thin film solar cell technology in terms of commercial production and laboratory record efficiency. CdTe solar cells are now the largest thin film technology in production with typical commercial module efficiencies of >17 % and record cell efficiencies of 21.5 % [12, 13], respectively. In the meantime, CIGS technology, as the main thin film competitor, has also reached module and cell efficiencies of >17 % and 21.7 % [12, 14]. However, reliance on the heavy metal Cd and non-abundant elements In and Te present a barrier toward meeting the multiterawatt-scale target for renewable energy supplied by photovoltaics [15].

Multinary kesterite structured semiconductor compounds $Cu_2ZnSnS_4$ (CZTS), $Cu_2ZnSnSe_4$ (CZTSe) and their solid solutions $Cu_2ZnSn(S_xSe_{1-x})_4$ (CZTSSe) with x = 0 – 1 are considered as promising alternative chalcogenide candidates for emerging photovoltaics with absorber materials made from non-toxic and earth abundant elements, except selenium. These semiconductors can be obtained by replacing half of the indium atoms in chalcopyrite $CuInSe_2$ or in $CuInS_2$ by zinc, and by replacing the other half of the indium atoms by tin. Kesterite structured p-type semiconductors with optimal direct band gap for solar energy conversion and high optical absorption coefficient in the order of $10^4$ $cm^{-1}$ are believed to be suitable alternatives for CIGS absorbers that contain rare and expensive indium [16, 17, 18]. The band gap energy of CZTS is around 1.5 eV [19], CZTSe has band gap energy around 1.0 eV [20] and the band gap of CZTSSe lies somewhere in-between, depending on the sulphur to selenium ratio in the material [21].

However, current kesterite CZTSSe solar cells have much lower efficiency than CIGS solar cells. The CZTSSe solar cells have achieved a record power conversion efficiency of 12.6 % [22]. Currently, the power conversion efficiency records of CZTS and CZTSe devices are 9.2 %, and 11.6 %, respectively [23, 24]. The CZTSSe MGL solar cells have shown power conversion efficiency up to 8.4 % [25]. While these are promising efficiencies for early-stage development, there is an urgent need to identify the main performance-limiting factors in an effort to improve the solar cell characteristics to a level more on par with CdTe and CIGS [26]. Kesterite solar cells show the highest efficiency when the absorber layers ($Cu_2ZnSnS_4$, $Cu_2ZnSnSe_4$ and their solid solutions) are non-stoichiometric with copper-poor and zinc-rich conditions, as reported in the

literature [22, 23, 24]. The fundamental cause of this composition range is not completely understood.

This performance gap between kesterites and chalcopyrites is caused by the narrow phase stability of the quaternary kesterite phase, $Cu_2ZnSn(S_xSe_{1-x})_4$, and the existence of other competitive and complex secondary phases and defect-complexes along with interfacial carrier recombination [6]. If successfully developed to reach efficiencies beyond 18%, the CZTSSe devices have the potential to replace the existing thin film solar cell technologies, such as CIGS and CdTe, which are faced with elemental abundance and toxicity [27].

## 1.3 Factors limiting kesterite structured solar cell working ability

A possible reason for main performance-limiting factors in kesterite structured thin film solar cells is that their absorber material often contains different additional binary and ternary phases. Due to the presence of four or even five elements in this compound semiconductor, there are many possibilities for the formation of secondary phases such as ZnS, ZnSe, CuS, $Cu_2S$, $Cu_{2-x}Se$, $SnS_{2-x}$, SnSe, $SnSe_2$, $Cu_2SnS_3$ and $Cu_2SnSe_3$, which constitute a serious problem for the preparation of kesterite absorber material [28, 29]. The investigations on the phase diagrams of the $Cu_2Se$-$ZnSe$-$Cu_2SnSe_3$ and $Cu_2S$-$ZnS$-$SnS_2$ systems by I.D. Olekseyuk $et\ al.$ [30, 31] show that the homogeneity range of the single phase CZTSe and CZTS are present only within a rather narrow range of compositions. According to the phase diagram, the single phase area of CZTSe is slightly wider to the Zn rich side than the CZTS single phase area. Even slight deviations from the optimal growth conditions of CZTS will result in the formation of secondary phases like ZnS, $Cu_2SnS_3$, SnS, $SnS_2$, and CuS, depending on whether the composition is more Cu, Zn or Sn rich. Theoretical calculations have shown that thermodynamically, the most stable defect in kesterites is Cu at Zn ($Cu_{Zn}$) antisite defect with fairly high concentration. The spontaneous formation of $Cu_{Zn}$ antisite defects up to the dilute limit is favoured due to the negative formation energy for the entire stability range of CZTS. The high concentration of intrinsic point defects places the Fermi energy at the valence band maximum, creating rather extended and shallow hole states. One way to optimize the carrier concentration in CZTS by controlling the $Cu_{Zn}$ antisite concentration is by introducing compensating donors or employing Cu-poor and Zn-rich growth conditions. Under these growth conditions, ZnS is the main competing phase. [32]. Zinc sulphide is also the most stable binary phase with high negative enthalpy of formation. At the same time, ZnS has a much larger band gap than CZTS and will lead to the formation of internal barriers, which are expected to degrade solar cell performance [29].

Additionally, CZTS and CZTSe absorber materials can exist as $ordered$ or $disordered$ kesterite crystal structures, which are related to the nature of intrinsic defects that causes structural disorder in the cation sub lattice of the

host lattice [33]. Zn and Cu elements are close neighbours in the periodic table with almost similar atomic size. So it is highly likely for Zn and Cu to occupy vacancies of counterparts and result in a disordered kesterite structure [34].

It is known experimentally that the band gap energy of CZTSe compound at room temperature is about 1.0 eV [20, 35], which is also confirmed by theoretical calculations [36]. Ideally, a single junction thin film solar cell absorber material should have direct band gap energy around 1.35 eV [37]. Therefore, it is required to adjust the band gap energy. One possible way to do so is to use solid solutions with an overall stoichiometry of $Cu_2ZnSn(Se_xS_{1-x})_4$ with $x = 0 - 1$.

High series resistance, the presence of blocking back contact and buffer/absorber interface recombination, is also reported as the main limiting factor in kesterite solar cells from the temperature dependent electrical analysis [26, 27, 38]. Several other key loss mechanisms have been identified, such as small minority carrier diffusion length, as estimated by bias-dependent external quantum efficiency measurements, and very low minority carrier lifetime, as revealed from the time-resolved photoluminescence measurements [39, 40]. Both of these parameters are related to high recombination current, which limits the open-circuit voltage and leads to weak long wavelength external quantum efficiency response that, in turn, limits the short-circuit current. A blocking behaviour at the absorber/back contact interface limits the fill factor [26].
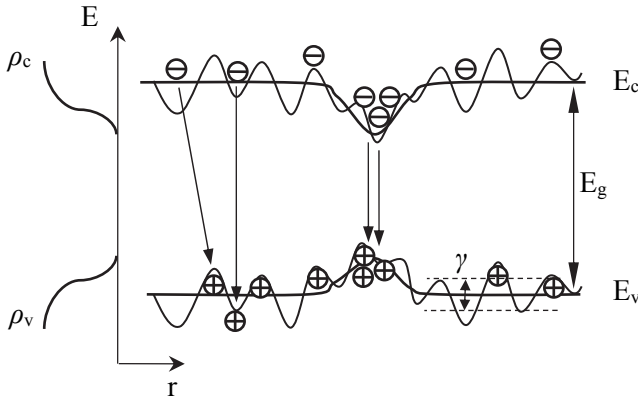


Figure 1: Schematic plot of the fluctuating band diagram of a heavily doped semiconductor. As a reason of heavy doping, the band edges start to fluctuate in space. Larger fluctuations may be related to a defect phase, defect region, or compositional fluctuations. The recombination paths are indicated with vertical arrows. On the left are presented, the density of state functions $\rho_c$, and $\rho_v$ of the conduction band, and the valence band, respectively.

Hence, almost all basic solar cell parameters are limited by recombination and parasitic losses. Moreover, most of kesterite absorber materials used in solar cells show properties of so-called heavily doped semiconductors, where high concentration of randomly distributed charged point defects leads to the formation of spatial electrostatic potential fluctuations. As a result, this will lead

to a local perturbation of the band structure, band tails are formed and the density of state functions of the valence ($\rho_v$) and conduction bands ($\rho_c$) are broadened (Fig. 1) [41]. The average depth of the potential fluctuations $\gamma$ is the mean difference of the energy of holes (electrons) in the valence (conduction) band fluctuation minimum and maximum (Fig. 1). The $\gamma$ value is dependent on the defect concentration. The larger potential fluctuations may be related to the presence of a defect phase or defect region that has a larger defect concentration. At the same time, high $\gamma$ values can be a result of compositional fluctuations where some crystal regions have different band gap energy than others (Fig. 1) [21].

Accordingly, different types of current transport have been observed. In principle, two temperature regions can be observed for heavily doped semiconductors. At high temperatures, the current flow is limited by the thermionic emission over the potential barriers and at low temperatures, when the energy of the majority charge carriers is less than the height of the potential barriers, the current flow is limited by the tunnel effect [42, 43]. The potential barriers could be formed due to the following: grain boundaries in polycrystalline materials or the spatial potential fluctuations, the high defect concentration, or the compositional fluctuations [44, 45, 46]. Many investigations of temperature-dependent conductivity of different kind polycrystalline semiconductors [47, 48, 49] including kesterites have been reported [50, 51, 52] where at high temperatures, the electrical conductivity is dominated by the thermionic emission and at lower temperatures, by the Mott variable-range hopping.

## 1.4 Recombination losses and defects in kesterite absorber materials

In kesterite solar cells, recombination losses are not only related to the interface between the absorber and buffer layers but also to different bulk defects or band tails. Many researchers have made the first-principles calculations for a series of intrinsic defects and defect complexes in CZTS [32, 53]. It has been shown that the intrinsic $p$-type conductivity in CZTS is attributed to the $Cu_{Zn}$ antisite defect, which has a low formation energy and relatively deep acceptor level at $E_A = 0.12$ eV compared to the Cu vacancy (0.02 eV). This deep acceptor $Cu_{Zn}$ antisite defect was also found by admittance spectroscopy [54]. Even a deeper acceptor ($E_A = 0.28$ eV) was detected in CZTS by photoluminescence spectroscopy [55]. These quite deep defects can be efficient recombination centres even at temperatures close to room temperature. In addition, Chen et al. [53] have found that the donor level is shallower in CZTSe than in CZTS, which could explain the higher efficiency obtained in CZTSSe cells with high Se content.

The calculations of band alignment between $Cu_2ZnSnS_4$ and the $n$-type counter partner CdS made by Chen et al. [53] reveal that a cliff-like (type II-staggered) band alignment exists for the $CdS/Cu_2ZnSnS_4$ heterojunction, i.e.,

the conduction band minimum is lower on the CdS buffer layer and the valence band maximum is higher on the CZTS absorber layer, which facilitates electron-hole separation. A typical energy band diagram of the TCO/CdS/CZTS heterostructure in Fig. 2 is modelled in [56]. The band alignment is defined simply as the discontinuity in the band edge at the interface between two semiconductors. A type II staggered alignment occurs when the band gaps of the two materials overlap but one does not completely enclose the other [57]. The results are expected to be relevant also to other $I_2$-II-IV-$VI_4$ semiconductors [53].
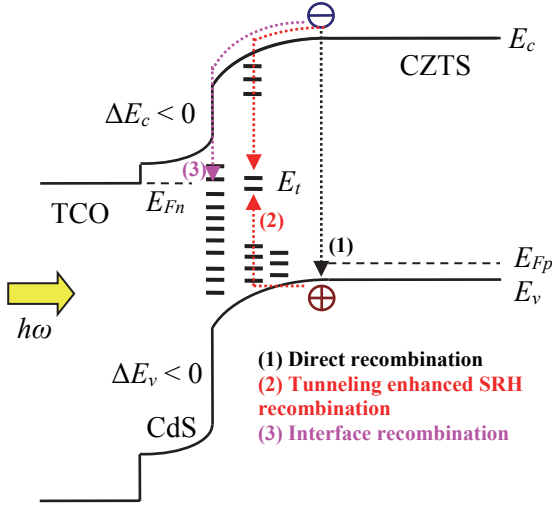


Figure 2: Energy band diagram of a typical CdS/CZTS heterostructure with the conduction band offset $\Delta E_c$ and the valence band offset $\Delta E_v$ between CdS and CZTS. The quantities $E_c$, $E_v$, $E_t$, and $EF_{p,n}$ denote the conduction band minimum, the valence band maximum, the trap level, and the quasi-Fermi energy of holes and electrons, respectively. The possible main recombination paths in the space-charge region are shown.

At the same time, using the first-principles theory, Chen et al. [58] showed that the compensation between the dominant acceptor defect $Cu_{Zn}$ and the donor defect $Sn_{Zn}$ can significantly decrease the formation energies of the defect clusters ($Cu_{Zn} + Sn_{Zn}$ and $2Cu_{Zn} + Sn_{Zn}$), leading to high concentrations of these clusters even in stoichiometric samples with Cu/(Zn + Sn) and Zn/Sn ratios near 1. The partially passivated $Cu_{Zn} + Sn_{Zn}$ cluster produces a deep donor level in the band gap of CZTS, and the fully passivated $2Cu_{Zn} + Sn_{Zn}$ cluster causes a significant local band gap decrease. Both effects are detrimental to photovoltaic performance, so Zn-rich and Cu, Sn-poor conditions are required to prevent their formation and increase the efficiency. Temperature dependent photoluminescence (PL) study of $Cu_2ZnSnS_4$ polycrystals showed that the recombination through these defect clusters dominates in most CZTS samples at low temperatures [45]. The presence of different defect complexes in CZTS was also proposed by Huang et al. [59]. According to their calculations, these

complexes can cause a significant local band gap decrease and boost the recombination.


## 1.5 Electrical conductivity in kesterite materials

The temperature dependent conductivity of polycrystalline kesterite thin films [26, 38, 50–52] and single crystals [60] has been studied in many papers. The referenced samples were prepared by various physical and chemical thin film deposition technologies, including vacuum [38, 43, 50, 52, 60] and nonvacuum [26, 51] processes. To investigate the temperature dependence of resistivity, $\rho(T)$, series resistance values obtained from the solar cells current-voltage curves were used [26, 38], the standard two probe DC current-voltage measurement of Ohmic contacts through-thickness [50] and on planar configuration [51] were applied, and the van der Pauw method in darkness was frequently employed [43, 52, 60].

The studied samples were prepared by different technologies and electrical conductivity investigated by different methods; however, kesterites seem to have one common conductivity mechanisms profile over temperatures ranging from 10 – 300 K and beyond. Different conduction mechanisms dominate over different temperature ranges in polycrystalline kesterite photovoltaic absorber materials [50]. Typically, the conductivity $\sigma(T)$ data have been divided into two different regions: high and low temperatures.

At high temperatures ($T > 180$ K), the electrical conductivity of the polycrystalline kesterite thin films is dominated by thermionic emission across potential barriers due to grain boundaries. As temperature decreases, for a *p*-type semiconductor, most of the free holes are recaptured by the acceptors. Then the holes do not have sufficient thermal energy to be excited from the acceptor levels to the valence band. In this case, the band conduction becomes less important, and the hole hopping directly between the acceptor states in the impurity band will be the main contributor to the conduction mechanism. If the compensation ratio is very high, the Fermi level will be located in the impurity band. Conduction of a compensated sample in this case is realized through nearest-neighbour hopping (NNH) of charge carriers with small activation energy directly over impurity states [43].

At lower temperatures, charge carrier hopping between nearest neighbour sites is not always favoured due to the significant energy difference of the levels. Then holes prefer to jump to a more energetically similar but remote site. Therefore, in disordered or highly compensated materials, the mechanism of electrical conduction changes from NNH to Mott variable-range hopping (M-VRH) at a critical temperature. As the temperature decreases further, the Coulomb effect becomes important and the conductivity crosses over from the M-VRH to the Efros–Shklovskii variable-range hopping (ES-VRH) regime [43].

Many different analysis of electrical transport showed a large degree of disorder due to high doping levels and large compensation ratio that creates potential fluctuations in the bulk of the kesterite grains [43].

## 1.6 Kesterite structured monograin materials

To avoid additional phases, it seems to be more appropriate to use higher temperatures for material growth to improve the control of the phase composition of the product. For this reason, so-called monograin solar cells [35, 61, 62] look very promising. At the same time, many physical properties of these kesterite monograins are still unclear and also solar cells made on their basis need to be studied in more detail. For further use of these materials as absorber materials for PV applications, it is essential to find out the temperature dependence of solar cell parameters since solar cell performance generally decreases with increasing temperature. Fundamentally, the solar cell performance decreases with increasing temperature due to increased internal carrier recombination rates caused by increased carrier excitation.

Correlations expressing the temperature dependence of the PV module's electrical efficiency are numerous, although many of them assume the familiar linear form, differing only in the numerical values of the relevant parameters which are material and system dependent [63, 64]. Knowing these parameters is crucial for predicting the temperature dependence of kesterite-type modules also in the future.

## 1.7 Aim of the study

Derived from the literature review above, the objectives of the present doctoral thesis were to study the temperature and spectrally dependent electrical properties of different kesterite type absorber material MGL solar cells to identify loss mechanisms and reveal current transport properties. To characterize recombination and parasitic effects, current-voltage (J-V) characteristics and external quantum efficiency (EQE) curves were used. In order to investigate the spatial electrostatic potential fluctuations in the kesterite-based MGL solar cells, the aim of the study was to propose a new simple method by using temperature and spectrally dependent photo-current response measurement analysis.

# 2. THEORY OF SOLAR CELL ELECTRICAL CHARACTERIZATION

## 2.1 Electrical characterization methods

In the research of possible improvements to solar cell designs and the underlying physical processes limiting their performance, it is important to characterize the electrical performance of the devices. In the wide range of characterization methods available for thin film solar cells, the simplest and the most common tool for solar cell evaluation and characterization is the measurement of current-voltage (I-V), or more often current density versus voltage (J-V) curves under standard illumination conditions, 100 mW/cm$^2$ AM1.5 spectrum at 25 °C. Frequently, J-V characterization means determination of the basic parameters: open-circuit voltage ($V_{OC}$), short-circuit current density ($J_{SC}$), fill factor ($FF$), and efficiency ($\eta$). However, besides the basic characteristics of conversion efficiency, there is a wealth of additional information that can be obtained by analyzing the entire J-V curve. This is particularly so if the dependences on light intensity and temperature are considered. One extension of a regular J-V measurement is the measurement of the wavelength-dependent current response, typically performed at zero bias. This is referred to as the "quantum efficiency" as after proper normalization, it represents the fraction of photons of wavelength $\lambda$ that are converted into electron-hole pairs and collected as current [65, 66].

Solar cell operation can be characterized by identifying loss mechanisms. These loss mechanisms can be divided into three basic categories. First, recombination losses limit the $V_{OC}$. Second, parasitic losses, such as series resistance, shunt resistance, and voltage-dependent current collection that primarily impact the $FF$, but can also reduce $J_{SC}$ and $V_{OC}$. Finally, optical losses limit the generation of carriers and, therefore, $J_{SC}$ [66].

## 2.2 Current-voltage analysis

### 2.2.1. Solar cell basic parameters

An example of a typical solar cell light and dark J-V curves is shown in Fig. 3 and from three points on the light J-V curve, basic parameters of the solar cell can be deduced: open-circuit voltage $V_{OC}$, short-circuit current $J_{SC}$ and fill-factor $FF$. The fill-factor is defined as $FF = (V_{MPP} J_{MPP})/(V_{OC} J_{SC})$, $V_{MPP}$ and $J_{MPP}$, being the voltage and current density at the point of maximum power, and it represents the ratio between the two squares marked in the fourth quadrant of Fig. 3. From these, the efficiency $\eta$ of a cell is defined as

$$\eta = \frac{P_{MPP}}{P_{AM1.5}} = \frac{V_{MPP}J_{MPP}}{P_{AM1.5}} = \frac{V_{OC}J_{SC}FF}{100mW/cm^2} \qquad (1)$$
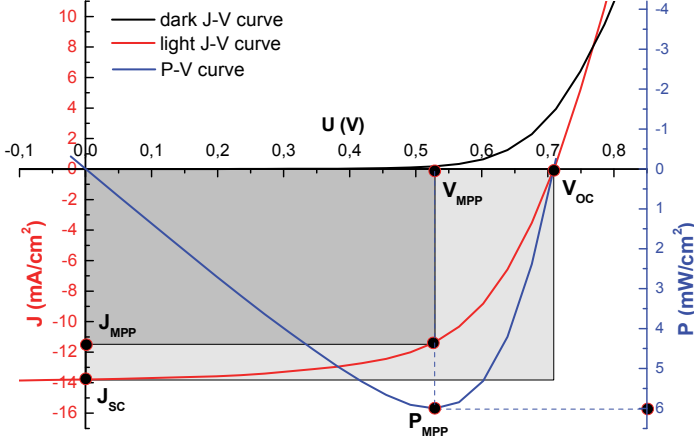


Figure 3: Light and dark J-V curves and output power curve of a CZTS solar cell [III] at room temperature. The basic parameters: short-circuit current density $J_{SC}$, open-circuit voltage $V_{OC}$ and the maximum power point $P_{MPP}$ with the associated current density $J_{MPP}$ and voltage $V_{MPP}$ are marked.

Here $P_{AM1.5}$ is the incident light power at AM1.5 illumination and $P_{MPP}$ is the maximum output power of the solar cell.

### 2.2.2. Idealized analytical solar cell model

The basic solar cell parameters, however, are not the only information we can obtain from J-V data. Interpretation of J-V measurements can give much information about the diode parameters. From the dark and light J-V curve analysis, the quality of the *p-n* junction and losses related to resistive components of the device can be concluded. Quantitative analyses can be derived from diode equations based on a one or two diode model [67]. These models are based on the exponential Shockley equation for a diode. The simplest form of the Shockley ideal diode equation reads

$$J_D(V) = J_0\left[\exp\left(\frac{qV}{nkT}\right) - 1\right], \qquad (2)$$

where $J_D$ [mA/cm$^2$] is the diode current density, $J_0$ [mA/cm$^2$] is the saturation current density of the diode, $V$ [V] is the voltage applied across the diode, $k$ [J/K] the Boltzmann constant, $T$ [K] the absolute temperature of the *p-n* junction, $q$ [C] is the elementary charge and, $n$ is the dimensionless diode

ideality factor, also known as quality factor. For an ideal diode, $n$ is constant and $J_0$ is only dependent on temperature.
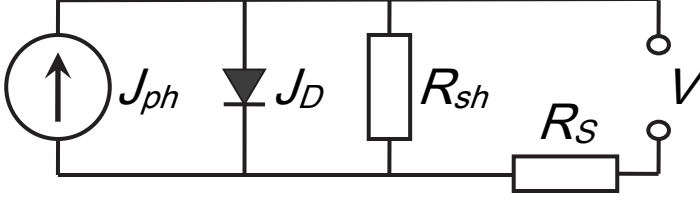


Figure 4: Equivalent circuit diagram of a solar cell using a one diode model, including a diode (the *p-n* junction) with an associated current density $J_D$, a current source accounting for the photo-generated current density $J_{ph}$, as well as series resistance $R_S$ and shunt resistance $R_{sh}$.

Ideally, a solar cell J-V curve can be described by a single Shockley ideal diode equation (2) shifted by the photo-generated current density $J_{ph}$. Kesterite solar cells are not really ideal. Extending the ideal diode equation (2) for the case of constant $J_{ph}$ based on the equivalent circuit diagram for a solar cell shown in Fig. 4, it is necessary to take into account also series resistance $R_S$ and shunt resistance $R_{sh}$ of solar cells. Then the idealized solar cell equation will be given by

$$J = J_0 \left[ \exp\left( \frac{q(V - R_S J)}{nkT} \right) - 1 \right] + \frac{(V - R_S J)}{R_{sh}} - J_{ph}, \qquad (3)$$

where the photo-generated current density $J_{ph}$, the dark saturation current density $J_0$, and the diode ideality factor $n$, generally can all be dependent on both bias voltage $V$ and temperature $T$. Series resistance $R_S$, shunt resistance $R_{sh}$, and diode ideality factor $n$ describe non-idealities that limit the performance of the solar cells. The ideality factor is a measure of the junction quality and the type of recombination in a solar cell. For the thermionic emission, the $n$ has a value of 1. However, some recombination mechanisms, particularly if they are large, may introduce an ideality factor of 2. A high value of $n$ not only degrades the *FF*, but since it usually indicates high recombination, it gives low $V_{OC}$ as well.

### 2.2.3. J-V curve parameter extraction

There are several ways to extract the parameters of J-V characteristics such as $R_S$, $R_{sh}$, $J_0$, $n$, and $J_{ph}$. One way to extract the parameters is to fit the whole solar cell equation (3) to the measurement data in one least squares fit procedure or by several consecutive linear fits to different representations of different parts of the J-V curve [68]. The J-V curve analysis used in this thesis follows the procedure outlined by Hegedus and Shafarman [66].

The plots in Fig. 5(a)–(d) illustrate the analysis procedure.

(a) A standard linear J-V curve where the main solar cell parameters $V_{OC}$, $J_{SC}$, $FF$, and $\eta$ are derived The next three plots are derived from these light or dark J-V curves.

(b) A plot of the derivative $g(V) \equiv dJ/dV$ against $V$ near $J_{SC}$ and in reverse bias. If the term is ohmic and $J_{ph}$ is constant, $g(V)$ will be flat with the value in reverse bias equal to $G = 1/R_{sh}$.

(c) A plot of the derivative $r(J) \equiv dV/dJ = R_S + \frac{nkT}{q}\left(J + J_{ph}\right)^{-1}$ against $(J+J_{SC})^{-1}$ will yield a straight line if $J_{ph}$ is independent of voltage. $R_S$ is given by the intercept with $y$ axis and $n$ can be calculated from the slope $nkT/q$. A correction can be made for the case in which $R_{sh}$ is not negligible by plotting $(J+J_{SC} - V/R_{sh})^{-1}$ on the abscissa. For the analysis of the dark J-V curve, $J_{SC}=J_{ph}=0$.

(d) A semilogaritmic plot of $J+J_{SC}$ against $V-R_S J$ using the value of $R_S$ is obtained from plot (c). A linear region over at least 1–2 orders of magnitude in current indicates a good fit to the diode equation. The intercept then gives $J_0$ and the slope in this case equals $q/nkT$; so, $n$ can be calculated and compared with the value from plot (c). Again, a correction for $R_{sh}$ can be made, in this case by plotting $J+J_{SC} - V/R_{sh}$ on the ordinate.
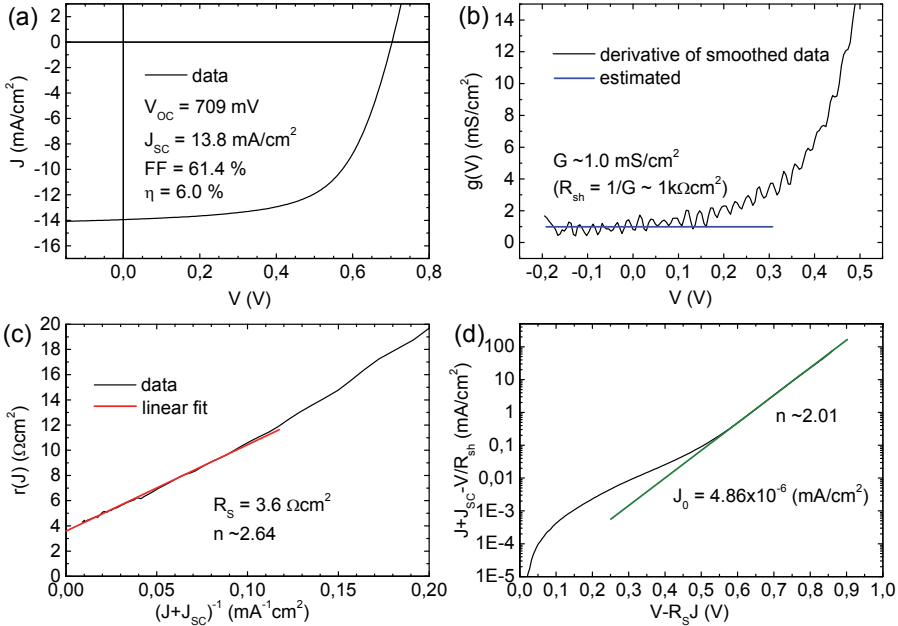


Figure 5: Four step analysis of J-V curves. The details of these four steps (a)–(d) are given in the text. The data presented are an example of a four step analysis procedure applied to one of the light J-V curves of CZTS absorber material MGL solar cells studied in the paper (III).

### 2.2.4. *Parasitic effects*

In most cases, deviations from the behaviour predicted by Eq. (3) can be attributed to parasitic effects such as non-ohmic or blocking contributions in series with the primary diode or shunt-like effects in parallel with the primary diode. The parasitic effects pointed out below are described in more detail by Hegedus and Shafarman [66].

Resistive effects in solar cells reduce the efficiency by dissipating power in the resistances. The most common parasitic resistances are series resistance $R_S$ and shunt resistance $R_{sh}$. In most cases, the key impact of parasitic resistance is the reduction of *FF*, although excessively high parasitic resistance may also reduce $J_{SC}$ and $V_{OC}$, respectively.

A common cause for the light J-V curve deviation from the diode behaviour is a voltage-dependent photocurrent collection, $J_{ph}(V)$. In general, there are several possible explanations as any of the parameters in the diode equation could be illumination dependent. $J_{ph}(V)$ could be caused by field-dependent collection in the absorber layer or there could be a voltage-dependent barrier height to the current collection. These can be separated by the wavelength and voltage-dependent QE. Similarly, the difference in *FF* under blue and red light can be used to distinguish $J_{ph}(V)$ losses. Generally, the shunt term, which describes a parallel path to the main diode current, is assumed to be ohmic, i.e., $G$ is assumed to be independent of $V$. A voltage-dependent shunt, $G(V)$, would affect light J-V measurements identically to $J_{ph}(V)$, but $G(V)$ could be distinguished from $J_{ph}(V)$ as it would be expected to have the same effect on the dark data. Experience with many thin film solar cells has shown that voltage-dependent photocurrent collection $J_{ph}(V)$ is the most likely explanation when the dark J-V curve is well behaved, but the light J-V curve deviates.

Other common parasitic effects that are observed in thin film solar cells include blocking behaviour, which can originate at a second junction in the device, such as non-ohmic contact, or from an interface barrier that may block carrier collection in the forward bias. The latter situation could arise, for example, due to a spike in the conduction band alignment at the *p-n* junction interface.

Another cause for non-ideal J-V curve behaviour is the light-to-dark crossover, which can be caused by photoconductive effects or a light-dependent barrier. Other more fundamental reasons for the inability to describe the data with Eq. (3) include the contributions of more than one recombination mechanism or a voltage-dependent diode quality factor $n(V)$.

### 2.2.5. *$J_{SC}$-$V_{OC}$ method*

In case the dark and illuminated J-V characteristics exhibit rather different voltage dependences, it is indicative that the superposition principle is not fulfilled for solar cells. Therefore, it cannot be expected that the recombination

process determined for solar cells in the dark stringently describes behaviour under illumination. On the other hand, neither is a straightforward evaluation of the J-V curve under illumination possible, as the voltage-dependent photocurrent $J_{ph}(V)$ leads to an incorrect determination of the diode parameters. Furthermore, neither is it straightforward to extract the diode parameters from a measurement that is influenced by $R_S$ and $R_{sh}$ [69, 70].

Therefore, we can use another method to determine the solar cell diode parameters by measuring $J_{SC}$ and $V_{OC}$ for different light intensities, with identical spectral content at a given temperature. Inserting, respectively, $V = 0$ and $J = 0$ in Eq. (3) gives

$$-J_{SC} = J_0 \left[ \exp\left( -\frac{qR_S J_{SC}}{nkT} \right) - 1 \right] - \frac{R_S J_{SC}}{R_{sh}} - J_{ph} \tag{4}$$

$$J_{ph} = J_0 \left[ \exp\left( \frac{qV_{OC}}{nkT} \right) - 1 \right] + \frac{V_{OC}}{R_{sh}} \tag{5}$$

If $R_S$ is small compared to $V_{OC} / J_{SC}$ (less than 1%) and $R_S / R_{sh} \ll 1$, then in Eq. (4), $J_{SC} = J_{ph}$ and in Eq. (5), $J_{SC}$ and $V_{OC}$ satisfy the diode law without the influence of series resistance. The influence of the shunt resistance remains, but at high-enough light intensities, $V_{OC}$ remains unaffected. Using Eq. (5), we are able to extract $J_0$ and $n$. A semilogarithmic plot of (Ln $J_{SC}$) vs. $V_{OC}$ will yield a straight line for high-enough $V_{OC}$. At a given temperature, $n$ can be calculated from the slope and $J_0$ can be found by taking the intercept of the plot with the $J_{SC}$-axis. A small error in the estimation for $n$ results in a large error in $J_0$ due to the use of the logarithmic scale. Therefore, the value of $J_0$ will generally be less accurate than that of $n$ [69].

It is worth reminding that $J_{SC}$ vs. $V_{OC}$ method works only for a well-behaved case of $J_{ph}$. In the case of voltage-dependent $J_{ph}(V)$ or $G(V)$, this method could also give erroneous results, overestimating $n$. One advantage of this method is that $R_S$ correction can normally be ignored since it makes no contribution at $V_{OC}$, or at $J_{SC}$, except at an extremely large $R_S$ [66].

### 2.2.6. Temperature dependences of J-V parameters

Like all other semiconductor devices, solar cells are sensitive to temperature. Increase in temperature reduces the band gap of a semiconductor, thereby affecting most of the semiconductor material parameters. The main temperature dependence in solar cells arises from the variation of three main parameters: $J_{SC}$, $V_{OC}$, and $FF$, which are commonly used to characterize the solar cell outputs [71]. In a solar cell, the parameter most affected by change in the temperature is $V_{OC}$.

A specific objective in the characterization of the J-V behaviour of a solar cell is to determine a mechanism that limits $V_{OC}$. It is helpful to look at $V_{OC}$ as a

function of $T$ to determine the dominant recombination path. Any of several different recombination paths could dominate the device behaviour at $V_{OC}$, including recombination currents in the space-charge or quasi neutral regions of the absorber layer or at any of the critical interfaces, including the absorber/buffer interface or the absorber/back contact interface. In addition to the recombination paths, the tunnelling contribution can be estimated using the temperature dependent J-V characterization method [66]. The different dominant recombination paths in thin film solar cells are illustrated in Fig. 6 [8]. These are in the direction of the incoming light:

- **TE-IFR** Tunnelling-enhanced recombination at the buffer/absorber interface
- **TE-SCR** Tunnelling-enhanced recombination in the space charge region
- **QNR** Recombination in the quasi-neutral region
- **BCR** Recombination at the back contact
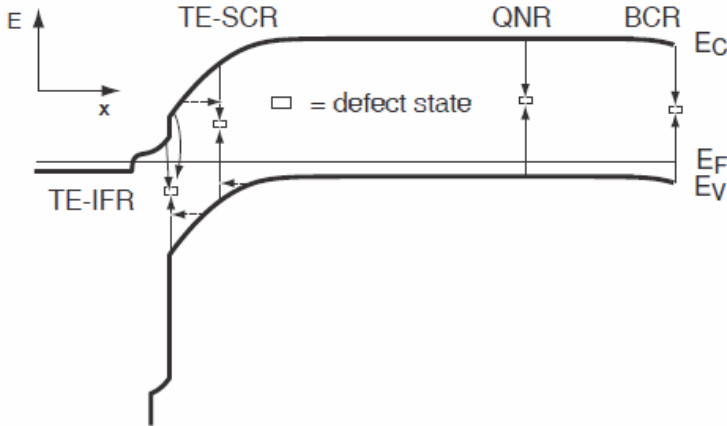


Figure 6: Schematic illustration of the dominant recombination paths in thin film solar cells. The vertical arrows indicate how electrons from the bottom of the conduction band ($E_C$) can recombine with holes from the top of the valence band ($E_V$) via defect states within the band gap. The horizontal arrows indicate how recombination can be enhanced by tunnelling in regions with high electric field. In the direction of the incoming light, the recombination paths are: tunnelling-enhanced recombination at the buffer/absorber interface (TE-IFR), tunnelling-enhanced recombination in the space charge region (TE-SCR), recombination in the quasi-neutral region (QNR), and recombination at the back contact (BCR). *Reproduced from J. Malmström dissertation [8].*

Normally, tunnelling enhancement is important only for interface recombination and for recombination in the space charge region, as indicated by the horizontal arrows in Fig. 6. However, tunnelling can be important also for recombination at the back contact if there is a strong band bending close to this interface. In addition, tunnelling can contribute to recombination at grain boundaries or at band tails due to potential fluctuations, even in the formally

quasi-neutral region. Recombination in the buffer and window layers is not included in the list. Under dark conditions, these recombination paths can clearly be neglected because of the wider band gap $E_g$ of these layers [8].

The open-circuit voltage, $V_{OC}$, is the maximum voltage available from a solar cell, and this occurs at zero current. The open-circuit voltage is the voltage at which the forward bias diffusion current is balanced by the photo-generated current. The forward bias diffusion current is dependent on the amount of recombination in a *p-n* junction and increasing the recombination increases the forward bias current. Consequently, high recombination increases the forward bias diffusion current, which, in turn, reduces the open-circuit voltage. $V_{OC}$ can be obtained from Eq. (3) by setting the net current $J = 0$. Therefore,

$$V_{OC} = \frac{nkT}{q} \ln\left[1 - \frac{V_{OC}}{R_{sh}J_0} + \frac{J_{ph}}{J_0}\right] \tag{6}$$

The above equation shows that $V_{OC}$ depends mainly on $J_0$ of the solar cell and on the photo-generated current. While $J_{SC}$ typically has a small variation depending on the temperature, the key effect on the performance of the solar cell is $J_0$, since it may vary by orders of magnitude. The recombination is controlled by the concentration of minority carriers at the junction edge, i.e., how fast they diffuse into the quasi-neutral region of the junction and how quickly they recombine. Therefore, $V_{OC}$ is a measure of the amount of recombination in the device. According to theory, $J_0$ is a function of material properties and it is also sensitive to temperature. In general [71, 72],

$$J_0 = J_{00} \exp\left[-\frac{E_A}{nkT}\right] \approx AT^2 \exp\left[-\frac{E_A}{nkT}\right], \tag{7}$$

where the activation energy $E_A$ and the saturation current density prefactor $J_{00}$ depend mainly on the dominating recombination mechanism (tunnelling or thermal activation) in the solar cell. $J_{00}$ is also proportional to the density of recombination centres in both cases [73]. The parameter $A$ includes the Richardson constant.

According to Eq. (6), if $n$, $J_{00}$ and $J_{ph}$ are only weakly dependent on or independent of temperature, we expect a linear dependence of $V_{OC}$ on temperature if $J_{ph} \gg V_{OC} / R_{sh}$ and $J_{ph} \gg J_0$, then from Eqs. (6) and (7), we have

$$V_{OC} = \frac{E_A}{q} - \frac{nkT}{q} \ln\left[\frac{J_{00}}{J_{ph}}\right] \tag{8}$$

From the extrapolation of $V_{OC}$ to $T = 0$ K, the activation energy $E_A$ can be determined. This method of extracting the activation energy is useful only when the ideality factor is independent of temperature, which is rarely the case with CZTS-based cells [66, 70, 74].

However, as soon as tunnelling becomes important, the ideality factor becomes temperature dependent, inducing nonlinear terms into Eq. (8). Hence, a

more refined evaluation scheme is required. Temperature dependence of $n$ and $J_0$ gives indications on what the main recombination paths are [69]. From Eq. (7) for the $J_0$, the following expression can be derived:

$$\ln\left(\frac{J_0}{J_{00}}\right) = \frac{-E_A}{nkT}$$

(9)

Assuming that the activation energy has linear temperature dependence; this assumption is reasonable since the temperature dependence of the band gap energy is close to linear [75] in the temperature region where temperature dependent J-V measurements are typically performed. By reorganizing Eq. (9), we obtain

$$n\ln(J_0) = n\ln(J_{00}) - \frac{E_A}{kT}$$

(10)

A plot of $n\ln(J_0)$ versus $1/kT$ should yield a straight line with a slope corresponding to the activation energy $E_A$. For the two models considered above [Eqs. (8) and (10)], in case $E_A$ is equal or close to the value of $E_g$ of the absorber material, $V_{OC}$ is determined by recombination in the SCR or in the QNR. In case $E_A < E_g$, the interface recombination is dominating. In practice, the recombination often may not fit the textbook cases due to, for example, recombination through defect bands rather than discrete states or by tunnelling or multistep processes. A quantitative analysis of the temperature dependence of the ideality factor is required to decide in either case whether or not tunnelling contributes significantly to recombination [66, 68, 74].

Ideality factor of a well-behaved device is typically in the range $1.3 \le n \le 2$. The results for $E_A \approx E_g$ and $n$ indicate that the solar cell operates with the diode current controlled by recombination through trap states in the space-charge region of the absorber layer. The variation in $n$ between 1 and 2 depends on the energies of the deep defects that act as dominant trap states and relatively small temperature dependence of $n$ has been attributed to a distribution of trap states or a tunnelling contribution to the space-charge recombination current [66].

## 2.3 Hopping conductivity

Hopping conduction is defined as electric conduction in which the carrier transport via electrons is hopping from one localized state to another. Electron transport through localized states (shallow-level states or deep-level states) within the band gap of a semiconductor includes (as shown in Fig. 7) [76]:
1. Electron hops from one state to another state that has a higher energy. A thermal energy is required for that move. Let us denote the energy difference as $E_{hop}$. This process is thermally assisted tunnelling. It depends on temperature.

2. Electron hops from one state to another state that has equal energy. This is a tunnelling process. It does not depend on temperature.
3. Electron hops from one state to another state that has a lower energy. This transport is a tunnelling process with the emission of a phonon(s). It does not depend on temperature.
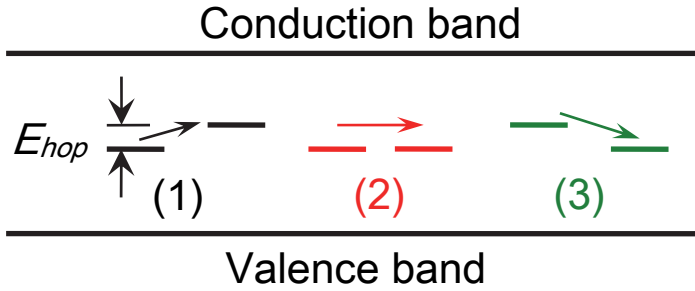


Figure 7: Electron transport between localized states: (1) thermally-assisted tunnelling; (2) tunnelling; and (3) tunnelling with the emission of a phonon(s).

The conditions necessary for the occurrence of hopping are:
1. Wave functions of two localized states must overlap.
2. Both occupied and unoccupied states must be present for the hopping to occur. This condition requires that the hopping should happen between states close to the Fermi level.
3. Additional energy is necessary for the electron hopping from one localized state to another localized state with a higher energy level.

The hopping conductivity is given by a universal expression:

$$\rho(T) = \rho_0(T)\exp\left[(T_0/T)^p\right], \tag{11}$$

where the prefactor $\rho_0(T) = AT^m$, $A$ is the prefactor constant and $T_0$ is the characteristic temperature. Exponents $m$ and $p$ are interrelated and depend on the mechanism of the hopping charge transfer. The NNH conductivity is given by $m = p = 1$. The VRH conductivity is described by the values of $p = \frac{1}{4}$ (the Mott type) and $p = \frac{1}{2}$ (the Efros–Slovskii type). The M-VRH conductivity takes place when the Coulomb interactions between the carriers are unimportant. Otherwise, such correlations lead to a soft Coulomb gap, $\Delta$, in the density of the localized states around $\mu$ and to the ES-VRH conductivity [77].

## 2.4 Quantum Efficiency analysis

Quantum Efficiency (QE) measurement is a valuable tool to characterize solar cells photocurrent collection. This analysis method is commonly used to determine the losses responsible for reducing the measured $J_{SC}$ from the maximum achievable photocurrent. Typical measurement equipment is very simple and consists of a calibrated light source, wide enough to simulate the solar spectrum, optics, monochromator and electronics to measure the generated photocurrent. QE is a dimensionless parameter given by the number of charge carriers generating external photocurrent per incident photon at each wavelength [66].

There are two types of quantum efficiency of a solar cell often considered:

- External Quantum Efficiency (EQE) includes the effect of optical losses such as transmission and reflection.
- Internal Quantum Efficiency (IQE) is defined as a probability that only photons neither reflected nor transmitted out of the cell contribute to the photocurrent, as a function of the photon wavelength.

In this thesis, EQE has been studied. The product of the measured EQE with the whole solar electromagnetic spectrum, typically AM1.5G for terrestrial solar cells, integrated over wavelength will give the amount of photocurrent that the cell will produce when exposed to sunlight. Thus, a good verification of the QE measurement is that the current calculated by integrating the EQE measured with 0 V bias, with the AM1.5G spectrum agrees with $J_{SC}$. Although significant differences between the integrated QE and the measured $J_{SC}$ may occur when the collection of the charge carriers depends on the intensity and/or spectrum of the incident illumination [66].

Ideally, the QE has a square shape, where the QE value is fairly constant across the entire spectrum of wavelengths measured. However, the QE for the real solar cells is reduced due to the optical and electronic losses. Optical losses are related to:

- Shading from the collection grid;
- Reflection from the front-surface and from the interfaces of materials used to build the device;
- Absorption in the window and the buffer layers;
- Incomplete absorption in the absorber layer near the band gap;
- Transmission through the non-active area (peculiarity of MGL solar cells).

Electronic losses are related to incomplete collection of photogenerated carriers in the absorber. Thus, electronic losses can be separated from the optical losses by the QE measurements at different voltage bias since only electronic losses should be affected by the applied bias [66].

The quantum efficiency of a solar cell can be calculated from the equations for minority carrier continuity and current density [78]. The QE resulting from depletion-region photon absorption should be

$$QE_{dr} \cong 1 - \exp(-\alpha W) \qquad\qquad (12)$$

and that from bulk absorption followed by carrier diffusion should be

$$QE_{bulk} \cong \frac{\alpha L_{eff} \exp(-\alpha W)}{\alpha L_{eff} + 1}, \qquad\qquad (13)$$

where $\alpha$ is the absorption coefficient for wavelength $\lambda$, $W$ is the depletion width, and $L_{eff}$ is the effective diffusion length for electrons in the absorber after correction for the finite thickness of the absorber. These equations combine for a total quantum efficiency

$$QE \cong 1 - \frac{\exp(-\alpha W)}{\alpha L_{eff} + 1}. \qquad\qquad (14)$$

# 3. EXPERIMENTAL

## 3.1 Synthesis of Kesterite monograin powders

All the kesterite monograin powder absorber materials for studied samples in this thesis were synthesized from $Cu_2S$ or CuSe, SnS or SnSe and ZnS or ZnSe powder binary and elemental sulphur and/or selenium precursors in molten potassium iodide (KI) by the isothermal recrystallization process by Dr. Kristi Timmo and Dr. Jaan Raudoja at Tallinn University of Technology. The quartz ampoules with mixtures of grounded precursors in intended quantities were degassed under dynamic vacuum, sealed and isothermally annealed at 740 °C for 90 hours. After the synthesis, ampoules were quenched to room temperature, opened and the flux material was removed by leaching with deionised water. The released monograin powder was dried and sieved to narrow granulometrical fractions. During the cooling of the batch of the material, part of the dissolved chalcogenides and/or dissolved kesterite precipitates on the surfaces of the monograins, therefore, additional chemical and thermal post treatments are needed to remove them. The details of the monograin growth technology can be found elsewhere [79].

## 3.2 Preparation of monograin layer solar cell

Post-treated powder crystals were covered with chemical bath deposited CdS buffer layers. For MGL formation, a monolayer of kesterite type powder crystals were embedded into a thin layer of epoxy such that the upper part of each grain sticks out of the polymer film. After polymerization of this epoxy, i-ZnO and conductive ZnO:Al were deposited by radio frequency (RF) sputtering onto the open (i.e., not covered by epoxy) surface of the layer. Solar cell structures were completed by vacuum evaporation of 1–2 μm thick In grid contacts onto the ZnO window layer. Finally, the glass substrate was glued onto the front surface of the MGL membrane and the back contact area of crystals was opened by chemical etching and by additional abrasive treatment methods. Graphite paste was used to apply the back contacts. The analysis area of the solar cell is determined by the back contact area, which is typically about 0.04 $cm^2$. The active area of the MGL solar cells is around 75% of the total analysis area. The other 25% of the total area, comprising epoxy between the absorber crystals, is passive. More details about the solar cell preparation can be found in [80].
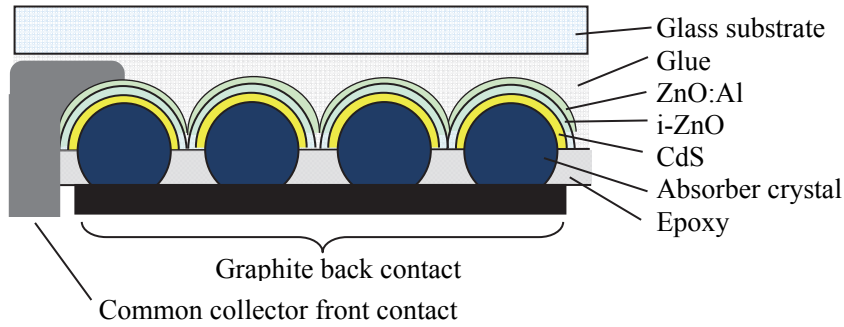
Figure 8: Monograin layer solar cell structure.

In principle, all of the MGL solar cells studied in this thesis research are of superstrate structure: graphite/MGL/CdS/ZnO/glass, as shown in Fig. 8, were made from post-treated monograin powder crystals with a diameter of 56–63 μm, as selected by sieving. The CZTSe, CZTS and CZTSSe solid solution absorber materials were Cu-poor and Zn-rich [35, 61, 62].

## 3.3 Current-Voltage and External Quantum Efficiency measurements

All the experiments were conducted at the Department of Materials Science, Tallinn University of Technology.

For the temperature dependent J–V and EQE measurements, the solar cells were mounted in a closed-cycle He-cryostat (*Janis*) where the temperature of the cell can be controlled in the range of T = 10–300 K. J–V measurements were done by decreasing the temperature while EQE measurements were done by increasing the temperature.

For the temperature dependent J–V measurements, an *Autolab PGSTAT30* potentiostat/galvanostat instrument was used as a source meter. The same instrument was also used as a potentiostat and a current amplifier for the EQE measurements to detect the generated photocurrent at 0 V and -1 V bias voltages.

Standard halogen lamp with calibrated intensity was used as a light source for both J–V($\Phi$,T) and EQE(V,T) measurements. The maximum intensity of the J–V($\Phi$,T) measurements was 300 mW/cm$^2$. Lower intensities were realized by using spectrally neutral net filters.

For EQE measurements, the same calibrated halogen lamp was used as a light source together with computer controlled prism monochromator *Carl Zeiss SPM-2* (*f* = 40 cm). Monochromatic and modulated (120 Hz) light was focused on the front surface of the solar cell. The generated short-circuit current signal was converted to potential with an *Autolab* instrument and detected with a *Stanford Research Systems* lock-in amplifier (*SR810DSP*). The software that

controls the EQE system was written on the *LabView* platform by my co-worker Erkki Kask. The software scans the spectrum that exits the monochromator slit from the desired range, at the same time recording the signal from the lock-in amplifier. Also, the software controls the temperature controller.

The output parameters $J_{SC}$, $V_{OC}$, *FF* and $\eta$ of MGL solar cells were deduced from J–V characteristics measured routinely using a *Keithley 2400* source meter with the *Oriel* class A solar simulator (*19159A, Newport*).

The measured J–V curves and EQE spectra were analysed with the MS Excel or Origin software.

# 4. RESULTS AND DISCUSSION

## 4.1 Temperature and illumination intensity dependent J-V analysis of $Cu_2ZnSn(Se_{0.3}S_{0.7})_4$ monograin layer solar cells

The studied $Cu_2ZnSn(S_xSe_{1-x})_4$ solid solution material had a sulphur to selenium ratio x = 0.71 and the composition $Cu_{1.90}Zn_{1.01}Sn(Se_{0.29}S_{0.71})_{3.88}$ as determined by the energy dispersive X-ray analysis (EDX).

I–V curves of a CZTSSe MGL solar cell measured at different temperatures under 100 $mW/cm^2$ illumination are presented in Fig. 9. It can be seen that increasing the temperature leads to a decrease of $V_{oc}$ and an increase of $I_{sc}$, as expected according to the theory.
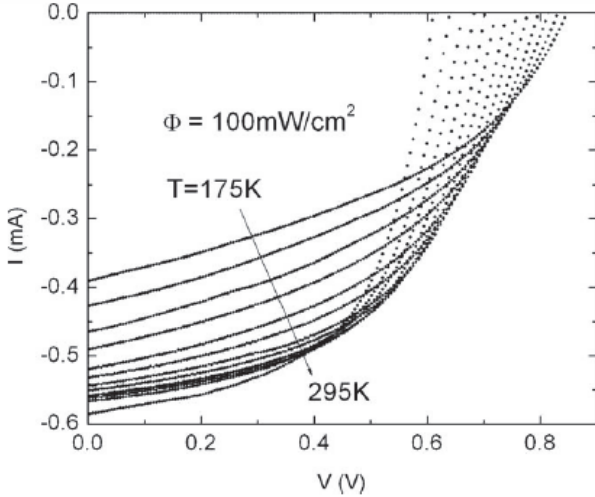


Figure 9: Temperature dependence of I–V curves of CZTSSe monograin solar cells obtained in a light intensity of 100 $mW/cm^2$.

The thermal behaviour of the $V_{oc}$ under different light intensities is shown in Fig. 10. As shown here, with an illumination intensity of 100 $mW/cm^2$, the open-circuit voltage $V_{oc}$ increases with a decreasing temperature by 1.91 mV/K. According to Eq. (8), the linear behaviour for all light intensities indicates that the temperature dependence of $n$ and of $J_{00}$ has only a minor effect on the temperature dependence of $V_{oc}$. According to theory, all $V_{oc}(T)$ curves measured for different intensities must show different slopes but the same $E_A$ at 0 K. In case of bulk recombination $E_A \approx E_g$ where $E_g$ is the band gap energy of the absorber material. The extrapolation to 0 K results in $E_A \approx 1.2$ eV for all intensities. This is consistent with the spectral response [35] and photoluminescence [20] measurements and shows that $E_A \approx E_g$ in this material. This, in turn, is direct evidence that in these CZTSSe MGL solar cells, the dominating recombination (at least at temperatures close to room temperature) is a recombination in the space-charge region. All the measured $V_{oc}(T)$ curves

were fitted with linear functions and the corresponding fitting parameters are given in Table 1.
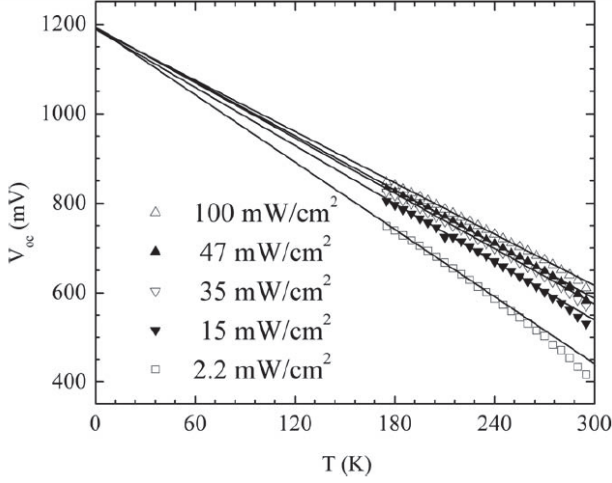


Figure 10: Open-circuit voltage $V_{oc}$ of the CZTSSe MGL cell as a function of temperature illuminated with different light intensities. The straight lines are linear fits of Eq. (8).

Especially important is the temperature dependence of the relative efficiency $\eta$ of solar cells. Therefore, we plotted also $\eta(T)$ curves measured at different light intensities, see Fig. 11. Calculated efficiencies are not calibrated because we used a simple halogen light source and therefore AM1.5G spectral conditions were not followed. It can be seen that the efficiencies have a maximum value below room temperature. The corresponding maximum efficiency temperature increases with light intensity and at 100 mW/cm$^2$, it is at about 250 K. At low temperatures, the efficiency starts to decrease with decreasing temperature. The same decrease can be observed with increasing the temperature above 250 K. At this "high" temperature region, the decrease of the efficiency is nearly linear with temperature. Table 1 shows the corresponding slopes. This curved $\eta(T)$ dependence is caused by the temperature dependence of the fill factor $FF$.

Table 1: Parameters obtained from fitting temperature dependent J–V curves

| $\Phi$ (mW/cm$^2$) | $-dV_{oc}/dT$ (mV/K) | $E_A$ (meV) | $d\eta/dT$ (%/K) |
|---|---|---|---|
| 100 | 1.91 | 1190 | -0.013 |
| 47 | 2.02 | 1193 | -0.016 |
| 35 | 2.06 | 1193 | -0.020 |
| 15 | 2.17 | 1189 | -0.022 |
| 2.2 | 2.51 | 1193 | -0.025 |

Figure 11: Temperature dependence of the relative efficiency $\eta$ of a CZTSSe MGL solar cell illuminated with different light intensities. Linear fitting was used for the high temperature region and fitting results are presented as lines.

Measured temperature coefficients of CZTSSe MGL solar cells indicate that in many cases they are lower than those of other types of solar cells. For example, Cu(In,Ga)Se$_2$ cells usually show $dV_{oc}/dT$ values from -2.01 to-3.3 mV/K and $d\eta/dT$ values from -0.017 to -0.064%/K [81]. Si cells show $dV_{oc}/dT$ values from -2.07 to -2.17 mV/K and $d\eta/dT$ value about -0.042%/K [82]. The same is true in CdTe cells, where $dV_{oc}/dT$ is typically in the range of -2.1 to -2.2 mV/K [83]. These low values of measured temperature coefficients of CZTSSe solar cells show a great potential of this compound.

According to Eq. (5), a semi logarithmic plot of $I_{sc}$ versus $V_{oc}$ will yield a straight line for high-enough $V_{oc}$. From this slope, $n$ can be calculated if one knows the temperature. $I_0$ can be found by taking the intercept of the straight part of the plot with the $I_{sc}$-axis. In Fig. 12, $I_{sc}(V_{oc})$ curves for different temperatures are plotted. It can be seen that all curves show a simple exponential behaviour. All experimental curves were fitted using the exponential part of Eq. (5). Fitting results show that the diode ideality factor $n$ exhibits no remarkable temperature dependence and only slightly increases from $n = 1.85$ to $n = 2.05$ in the temperature range $T = 175$–300 K. This is quite surprising because in most solar cells, the ideality factor decreases with temperature [72, 84]. One reason for this different trend in our cells can be the temperature dependent bulk recombination current, which increases at higher temperatures. Therefore, we observe an ideality factor very close to $n = 2$.
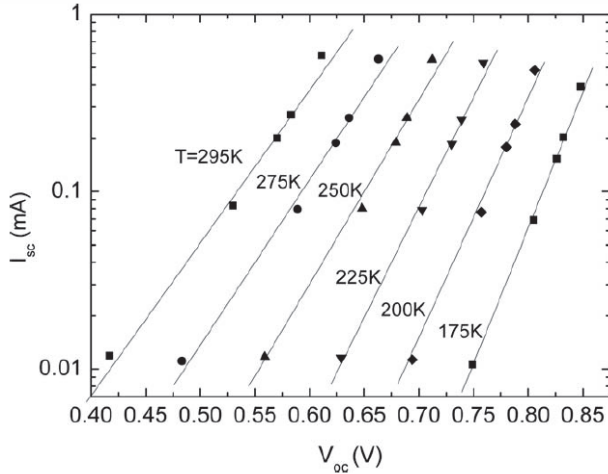
Figure 12: $I_{sc}$–$V_{oc}$-curves for temperatures in the range of 175–295 K. Every measurement was done with five different illumination intensities ranging from 2.2 to 100 mW/cm². Lines represent the least square fit, showing good correlation with Eq. (5).

From Fig. 12, we also extracted $I_0$ values and the temperature dependence of $I_0$ is shown in Fig. 13. We fitted these calculated points with Eq. (7), by using an average value on $n$ ($n = 1.87$). Although this fitting is not very accurate, we still obtained $E_A = 1.24$ eV, which is very close to the $E_A$ value we found using $V_{oc}(T)$ curves. This coincidence supports our assumptions regarding the role of $R_{sh}$ and $R_S$ and the use of a simplified theoretical model where we did not directly take into account the decrease of the band gap energy with temperature.
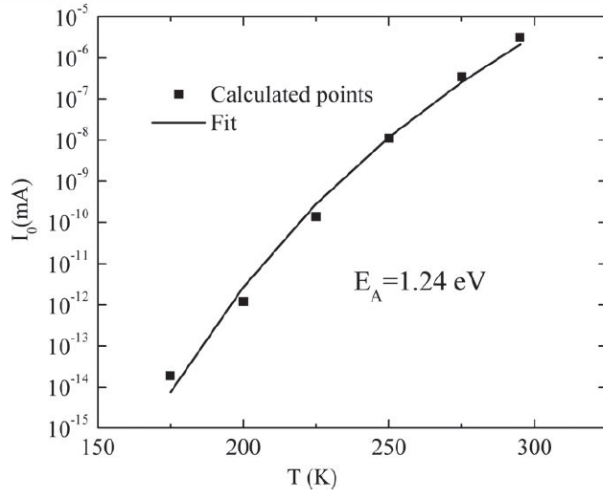


Figure 13: $I_0$–$T$ -graph. Experimental points were fitted using Eq. (7).

## 4.2 Temperature dependent EQE analysis of $Cu_2ZnSnSe_4$ monograin layer solar cells

The chemical composition Cu/(Zn+Sn) = 0.87; Zn/Sn = 0.97 of the studied monograin powder was determined by the EDX. In the record cells, the composition Cu/(Zn+Sn) = 0.8; Zn/Sn = 1.22 was reported [85]. In our experiment, crystals were Cu-poor and slightly Sn-rich while in record cells [85] Zn-rich composition was used. The CZTSe phase was confirmed by the X-ray diffraction (XRD) measurements.

A typical J–V curve of a CZTSe cell is shown in Fig. 14. It can be seen that this CZTSe cell has quite low solar cell parameters. Especially low is the open-circuit voltage $V_{oc}$. In this cell, we assume to have quite large recombination losses. However, we see that even this "bad" cell generates current and therefore it is possible to use it to study the temperature dependence of its quantum efficiency.
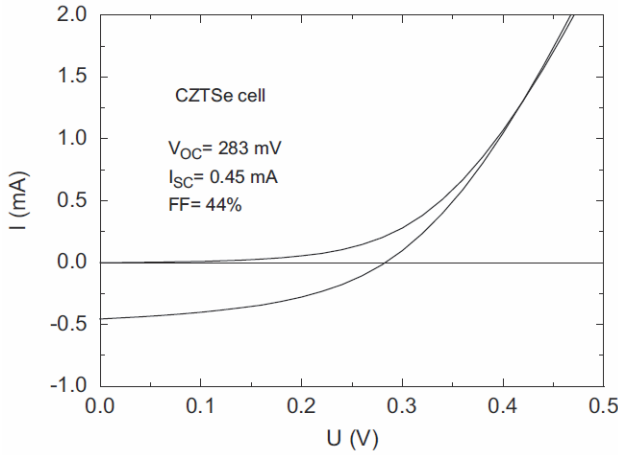


Figure 14: Dark and light I–V curves of CZTSe cell measured at room temperature.

The low-energy side of the EQE spectrum near the band gap energy $E_g$ of the absorber can be fitted by the equation of Klenk and Schock [86]:

$$QE = K\left(1 - \exp\left(-\alpha L_{eff}\right)\right), \tag{15}$$

where $L_{eff} = W + L_d$ is the effective diffusion length of minority carriers, $L_d$ is their diffusion length in the absorber material, $W$ is the width of the depletion region, and $\alpha$ is the absorption coefficient of the absorber material. The constant $K$ is unity in absolute measurements. It is obvious that in the case of a compensated absorber material, the effective diffusion length of majority carriers must also be taken into account. Therefore, in compensated CZTSe, we expect to see a more pronounced role of the hole mobility on the temperature dependence of EQE curves.

The fundamental absorption edge in most semiconductors follows an exponential law and for energies $E < E_g$, the absorption coefficient can usually be described by the so-called Urbach rule [87, 88]:

$$\alpha(E) = \alpha_0 \exp\left[\frac{\sigma}{kT}(E - E_0)\right] \quad , \tag{16}$$

where $\sigma$ is a steepness parameter, and $E_0$ and $\alpha_0$ are characteristic parameters of the material.

Assuming that in this region EQE is mostly determined by the absorption coefficient, i.e.

$$QE \cdot E(E) \propto \alpha(E) \tag{17}$$

the $QE \cdot E$ curves must also have an exponential part where it is possible to find $\sigma$, $E_0$, and $\alpha_0$. Indeed, Fig. 15 shows the exponential part of the $QE \cdot E$ curves at different temperatures.
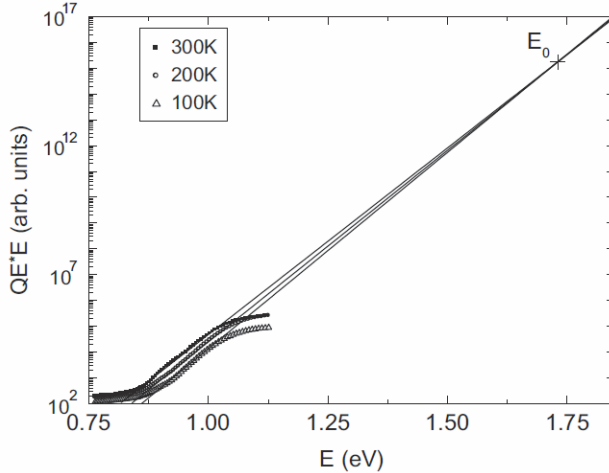


Figure 15: Typical $QE \cdot E$ curves obtained at different temperatures showing the exponential Urbach behaviour with $E_0$ at 1.73 eV. Solid lines are the fitting results with Eq. (16).

All these $QE \cdot E$ curves were fitted using Eq. (16). From these fits, we found $E_0$ and the temperature dependence of the steepness parameter $\sigma$, as shown in Fig. 16. It should be mentioned that at low temperatures, where $T < 60$ K we have slightly lower $E_0$ values. One reason for this could be a too low mobility of carriers on the EQE curve at very low temperatures. Therefore, the assumed relation (17) is not valid any more in this temperature region.

The data from Fig. 16 are fitted to the following empirical relation [87, 88]:

$$\sigma = \sigma_0 (2kT/\hbar\omega_p)\tan h(\hbar\omega_p/2kT) , \tag{18}$$

where $\sigma_0$ is a constant and $\hbar\omega_p$ the energy of the phonons associated with Urbach's tail. According to the fitting results, we obtained $\hbar\omega_p = 85$ meV (686

cm[-1]) and $\sigma_0$ = 1.46. Our latest Raman measurements showed that the highest phonon energy in CZTSe is about 250 cm^{-1} [20]. It was shown [89, 90, 91] that in the case of a structural and electronic disorder, the corresponding phonon energy found from Urbach's tail always seems to be much higher than the energy of measured phonon modes. For example, in CuInSe$_2$, phonon energies as high as 60 meV were found from Urbach's tail measurements while the highest optical mode energy obtained from Raman measurements was only 29 meV [91]. Similarly, in our CZTSe crystals with their quite high defect concentrations, the high value of the observed phonon energy seems to be realistic. The most important result of this kind of analysis is that we really can use EQE curves to obtain information about the behaviour of the absorption coefficient.
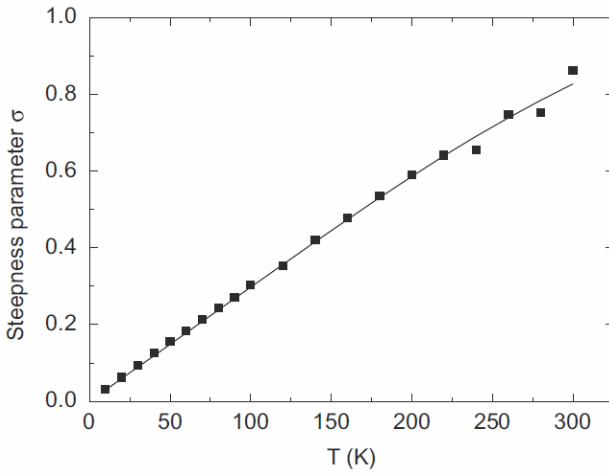


Figure 16: Temperature dependence of the steepness parameter $\sigma$. Solid line represents the fit using Eq. (18).

Above the exponential tail, the absorption coefficient of a direct band semiconductor has been observed to obey the equation: $\alpha(E) = B(E - E_g)^{1/2}$. If the absorption coefficient is small, i.e., near the band gap energy $E \approx E_g$, then Eq. (15) can be simplified as

$$QE \approx K\alpha L_{eff} \approx A\left(E - E_g^*\right)^{1/2} \big/ E \,, \tag{19}$$

where $E_g^*$ is an effective band gap energy and constant $A$ includes all the parameters that are independent of $E$. Therefore, $(E \cdot QE)^2$ vs. $E$ curves should have a linear segment from which a value for $E_g^*$ can be found. In the case of spatial potential fluctuations, the effective band gap energy is lower than the band gap energy of the "ideal" semiconductor without potential fluctuations, because the shape of the $\alpha(E)$ curve does not completely follow the $E^{1/2}$ rule, see for example [92]. At low temperatures, in particular, when electrons and holes

can occupy localized states inside the potential wells, the difference between $E_g$ and $E_g^*$ can be rather large. At the same time, when potential fluctuations are very small, we will often find $E_g \approx E_g^*$ [92].

Typical EQE curves measured at different temperatures are given in Fig. 17. All curves have an $E^{1/2}$ behaviour in the energy range of about $E = 1.02–1.12$ eV. From these curves, $E_g^*$ was found for every temperature used, see Fig. 18.
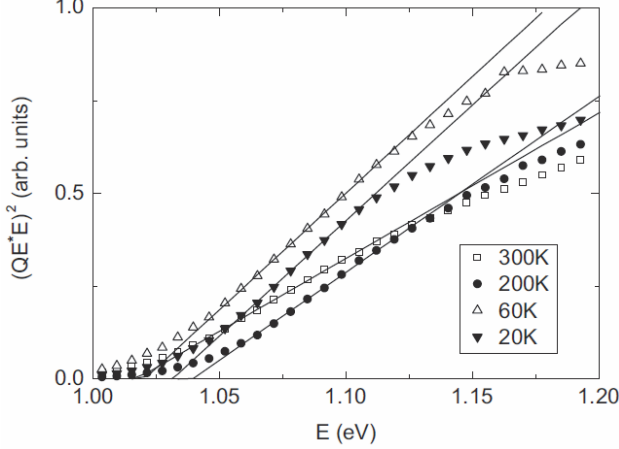


Figure 17: Normalised EQE curves vs. photon energy measured at different temperatures. Solid lines are fits using Eq. (19).

It can be seen from Fig. 18 that at low temperatures, $E_g^*$ is almost constant but drops at $T = 60$ K. At $T > 60$ K, the effective band gap energy increases with the temperature until at $T \approx 250$ K it starts to decrease again. The overall increase of $E_g^*$ at $T = 60–250$ K is about 23 meV.

This kind of dependence can be explained if we take deep potential fluctuations into account in our sample. It is obvious that EQE depends not only on the absorption coefficient but also on the ability of generated charge carriers to reach the front and back contacts. At low temperatures, in particular, the heavier holes tend to localize inside the potential wells. Although at low temperatures, we probably have absorption at $E < E_g$, here the EQE curves show no remarkable current. The reason could be that this spectral region belongs to the deepest potential wells and the generated holes cannot move and hence the EQE remains small. Therefore, we started to measure a current only at higher photon energy, where the potential wells are not so deep and photo-generated holes can move. At higher temperatures, also the current generated from the deepest wells increases. They can now move and thus the decrease of the effective band gap energy is small at $T = 60$ K. Because the concentration of these deep wells is small and only a fraction of all charges is liberated, we should see here also a decrease in the integrated EQE at the same temperature.
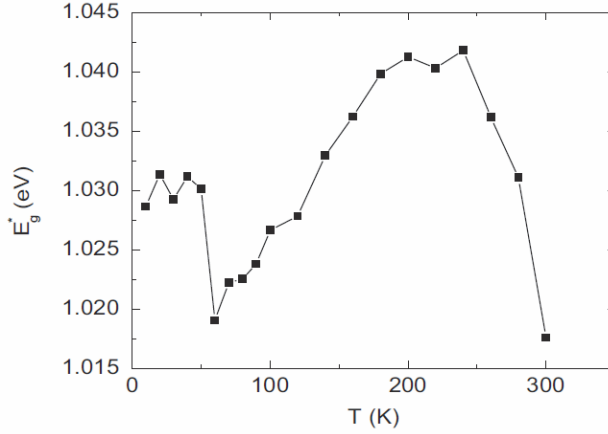
Figure 18: The temperature dependence of the effective band gap energy $E_g^*$.

The temperature dependence of the integrated quantum efficiency $\Phi$ is given in Fig. 19. In the range of $T = 60$–$250$ K, we see an increase of $\Phi$ with temperature. It is obvious that this increase is related to thermally activated liberation of charges from the potential wells. If we assume that the average depth of these energy wells is $\gamma$, then there must be a temperature region where

$$\Phi = \Phi_0 \exp(\gamma/kT) \tag{20}$$

Indeed, from the inset of Fig. 19 we see that the fit to Eq. (20) gives $\gamma = 25 \pm 1$ meV. This energetic depth correlates with the shift of $E_g^*$ with temperature in the same region if we also take the decrease of the band gap energy with temperature into account. Therefore, the observed shift of $E_g^*$ is slightly smaller than $\gamma$.
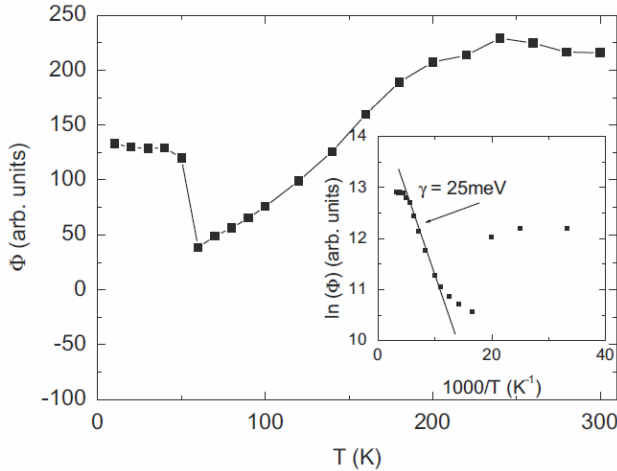


Figure 19: Temperature dependence of the integrated quantum efficiency $\Phi$. The inset shows an exponential part fitted with Eq. (20).

The value of $\gamma$ found from the EQE curves is actually very close to the corresponding value obtained from photoluminescence measurements, for which $\gamma = 24$ meV was determined for our CZTSe crystals [21].

At higher temperatures, all charges possess enough activation energy to be free and therefore $E_g^* \approx E_g$. From Fig. 18, we can find the band gap energy for CZTSe at room temperature to be $E_g = 1.017$ eV. Our previous PL studies [20] showed that the low temperature band gap energy of CZTSe must be in the range of 1.02 eV. The band gap energy obtained from EQE curves confirms this value. It is obvious that if the concentration of majority carriers (holes) is high, then EQE is mainly determined by the effective diffusion of minority carriers (electrons). At the same time, electrons generally have a smaller effective mass and therefore they usually have no localized states inside the potential wells. Therefore in this case, the temperature dependence of EQE curves should not show such a pronounced shift of the effective band gap energy with temperature. Thus, this kind of analysis is more suitable for compensated absorber materials and can be used to study spatial potential and probably also compositional fluctuations in these materials.

## 4.3 Temperature and illumination intensity dependent J-V and EQE analysis of $Cu_2ZnSnS_4$ monograin layer solar cells

This section presents the results of the temperature and illumination intensity dependent J-V and EQE analysis of $Cu_2ZnSnS_4$ MGL solar cells. The CZTS room temperature J-V characteristics of a studied CZTS MGL solar cells showed the following properties: open-circuit voltage $V_{oc} = 709$ mV, short-circuit current density $J_{sc} = 13.8$ mA/cm$^2$, fill factor $FF = 61.4$ %, and efficiency $\eta = 6.0$ %. Due to the peculiarity of the MGL solar cell structure, the active area where the photocurrent is actually produced is smaller than the analysis area.
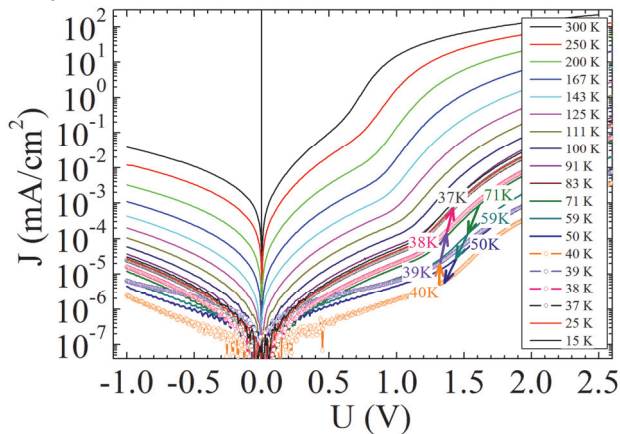


Figure 20: Temperature dependence of dark J-V curves.

The active area is estimated to be 75% of the back contact area after excluding the area of the binder material between the absorber material powder crystals. After such consideration, the current density per absorber material active area is estimated at $J_{sc}^{abs.}$ = 18.4 mA/cm$^2$ and the efficiency is estimated at $\eta^{abs.}$ = 8.0%. In spite of that, solar cell parameters are still limited due to recombination and parasitic losses. The series resistances obtained from the light and the dark J-V curves determined at room temperature by the process described by Hegedus and Shafarman [66] are rather high, $R_s^{light}$ = 3.6 Ωcm$^2$ and $R_s^{dark}$ = 4.5 Ωcm$^2$, accordingly. The temperature dependence of the series resistance $R_s$ was found from Fig. 20 by the procedure described in section 2.5.

The thermal behaviour of the $V_{oc}$ under different light intensities is shown in Fig. 21. It is known [I] that the temperature dependence of $V_{oc}$ near room temperature can be expressed as Eq. (6). In general, the activation energy $E_A$ and also $J_{00}$ depend mainly on the dominating recombination mechanism in the solar cell. In case of bulk recombination $E_A \approx E_g$, where $E_g$ is the band gap energy of the absorber material. The band gap energy of CZTS slightly depends on the type of crystal structure [55], but is usually higher than 1.5 eV. In our sample, $E_A \approx 1.26$ eV was determined from the $V_{oc}(T)$ plot (see Fig. 21). In general, according to the theory [74], at $E_A < E_g$, the interface recombination is dominating.
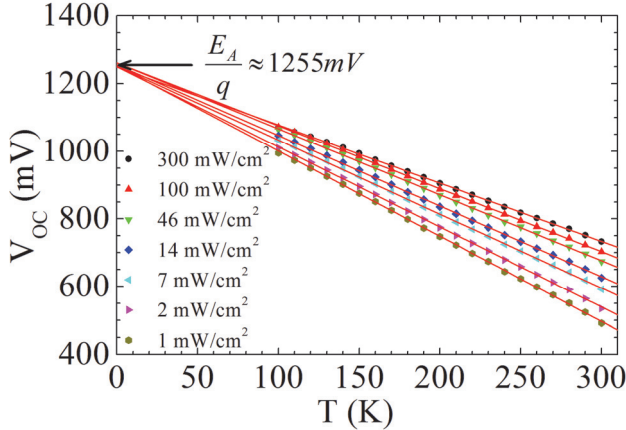


Figure 21: Temperature dependence of $V_{oc}$ measured at different light intensities.

The temperature dependence of the series resistance $R_s$ found using Fig. 20 is shown in Fig. 22a where three different regions can be distinguished. At temperatures $T > 90$ K (region I), $R_s$ decreases with increasing temperature, indicating the thermal activation of carriers [93]. In this region, $R_s$ can be presented as:

$$R_S = R_{S0} \exp(E_A/kT), \tag{21}$$

where the exponential prefactor $R_{S0}$ contains all the parameters that are independent or weekly dependent on temperature. Using Eq. (21), the activation energies $E_{A,\,d} = 87 \pm 3$ meV and $E_{A,\,l} = 43 \pm 1$ meV for dark and light curves were found, respectively. These activation energies are in the same range as those found in [43, 50, 94].
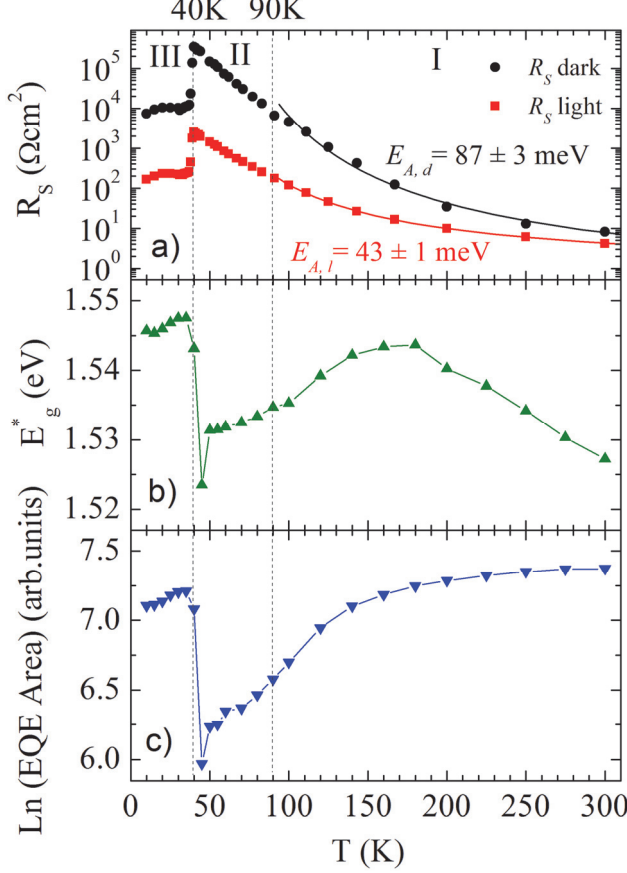


Figure 22: Temperature dependencies of the series resistance $R_s$ obtained from the dark and light J-V curves (a), the effective band gap energy $E_g^*$ (b), and integrated EQE area(c). Solid lines correspond to the fitting of Eq. (15) to the experimental data.

At intermediate temperatures ($T = 90$–$40$ K, region II), the dependence of the series resistance on temperature changes and a typical M-VRH conduction starts to dominate [95]. This type of behaviour is expected in all heavily doped materials where spatial potential fluctuations create deep potential wells for holes [21, 50, 96]. At the same time, we also expect the increasing role of bulk recombination in this temperature region and therefore the M-VRH model is not completely valid here. At about $T = 40$ K, a rapid change of $R_s$ can be seen. In the low temperature region ($T < 40$ K, region III), $R_s$ drops down more than

one order of magnitude and remains almost constant down to the lowest measured temperature. At these very low temperatures, generated holes are unable to tunnel through the potential barrier into the interface region between CZTS and CdS and therefore, the interface recombination rate must be very low.

Quantum efficiency measurement is a well-known method to describe optical and electronic losses in solar cell devices. From the low-energy side of the EQE curve, i.e., near the band gap energy $E \approx E_g$, the effective band gap energy $E_g^*$ can be determined [II] by the approximation (15) used in Section 3.2. Consequently, the $E_g^*$ value can be determined from a plot of $\left(E \cdot EQE\right)^2$ vs. $E$ at the low energy side of the EQE spectrum. Therefore, temperature dependence of a quantum efficiency curve presented in Fig. 23 can be used to analyse the temperature dependence of the effective band gap energy.
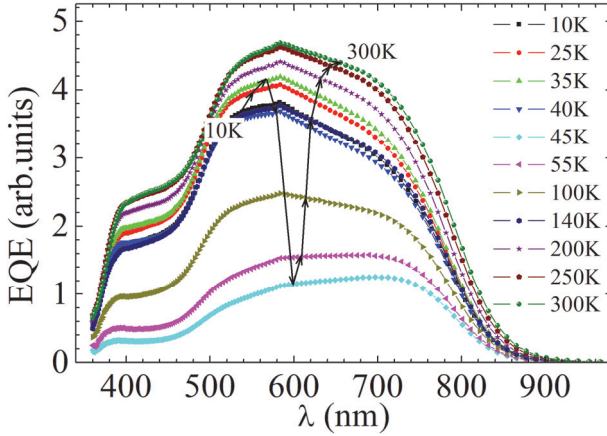


Figure 23: Temperature dependence of EQE at 0 V. The arrows guide the trend of the EQE temperature dependence.

The temperature dependencies of the series resistance $R_s$, the effective band gap energy $E_g^*$ and the integrated EQE are presented in Fig. 22. It can be seen (Fig. 22b) that in the temperature region from room temperature to $T = 180$ K, $E_g^*$ follows the model of temperature dependence of the band gap energy proposed by K.P. O'Donnell and X. Chen [75]. Then $E_g^*$ starts to decrease with further decreasing of the temperature until the "critical" temperature at about 40 K where the rapid increase of $E_g^*$ starts. Similar behaviour can be seen for integrated EQE, see Fig. 22c. It was shown in [II] that the changes at 40 K < $T$ < 180 K are related to the localization of holes inside deep valence band potential wells. As a result, an exponential Urbach tail starts to affect the absorption and the effective band gap $E_g^*$ starts to decrease due to holes localization in deeper potential wells. At the same time, hole mobility also decreases and the bulk recombination through these deep wells increases, reducing the overall EQE.

45

The observed sudden increase of $E_g^*$ to the "normal" band gap value $E_g$ at 40 K together with the increase of the generated current (EQE) and decrease in $R_s$ have to be related to the step-like change in the Fermi level position at the interface. This change could cause the blocking of hole transport to the interface states and as a result, the interface recombination decreases. This is why the photocurrent and $E_g^*$ increase. However, there might be also other processes taking place, causing the same kind of behaviour. Consequently, further studies are needed to explain this peculiar behaviour of the CZTS solar cell parameters at very low temperatures.

# CONCLUSIONS

From the temperature dependent current–voltage parameter analysis of the $Cu_2ZnSn(Se_xS_{1-x})_4$ MGL solar cells, the following conclusions were made:

- for a light intensity of 100 mW/cm$^2$, the temperature coefficient is $dV_{oc}/dT$ = -1.91 mV/K and the activation energy $E_A$ is close to the value of the band gap energy of 1.2 eV;
- the diode ideality factor $n$ is close to a value of 2 and shows very small increase with temperature; as a result, the dominating recombination is related to recombination in the space-charge region;
- the relative efficiency of the solar cell decreases with temperature with a slope of 0.013%/K. The temperature coefficient measured indicates that in many cases it is lower than that of other types of solar cells.

From the temperature dependent quantum efficiency analysis of the $Cu_2ZnSnSe_4$ MGL solar cells, the following conclusions were made:

- temperature dependence of the effective band gap energies and the average depth of potential wells of 25 meV of $Cu_2ZnSnSe_4$ absorber were calculated by the use of low energy side of the quantum efficiency curves; the determined value of potential wells was found to agree very well with the value determined in photoluminescence measurements;
- it was shown that the room temperature band gap energy of $Cu_2ZnSnSe_4$ is $E_g$ = 1.017 eV.

From the temperature dependent analysis of $Cu_2ZnSnS_4$ MGL solar cells, the following conclusions were made:

- the main recombination losses are related to interface recombination that was found to be blocked at $T < 40$ K;
- part of the losses originate also from bulk recombination, associated to potential fluctuations of the valence band edge.

# ACKNOWLEDGEMENTS

I would like to express my deepest gratitude to my supervisor Prof. Jüri Krustok for his support, encouragement and helpful discussions over the years of studies.

I would also like to thank Prof. Enn Mellikov for giving me the opportunity to join the research group at the Chair of Semiconductor Materials Technology.

I am very thankful to all my friendly colleagues in the Chair of Semiconductor Materials Technology, especially to Dr. Andri Jagomägi, Dr. Maarja Grossberg, Dr. Taavi Raadik, Dr. Raavo Josepson and PhD student Erkki Kask for their advice and support in Photoluminescence, Raman, and opto-electrical analysis.

The monograin-team at TUT composed of Dr. Mare Altosaar, Dr. Marit Kauk-Kuusik, Dr. Jaan Raudoja, Dr. Kristi Timmo, Dr. Tiit Varema, PhD student Maris Pilvet is greatly acknowledged for the samples provided.

My warmest gratitude belongs to my family, Marika and sons Sebastian and Simon for their support and love. I am also grateful to one of my dearest friends Mariliis Peettamm for the backing and inspiring me through difficult times.

Tallinn, April 2016

Mati Danilson

# ABSTRACT

This thesis is focused on the studies of temperature dependent electrical properties of monograin layer (MGL) solar cells with the kesterite type absorber materials: $Cu_2ZnSnS_4$ (CZTS), $Cu_2ZnSnSe_4$ (CZTSe), and $Cu_2ZnSn(S_{0.7}Se_{0.3})_4$ (CZTSSe).

These multinary kesterite type semiconductor compounds are promising absorber materials for photovoltaic applications. These materials are direct band gap semiconductor compounds with a high absorption coefficient. Their band gap energy is in the favourable range for optimal solar energy conversion and their constituent elements are abundant and non-toxic. Currently, the power conversion efficiency ($\eta$) record of solar cells with kesterite type absorber material has achieved 12.6 %. Still, the main limiting factor of the efficiency of kesterite type solar cells is too large deficit of open-circuit voltage ($V_{OC}$) from the maximum theoretical value. The limited value of $V_{OC}$ is directly related to the recombinational losses, which are related to the bulk and interface defects of the absorber material. The parasitic losses, such as high series resistance, limit the fill factor (*FF*).

Derived from the literature review, the objectives of the present doctoral thesis were set to study the temperature and spectrally dependent electrical properties of MGL solar cells with different kesterite type absorber materials and to identify recombinational loss mechanisms and parasitic losses limiting $V_{OC}$ and *FF*. In order to investigate the current transport properties and recombinational losses, the temperature and illumination intensity dependent current-voltage (J-V) and external quantum efficiency (EQE) measurements were conducted. Another aim of the study was to propose a new simple method by using temperature dependent EQE analysis to investigate the spatial electrostatic potential fluctuations in the kesterite-based solar cells.

The extrapolation of $V_{OC}$ to 0 K under different light intensities in CZTSSe MGL solar cells results in the activation energy ($E_A$) value of 1.2 eV. This value is about equal to the band gap energy of the studied CZTSSe absorber material. The extrapolated value is in accordance with the data found by photoluminescence (PL) and EQE measurements. This, in turn, is direct evidence that in CZTSSe MGL solar cells, the dominating room temperature recombination process is related to the recombination in the space-charge region. At the same time, the extrapolation of $V_{OC}$ to 0K in CZTS MGL solar cells results in the $E_A$ value of 1.26 eV. According to the PL and EQE data, the band gap energy of CZTS material at room temperature is about 1.5 eV. Based on the PL data and according to the theory if $E_A$ is smaller than the band gap energy, the dominating recombination process is related to the recombination in the interface region.

The temperature dependencies of the saturation current density ($J_0$) and the ideality factors of the CZTSSe and CZTS MGL solar cells were obtained from the *J-V* curve measurements at different illumination intensities. For both

absorber materials, the fitting of $J_{SC}$-$V_{OC}$ curves shows that the ideality factor is weakly temperature dependent in the wide temperature range. The temperature dependence of the $J_0$ of the CZTSSe MGL solar cells yields the $E_A$ value of 1.24 eV, which is comparable to the value found from the $V_{OC}(T)$ data. This is in accordance with the value of the band gap energy found by PL and EQE analysis and supports the assumption of the recombination in the space-charge region. The temperature dependence of the $J_0$ of the CZTS MGL solar cells results in the $E_A$ value of 1.28 eV, which is in good agreement with the value found from the $V_{OC}(T)$ dependence experiment.

The relative efficiency of CZTSSe MGL solar cells was found to decrease with the increasing temperature by -0.013 %/K. The measured temperature coefficient indicates that according to the literature, it is lower than for solar cells made from other types of absorber materials, for example Cu(In,Ga)Se$_2$, CdTe and Si. The curved $\eta(T)$ dependence is common for all kesterite MGL solar cells and is caused by the temperature dependence of the $FF$, which in turn, is caused by the magnitude and the temperature dependence of the series resistance.

The temperature dependences of the effective band gap energies ($E_g{}^*$) of MGL solar cells based on CZTS and CZTSe absorber materials were found very similar in their behaviour. The temperature dependence of the $E_g{}^*$ can be divided into three different regions. At temperatures around room temperature, $E_g{}^*$ follows the model describing the temperature dependence of the band gap energy. Then at about 250 K for pure selenide and at about 180 K for pure sulphide, the $E_g{}^*$ values start to decrease while temperature decreases. This uncommon behaviour of $E_g{}^*$ is explained by the presence of potential fluctuations where the charge carriers relaxed to the deeper states of potential wells can be photo-generated by the photons with energy smaller than the band gap energy to contribute to the photocurrent. For pure selenide at about 60 K and for pure sulphide at about 40 K, $E_g{}^*$ does a step-like change to a higher but rather temperature independent value. This sudden rise of $E_g{}^*$ at very low temperatures can be explained by the decreased mobility of the holes that are generated from the deepest potential wells. As a result, charge carriers photo-generated by the higher photon energies can contribute to the photocurrent collection.

At the same time, the step-like change of the Fermi level position at the interface could block of the hole transport to the interface states. As a result, the interface recombination decreases and the photocurrent collection increases. This hypothesis is supported by the step-like change in the absolute value of the photocurrent of the solar cells. For CZTSe at about 60 K and for CZTS at about 40 K, the sudden rise of the photocurrent to the rather constant value was measured. The scale of the spatial potential fluctuations with the average energetic depth ($\gamma$) of 25 meV for the CZTSe and 12 meV for the CZTS MGL solar cells was calculated from the integrated EQE area data. In both cases, the $\gamma$ value found from EQE is in good correlation with the corresponding value obtained from the PL measurements.

# KOKKUVÕTE

Antud doktoritöö on keskendunud kesteriitse struktuuriga puhastest nelikühenditest $Cu_2ZnSnS_4$ (CZTS) ja $Cu_2ZnSnSe_4$ (CZTSe) ning nende tahkest lahusest $Cu_2ZnSn(S_{0.7}Se_{0.3})_4$ (CZTSSe) valmistatud monoterakihiliste päikesepatareide elektriliste omaduste temperatuursõltuvuste uurimisele.

Kesteriitse struktuuriga mitmikpooljuhtühendid on lootustandvad materjalid rakendamiseks päikeseenergeetikas. Need on otsese ja optimaalse keelutsooni laiusega pooljuhtmaterjalid, millel on suur neeldumiskoefitsient ja mis koosnevad laialdaselt maakoores levinud mittetoksilistest elementidest. Seni on kesteriitide baasil valmistatud päikesepatarei suurimaks efektiivsuseks ($\eta$) mõõdetud 12,6 %. Kesteriitse struktuuriga absorbermaterjalidest valmistatud päikesepatareide kõige põhilisemaks efektiivsust piiravaks teguriks loetakse liiga suurt erinevust avatud-ahela pinge ($V_{OC}$) ja selle maksimaalse võimaliku teoreetilise väärtuse vahel. $V_{OC}$ puudujääk on otseselt seotud rekombinatsiooniliste kadudega, mis on tingitud suurest defektide hulgast absorbermaterjalis ja selle piirpindadel. Teiseks oluliseks efektiivsust piiravaks teguriks on erinevad parasiitkaod (näiteks liiga suur järjestiktakistus), mis vähendavad täituvusastet ($FF$).

Kirjandusülevaates välja toodud probleemidest lähtuvalt seati doktoritöö eesmärkideks uurida erinevate kesteriitse struktuuriga absorberitega monoterakihiliste päikesepatareide elektriliste omaduste temperatuur- ja spektraalsõltuvusi eesmärgiga selgitada välja võimalikud rekombinatsiooniliste kadude mehhanismid ja parasiitkaod, mis piiravad $V_{OC}$ ja $FF$ väärtusi. Voolu transpordiomaduste ja rekombinatsiooniliste kadude mehhanismide uurimiseks teostati voolu-pinge sõltuvuste ($J$-$V$) ja kvantefektiivsuse (EQE) mõõtmisi erinevatel temperatuuridel ja sõltuvalt valgustamise intensiivsusest. Samuti oli töö eesmärgiks pakkuda välja lihtne meetod elektrostaatiliste potentsiaali-fluktuatsioonide uurimiseks kesteriitse struktuuriga päikesepatareides kasutades EQE temperatuursõltuvuste analüüsi.

Erinevate valguse intensiivsustega mõõdetud $V_{OC}$ temperatuursõltuvuste ekstrapoleerimisel 0 K juurde määrati $Cu_2ZnSn(S_{0.7}Se_{0.3})_4$ päikesepatareis laengukandjate aktivatsiooni-energia $E_A$ väärtuseks 1,2 eV. See tulemus on kooskõlas fotoluminestsentsi (PL) ja EQE meetoditel saadud tulemustega ning on ligikaudu võrdne antud absorbermaterjali keelutsooni laiusega. See kokkulangevus kinnitab, et CZTSSe absorbermaterjaliga monoterakihilises päikesepatareis domineerib toatemperatuuri lähedastel temperatuuridel siirdel toimuv rekombinatsioon. $Cu_2ZnSnS_4$ absorbermaterjaliga monoterakihilise päikesepatarei $V_{OC}$ temperatuursõltuvuse ekstrapoleerimine 0 K juurde andis tulemuseks 1,26 eV. Tuginedes eelnevalt PL meetodil leitule ja vastavalt teooriale võib järeldada, et juhul kui $E_A$ väärtus on keelutsooni laiusest väiksem, siis domineerivaks mehhanismiks on kontaktpinnal toimuv rekombinatsioon.

CZTSSe ja CZTS monoterakihiliste päikesepatareide küllastusvoolu ($J_0$) ja ideaalsusteguri $n$ temperatuursõltuvuste uurimiseks kasutati pinge-voolu

mõõtmisi erinevatel valguse intensiivsustel. Mõlema absorbermaterjali ideaalsustegurid väärtusega 2 lähedal on peaaegu temperatuurist sõltumatud laias temperatuuride vahemikus. CZTSSe päikesepatarei küllastusvoolu $J_0$ temperatuursõltuvusest leitud $E_A$ väärtus 1,24 eV on lähedane $V_{OC}(T)$ sõltuvusest määratud väärtusega. See tulemus on kooskõlas PL ja EQE meetoditel määratud absorbermaterjali keelutsooni laiusega ja toetab järeldust siirdel toimuva domineeriva rekombinatsiooni kohta. CZTS päikesepatarei küllastusvoolu temperatuursõltuvusest leitud $E_A$ väärtus 1,28 eV on heas kooskõlas $V_{OC}(T)$ sõltuvusest määratud väärtusega.

CZTSSe päikesepatarei efektiivsuse temperatuursõltuvusest saadi suhtelise efektiivsuse muutumise koefitsiendiks -0,013 %/K. See väärtus on madalam võrreldes mitmete teist tüüpi absorber-materjalidega. Efektiivsuse mittelineaarne käitumine on iseloomulik kesteriitse struktuuriga absorbermaterjaliga päikesepatareidele. See on tingitud $FF$ väärtuse sõltuvusest temperatuurist, mis on omakorda tingitud parasiitse järjestiktakistuse temperatuursõltuvusest.

CZTS ja CZTSe absorbermaterjalidega monoterakihiliste päikesepatareide effektiivsete keelutsooni laiuste temperatuursõltuvused $E_g^*(T)$ on väga sarnase käitumisega. $E_g^*$ temperatuursõltuvustes võib esile tuua kolm erinevat piirkonda. Toatemperatuuri ümbruses käitub $E_g^*$ vastavalt keelutsooni laiuse temperatuursõltuvust kirjeldavale mudelile. Seejärel, temperatuuri alanedes, seleniididel alates 250 K ja sulfiididel alates 180 K madalamatel temperatuuridel, hakkab $E_g^*$ hoopiski vähenema. Ebatavalist $E_g^*$ käitumist võib seletada potentsiaalifluktuatsioonide olemasoluga, kus foto-voolu genereeritakse temperatuuri alanedes potentsiaalikaevude üha sügavamatelt täidetud energianivoodelt. 60 K juures seleniidide puhul ja sulfiididel 40 K juures toimub $E_g^*(T)$ käitumises järsk astmeline kasv suurema, kuid temperatuurist suhteliselt sõltumatu väärtuseni. Väga madalatel temperatuuridel toimuvat $E_g^*$ järsku tõusu võib seletada sügavatel energianivoodel foto-genereeritud laengukandjate liikuvuse vähenemisega nii madalatel temperatuuridel.

Samadel madalatel temperatuuridel võib toimuda ka Fermi nivoo asukoha järsk muutus absorbermaterjali ja puhvermaterjali kontaktpinnal, põhjustades aukude liikumise blokeerimist kontaktpinna olekutele, mille tulemusel väheneb kontaktpinna olekutel toimuv rekombinatsioon. Antud hüpotees tugineb päikesepatareis mõõdetud foto-voolu hüppelisele kasvule. Foto-voolu hüppelist kasvu madalatel temperatuuridel on näha nii CZTS kui ka CZTSe absorbermaterjaliga päikesepatareides. Suhteliselt konstantse väärtusega foto-vool ja $E_g^*$ mõõdeti seleniid-absorbermaterjaliga päikesepatareidele alla 60 K ja sulfiid-absorbermaterjaliga päikesepatareidele alla 40 K. Integraalset EQE pindala kasutades määrati potentsiaalifluktuatsioonide keskmiseks sügavuseks ($\gamma$) CZTSe päikesepatareides 25 meV ja CZTS päikesepatareides 12 meV. Mõlemal juhul on EQE kaudu leitud $\gamma$ väärtused heas korrelatsioonis PL mõõtmistelt leitud väärtustega.

# REFERENCES

1.  Global Solar PV Capacity to Reach Nearly 500 GW in 2019, HIS press release, 19 March 2015.
2.  .S. te Velde, G.W.M.T. van Helden, Philips Techn. Rev. 29 (1968) 238.
3.  D.Meissner , R.Memming, B.Kastening, Chem. Phys. Lett. 96 (1983) 34.
4.  E. Mellikov, M. Altosaar, J. Raudoja, K. Timmo, O. Volobujeva, M. Kauk, J. Krustok, T. Varema, M. Grossberg, M. Danilson, K. Muska, K. Ernits, F. Lehner, D. Meissner, $Cu_2(Zn_xSn_{2-x})(S_ySe_{1-y})_4$ monograin materials for photovoltaics, Materials Challenges in Alternative and Renewable Energy. Ceramic Transactions 224 (2011) 137.
5.  M. Altosaar, A. Jagomägi, M. Kauk, M. Krunks, J. Krustok, E. Mellikov, J. Raudoja, T. Varema, Monograin layer solar cells, Thin Solid Films 431-432 (2003) 466.
6.  M. Kumar, A. Dubey, N. Adhikari, S. Venkatesan, Q. Qiao, Strategic review of secondary phases, defects and defect-complexes in kesterite CZTS-Se solar cells, Energy Environ. Sci. 8 (2015) 3134.
7.  https://en.wikipedia.org/wiki/Solar_cell
8.  J. Malmström PhD thesis, On Generation and Recombination in Cu(In, Ga)Se2 Thin-Film Solar Cells, Upsala Universitet (2005).
9.  G. Templeton, $0.55 per watt from SolarCity's record-breaking new solar panel, ExtremeTech, 3 October 2015.
10. Renewable energy cost analysis - Solar photovoltaics, IRENA June 2012.
11. Best Research-Cell Efficiencies, NREL Rev.01-11-2016.
12. M.A. Green, K. Emery, Y. Hishikawa, W. Warta, E.D. Dunlop, solar cell efficiency tables (Version 45), Prog. Photovolt: Res. Appl. 23 (2015) 1.
13. http://investor.firstsolar.com/releasedetail.cfm?releaseid=895118
14. P. Jackson, Properties of Cu(In, Ga)Se$_2$ solar cells with new record efficiency up to 21.7%, Phys. Status Solidi RRL 9 (1) (2015) 28.
15. "Solar State of the Market Q3 2008: The Rocky Road to $100 Billion," pp. 90–95, Lux Research, 1 September 2008.
16. K. Ito and T. Nakazawa, Electrical and optical properties of stannite-type quaternary semiconductor thin films, Jpn. J. Appl. Phys. 27 (11) (1988) 2094
17. H. Katagiri, $Cu_2ZnSnS_4$ thin film solar cells, Thin Solid Films 480–481 (2005) 426.
18. I. Repins, N. Vora, C. Beall, S.-H. Wei, Y. Yan, M. Romero, G. Teeter, H. Du, B. To, M. Young and R. Noufi, Kesterites and chalcopyrites: A comparison of close cousins, MRS Symposium Proceedings 1324 (2011).
19. J.S. Seol, S.Y. Lee, H.D. Nam and K.H. Kim, Electrical and optical properties of $Cu_2ZnSnS_4$ thin films prepared by rf magnetron sputtering process, Sol. Energy Mater. Sol. Cells 75 (2003) 155.

20. M. Grossberg, J. Krustok, K. Timmo, M. Altosaar, Radiative recombination in $Cu_2ZnSnSe_4$ monograins studied by photoluminescence spectroscopy, Thin solid Films 517 (2009) 2489.

21. M. Grossberg, J. Krustok, J. Raudoja, K.Timmo, M. Altosaar, T. Raadik, Photoluminescence and Raman study of $Cu_2ZnSn(Se_xS_{1-x})_4$ monograins for photovoltaic applications, Thin Solid Films 519 (2011) 7403.

22. W. Wang, M.T. Winkler, O. Gunawan, T. Gokmen, T.K. Todorov, Y. Zhu, D.B. Mitzi, Device characteristics of CZTSSe thin-film solar cells with 12.6% efficiency, Adv. Energy Mater. 4 (2013) 1301465.

23. T. Kato, H. Hiroi, N. Sakai, S. Muraoka, H. Sugimoto, Characterization of front and back interfaces on $Cu_2ZnSnS_4$ thin-film solar cells, 27th EU PVSEC session 3CO.4.2 (2012) 2236.

24. Y.S. Lee, T. Gershon, O. Gunawan, T.K. Todorov, T. Gokmen, Y. Virgus, S. Guha, $Cu_2ZnSnSe_4$ thin-film solar cells by thermal coevaporation with 11.6% efficiency and improved minority carrier diffusion length, Adv. Energy Mater. 5 (2015) 1401372.

25. A. Neisser, C. Waldauf, T. Holopainen, K. Ernits, S. Moser, D. Meissner, Flexible monograin membrane photovoltaic modules – roadmap to production, 28th EU PVSEC session 3BV.5.4 (2013) ISBN 3-936338-33-7.

26. O. Gunawan, T. Todorov, D. Mitzi, Loss mechanisms in hydrazine-processed $Cu_2ZnSn(Se,S)_4$ solar cells, Appl. Phys. Lett. 97 (2010) 233506.

27. O. Gunawan, T. Gokmen, D.B. Mitzi, Suns-$V_{OC}$ characteristics of high performance kesterite solar cells, J. Appl. Phys. 116, (2014) 084504.

28. M. Grossberg, J. Krustok, A. Jagomägi, M. Leon, E. Arushanov, A. Nateprov, I. Bodnar, Investigation of potential and compositional fluctuations in $CuGa_3Se_5$ crystals using photoluminescence spectroscopy, Thin Solid Films 515 (2007) 6204.

29. J. Just, D. Lützenkirchen-Hecht, R. Frahm, S. Schorr, T. Unold, Determination of secondary phases in kesterite $Cu_2ZnSnS_4$ thin films by x-ray absorption near edge structure analysis, Appl. Phys. Lett. 99 (2011) 262105.

30. I.D. Olekseyuk, I.V. Dudchak, L.V. Piskach, Phase equlibrium in the quazythird-timed system $Cu_2Se$-$ZnSe$-$Cu_2SnSe_3$, Physics and Chemistry of Solid State 1 (2001) 195.

31. I.D. Olekseyuk, I.V. Dudchak, L.V. Piskach, Phase equilibria in the $Cu_2S$–$ZnS$–$SnS_2$ system, J. Alloys Compd. 368 (2004) 135.

32. A. Nagoya, R. Asahi, R. Wahl, G. Kresse, Defect formation and phase stability of $Cu_2ZnSnS_4$ photovoltaic material Phys. Rev. B 81 (2010) 113202.

33. M. Grossberg, J. Krustok, T. Raadik, M. Kauk-Kuusik, J. Raudoja, Photoluminescence study of disordering in the cation sublattice of $Cu_2ZnSnS_4$, Current Applied Physics 14 (2014) 1424.

34. Z. Su, J.M.R. Tan, X. Li, X. Zeng, S.K. Batabyal, L.H. Wong, Cation Substitution of Solution-Processed $Cu_2ZnSnS_4$ Thin Film Solar Cell with over 9% Efficiency. Adv. Energy Mater. 5 (2015) 1500682.

35. M. Altosaar, J. Raudoja, K. Timmo, M. Danilson, M. Grossberg, J. Krustok, E. Mellikov, $Cu_2Zn_{1-x}Cd_xSn(Se_{1-y}S_y)_4$ solid solutions as absorber materials for solar cells, Physica Status Solidi A 205 (2008) 167.

36. S.Y. Chen, X.G. Gong, A. Walsh, S.H. Wei, Crystal and electronic band structure of $Cu_2ZnSnX_4$ (X=S and Se) photovoltaic absorbers: First-principles insights, Appl. Phys. Lett. 94 (2009) 041903.

37. F. Meillaud, A. Shah, C. Droz, E. Vallatsauvain, C. Miazza, Efficiency limits for single-junction and tandem solar cells, Sol. Energy Mater. Sol. Cells 90 (2006) 2952.

38. K. Wang, O. Gunawan, T. Todorov, B. Shin, S.J. Chey, N.A. Bojarczuk, D. Mitzi, S. Guha, Thermally evaporated $Cu_2ZnSnS_4$ solar cells, Appl. Phys. Lett. 97 (2010) 143508.

39. D.B. Mitzi, O. Gunawan, T.K. Todorov, K. Wang, S. Guha, The path towards a high-performance solution-processed kesterite solar cell, Sol. Energy Mater. Sol. Cells 95 (2011) 1421.

40. D.B. Mitzi, O. Gunawan, T.K. Todorov, D. Aaron, R. Barkhouse, Prospects and performance limitations for Cu-Zn-Sn-S-Se photovoltaic technology, Phil. Trans. R. Soc. A 371 (2013) 20110432.

41. M. Grossberg, P. Salu, J. Raudoja, J. Krustok, Microphotoluminescence study of $Cu_2ZnSnS_4$ polycrystals, J. Photon. Energy. 3 (2013) 030599.

42. R. Caballero, C. Guillén, Optical and electrical properties of $CuIn_{1-x}Ga_xSe_2$ thin films obtained by selenization of sequentially evaporated metallic layers Thin Solid Films 431–432 (2003) 200.

43. J.C. González, G.M. Ribeiro, E.R. Viana, P.A Fernandes, P.M.P. Salomé, K. Gutiérrez, A. Abelenda, F.M. Matinaga, J.P. Leitão, A.F. da Cunha, Hopping conduction and persistent photoconductivity in $Cu_2ZnSnS_4$ thin films, J. Phys. D: Appl. Phys. 46 (2013) 155107.

44. M.J. Romero, I. Repins, G. Teeter, M.A. Contreras, M. Al-Jassim, R. Noufi, A comparative study of the defect point physics and luminescence of the kesterites $Cu_2ZnSnS_4$ and $Cu_2ZnSnSe_4$ and chalcopyrite $Cu(In,Ga)Se_2$, IEEE PVSEC (2012) 54140.

45. M. Grossberg, T. Raadik, J. Raudoja, J. Krustok, Photoluminescence study of defect clusters in $Cu_2ZnSnS_4$ polycrystals, Curr. Appl. Phys. 14 (2014) 447.

46. L. Yin, G. Cheng, Y. Feng, Z. Li, C. Yang, X. Xiao, Limitation factors for the performance of kesterite $Cu_2ZnSnS_4$ thin film solar cells studied by defect characterization, RSC Adv. 5 (2015) 40369.

47. R.P. Sharma, A.K. Shukla, A.K. Kapoor, R. Srivastava, P.C. Mathur, Hopping conduction in polycrystalline semiconductors, J. Appl. Phys. 57 (1985) 2026.

48. R. Caballero, C. Maffiotte, C. Guillén, Preparation and characterization of $CuIn_{1-X}Ga_XSe_2$ thin films obtained by sequential evaporations and different selenization processes, thin Solid Films 474 (2005) 70.

49. U. Reislöhner, H. Metzner, C. Ronning, Hopping conduction observed in thermal admittance spectroscopy, Phys. Rev. Lett. 104 (2010) 226403.

50. V. Kosyak, M.A. Karmarkar, M.A. Scarpulla, Temperature dependent conductivity of polycrystalline $Cu_2ZnSnS_4$ thin films, Apl. Phys. Lett. 100 (2012) 263903.

51. M.A. Majeed Khan, S. Kumar, M. Alhoshan, A.S. Al Dwayyan, Spray pyrolysed $Cu_2ZnSnS_4$ absorbing layer: A potential candidate for photovoltaic applications, Opt. Laser Technol. 49 (2013) 196.

52. M. Guc, R. Caballero, K.G. Lisunov, N. López, E. Arushanov, J.M. Merino, M. León, Disorder and variable-range hopping conductivity in $Cu_2ZnSnS_4$ thin films prepared by flash evaporation and post-thermal treatment, J. Alloys Comp. 596 (2014) 140.

53. S.Y. Chen, J.-H. Yang, X.G. Gong, A. Walsh, S.-H. Wei, Intrinsic point defects and complexes in the quaternary kesterite semiconductor $Cu_2ZnSnS_4$, Phys. Rev. B 81 (2010) 245204.

54. E. Kask, T. Raadik, M. Grossberg, R. Josepson, J. Krustok, Deep defects in $Cu_2ZnSnS_4$ monograin solar cells, Energy Procedia 10 (2011) 261.

55. M. Grossberg, J. Krustok, J. Raudoja, T. Raadik, The role of structural properties on deep defect states in $Cu_2ZnSnS_4$ studied by photoluminescence spectroscopy, Appl. Phys. Lett. 101 (2012) 102102.

56. M. Courel, J.A. Andrade-Arvizu, O. Vigil-Galán, Towards a $CdS/Cu_2ZnSnS_4$ solar cell efficiency improvement: A theoretical approach, Appl. Phys. Lett. 105 (2014) 233501.

57. E.T. Yu, J.O. McCaldin, T.C. McGill, Band offsets in semiconductor heterojunctions, Solid State Physics 46 C (1992) 1-146.

58. S.Y. Chen, L.-W. Wang, A. Walsh, X.G. Gong, S.-H. Wei, Abundance of CuZn+SnZn and 2CuZn+SnZn defect clusters in kesterite solar cells, Appl. Phys. Lett. 101 (2012) 223901.

59. D. Huang, C. Persson, Band gap change induced by defect complexes in $Cu_2ZnSnS_4$, Thin Solid Films 535 (2013) 265.

60. K.G. Lisunov, M. Guk, A. Nateprov, S. Levcenko, V. Tezlevan, E. Arushanov, Features of the acceptor band and properties of localized carriers from studies of the variable-range hopping conduction in single crystals of p-$Cu_2ZnSnS_4$, Sol. Energ. Mat. Sol. C 112 (2013) 127.

61. E. Mellikov, M. Altosaar, M. Krunks, J. Krustok, T. Varema, O. Volobujeva, M. Grossberg, L. Kaupmees, T. Dedova, K. Timmo, K. Ernits, J Kois, I. Acik Oja, M. Danilson, S. Bereznev, Research in solar cell technologies at Tallinn University of Technology, Thin Solid Films 516 (2008) 7125.

62. E. Mellikov, D. Meissner, T. Varema, M. Altosaar, M. Kauk, O. Volubujeva, J. Raudoja, K. Timmo, M. Danilson, Monograin materials for solar cells, Solar Energy Materials & Solar Cells 93 (2009) 65.

63. E. Skoplaki, J.A. Palyvos, On the temperature dependence of photovoltaic module electrical performance: a review of efficiency/power correlations, Solar Energy 83 (2009) 614–624.

64. E. Amy de la Breteque, Thermal aspects of c-Si photovoltaic module energy rating, Solar Energy 83 (2009) 1425–1433.

65. M. Gloeckler, Ph.D. thesis, Colorado State University (2005).

66. S.S. Hegedus, W.N. Shafarman, Thin-film solar cells: Device measurements and analysis, Prog. Photovolt: Res. Appl. 12 (2004) 155.

67. D.S.H. Chan, J.C.H. Phang, Analytical Methods for the Extraction of Solar-Cell Single- and Double-Diode Model Parameters from I-V Characteristics, IEEE Transactions on Electron Devices 34 (1987) 286.

68. Ulf Malm PhD thesis, Modelling and degradation characteristics of thin-film CIGS solar cells, Uppsala Universitet (2008).

69. J. Verschraegen, M. Burgelman, J. Penndorf, Temperature dependence of the diode ideality factor in $CuInS_2$-on-Cu-tape solar cells, Thin Solid Films 480-481 (2005) 307.

70. I. Hengel, A. Neisser, R. Klenk, M. Ch. Lux-Steiner, Current transport in $CuInS_2$:Ga/CdS/ZnO – solar cells, Thin Solid Films 361-362 (2000) 458.

71. M.A. Green, Solar Cells, Prentice-Hall, Inc., Englewood Cliffs (1982).

72. U. Rau, H.W. Schock, Electronic properties of $Cu(In,Ga)Se_2$ heterojunction solar cells – recent achievements, surrent understanding, and future challenges, Appl. Phys. A 69 (1999) 131.

73. H. Bayhan, Tunneling-enhanced recombination in polycrystalline CdS/CdTe solar cells, Turk J Phys 30 (2006) 109.

74. V. Nadenau, U. Rau, A. Jasnek, H.W. Schock, Electronic properties of $CuGaSe_2$-based heterojunction solar cells. Part I. Transport analysis, J. Appl. Phys. 87 (2000) 584.

75. K.P. O'Donnell, X. Chen, Temperature dependence of semiconductor band gaps, Appl. Phys. Lett. 58 (1991) 2924.

76. Qifeng Shan PhD thesis, Non-Ideal Properties of Gallium Nitride Based Light-Emitting Diodes, Rensselaer Polytechnic Institute, ProQuest Dissertations Publishing (2012).

77. V.S. Zakhvalinskii, R. Laiho, A.V. Lashkul, K.G. Lisunov, E. Lähderanta, Y.S. Nekrasova, P.A. Petrenko, V.N. Stamov, Variable-range hopping conductivity of $La_{1-x}Sr_xMn_{1-y}Fe_yO_3$, J. Phys.: Condens. Matter 23 (2011) 015802.

78. X.X. Liu, J.R. Sites, Solar-cell collection efficiency and its variation with voltage, J. Appl. Phys. 75 (1994) 577.

79. K. Muska, M. Kauk, M. Grossberg, J. Raudoja, O. Volobujeva, Influence of compositional deviations on the properties of $Cu_2ZnSnSe_4$ monograin powders, Energy Procedia 10 (2011) 323.

80. K. Muska, M. Kauk-Kuusik, M. Grossberg, M. Altosaar, M. Pilvet, T. Varema, K. Timmo, O. Volobujeva, A. Mere, Impact of $Cu_2ZnSn(Se_xS_{1-x})_4$ (x=0.3) compositional ratios on the monograin powder properties and solar cells, Thin Solid Films 535 (2013) 35.

81. R. Kniese, D. Hariskos, G. Voorwinden, U. Rau, M. Powalla, High band gap Cu(In, Ga)Se$_2$ solar cells and modules prepared with in-line co-evaporation, Thin Solid Films 431 (2003) 543.

82. P. Singh, S.N. Singh, M. Lal, M. Husain, Temperature dependence of I-V characteristics and performance parameters of silicon solar cell, Sol. Energ. Mat. Sol. Cells 92 (2008) 1611.

83. J.E. Phillips, W.N. Shafarman, E. Shan, Evidence for amorphous like behavior in small grain thin film polycrystalline solar cells, Proc. IEEE First WCPEC (24th IEEE PVSC) (1994) 303.

84. P. Würfel, Physics of Solar Cells: From Principles to New Concepts, Wiley, VCH (2005).

85. T.K. Todorov, K.B. Reuter, D.B. Mitzi, High-efficiency solar cell with earth-abundant liquid-processed absorber, Adv. Mater. 22 (2010) E156.

86. R. Klenk, H.W. Schock, Photocurrent collection in thin film solar cells – calculation and characterization for CuGaSe$_2$/(Zn,Cd)S, Proc. 12th European PVSEC (1994) 1588.

87. F. Urbach, The long-wavelength edge of photographic sensitivity and of the electronic absorption of solids, Phys. Rev. 92 (1953) 1324.

88. G.D. Cody, T. Tiedje, B. Abeles, Y. Goldstein, Disorder and the optical-absorption edge of hydrogenated amorphous silicon, Phys. Rev. Lett. 47 (1981) 1480.

89. E. Arushanov, S. Levcenko, N.N. Syrbu, A. Nateprov, V. Tezlevan, J.M. Merino, M. León, Urbach's tail in the absorption spectra of CuIn$_5$Se$_8$ and CuGa$_3$Se$_5$ single crystals, Phys. Status Solidi (a) 203 (2006) 2909.

90. I. Bonalde, E. Medina, M. Rodriguez, S.M. Wasim, G. Marin, C. Rincon, A. Rincon, C. Torres, Urbach tail, disorder, and localized modes in ternary semiconductors, Phys. Rev. B 69 (2004) 195201.

91. S.M. Wasim, I. Bonalde, E. Medina, G. Marin, C. Rincon, Defect-induced increase in the phonon energy involved in the formation of Urbach tail in Cu-ternaries, J. Phys. Chem. Solids 66 (2005) 1187.

92. A.P. Levanyuk, V.V. Osipov, Edge luminescence of direct-gap semiconductors, Sov. Phys. Usp. 24 (1981) 187.

93. J.T. Asubar, Y. Jinbo, N. Uchitomi, Impurity band conduction and negative magneto-resistance in p-ZnSnAs$_2$ thin films, Phys. Status Solidi C 6 (2009) 1158.

94. P.A. Fernandes, P.M.P. Salome, A.F. Sartori, J. Malaquias, A.F. da Cunha, B.-A. Schubert, J.C. González, G.M. Riberio, Effects of sulphurization time on Cu$_2$ZnSnS$_4$ absorbers and thin films solar cells obtained from metallic precursors, Sol. Energy Mater. Sol. Cells 115 (2013) 157.

95. N.F. Mott, Impurity band conduction. Experiment and theory. The metal-insulator transition in an impurity band, J. Phys. Colloques 37 (1976) C4.

96. S. Siebentritt, N. Papathanasiou, M.Ch. Lux-Steiner, Potential fluctuations in compensated chalcopyrites, Physica B 831 (2006) 376.

# Appendix A

**Paper I**

J. Krustok, R. Josepson, **M. Danilson**, D. Meissner. Temperature dependence of $Cu_2ZnSn(Se_xS_{1-x})_4$ monograin solar cells, Solar Energy 84 (2010) 379-383.

# Temperature dependence of $Cu_2ZnSn(Se_xS_{1-x})_4$ monograin solar cells

J. Krustok [*], R. Josepson, M. Danilson, D. Meissner

*Tallinn University of Technology, Ehitajate tee 5, 19086 Tallinn, Estonia*

## Abstract

The temperature dependence of open-circuit voltage ($V_{oc}$), short-circuit current ($I_{sc}$), fill factor ($FF$), and relative efficiency of monograin $Cu_2ZnSn(Se_xS_{1-x})_4$ solar cell was measured. The light intensity was varied from 2.2 to 100 mW/cm$^2$ and temperatures were in the range of $T = 175$–300 K. With a light intensity of 100 mW/cm$^2$ $dV_{oc}/dT$ was determined to be $-1.91$ mV/K and the dominating recombination process at temperatures close to room temperature was found to be related to the recombination in the space-charge region. The solar cell relative efficiency decreases with temperature by 0.013%/K. Our results show that the diode ideality factor $n$ does not show remarkable temperature dependence and slightly increases from $n = 1.85$ to $n = 2.05$ in the temperature range between 175 and 300 K.
© 2009 Elsevier Ltd. All rights reserved.

*Keywords:* $Cu_2ZnSn(Se_xS_{1-x})_4$; Solar cell; Temperature dependence; Monograin powder; I–V curves

## 1. Introduction

In recent years the quaternary CZTS-based semiconductors such as $Cu_2ZnSn(Se_xS_{1-x})_4$ have attracted increasing attention as possible absorber materials for solar cells. These materials have an optimal direct bandgap for solar energy conversion and a high absorption coefficient ($>10^4$ cm$^{-1}$) (Altosaar et al., 2008; Mellikov et al., 2008, 2009; Jimbo et al., 2007; Katagiri et al., 2009; Ennaoui et al., 2009). They are believed to be suitable alternatives for $CuInSe_2$ absorbers that contain expensive indium. These semiconductors can be obtained by replacing half of the indium atoms in chalcopyrite $CuInSe_2$ by zinc, and by replacing the other half by tin. While $CuInGaSe_2$- (CIG-Se-) based solar cells show efficiencies of up to 20%, record efficiencies of thin film CZTSSe cells are as yet only about 6–7% (Katagiri et al., 2009). One possible reason for this is the fact that CZTSSe thin films often contain different binary and ternary phases. Therefore it seems to be more appropriate to use higher temperatures for growth in order to better control the phase composition of the product. This is one reason why so-called monograin solar cells (Altosaar et al., 2008; Mellikov et al.,2008, 2009) look very promising. At the same time many physical properties of these compounds are still unknown and also solar cells made on their basis have not been studied in detail. Especially important for further use of these materials is the temperature dependence of the solar cell parameters since solar cell performance generally decreases with increasing temperature, fundamentally due to increased internal carrier recombination rates, caused by increased carrier excitation. Large number of correlations expressing the temperature dependence of the PV module's electrical efficiency can be retrieved, although many of them assume familiar linear form, differing only in the numerical values of the relevant parameters which are material and system dependent (Skoplaki and Palyvos, 2009; Amy and de la Breteque, 2009). Knowing these parameter is crucial for predicting the temperature dependence of CZTSSe modules also in the future. In this paper we will discuss detailed I/V-measurements of CZTSSe cells that were performed using various temperatures and light intensities.

---

[*] Corresponding author. Tel.: +372 620 3364.
E-mail address: krustok@staff.ttu.ee (J. Krustok).

## 2. Experimental

Monograin powder materials were synthesized from metal binaries (CuSe, ZnSe(S), SnSe and elemental Se) in a molten flux in an isothermal recrystallization process. The grounded precursors were thermally annealed in evacuated quartz ampoules. The crystal size of the materials was controlled by the temperature and duration of the recrystallization process and by the chemical nature of the flux. Surface morphology, phase structure and composition of the powder crystals were analyzed by high resolution SEM, XRD and EDS, respectively. The evolution of crystal shape and morphology of the monograin powders was analyzed by electron imaging using a high-resolution scanning electronmicroscope (SEM) Zeiss ULTRA55 with the compositional contrast detector EbS. The chemical composition and the distribution of components in powder crystals were determined using an energy dispersive X-ray analysis (EDX) system (Röntex). XRD patterns were recorded using a Bruker AXS D5005 diffractometer with the monochromatic Cu $K_\alpha$-radiation.

Monograin layer (MGL) solar cells were made from grains with diameters of 56–63 µm as selected by sieving. The absorber material had a composition $Cu_{1.9}Zn_{1.01}$-$Sn(Se_{0.29}S_{0.71})_{3.88}$ as determined by energy dispersive X-ray analysis (EDS). This material was used for the formation of the absorber layer in the MGL solar cell structure: graphite/CZTSSe/CdS/ZnO (Altosaar et al., 2008; Mellikov et al., 2008, 2009). Powder crystals were covered with chemically deposited CdS buffer layers. For MGL formation a monolayer of CZTSSe powder crystals was glued together by a thin layer of epoxy. The polymer film thickness was adjusted to 20 µm on top of a 10 µm glue film before inserting the monograins. Since the grains sink into the polymer and reach the underneath glue layer, after washing off the glue completely, the lower part of each grain sticks out of the polymer film. After polymerization of this epoxy, i-ZnO and conductive ZnO:Al were deposited by RF-sputtering onto the open (i.e. not covered by epoxy) surface of the layer. Solar cell structures were completed by vacuum evaporation of 1–2 µm thick in grid contacts onto the ZnO window layer. Following this, the layer was glued onto glass substrates. The opening of back contact areas of crystals that were originally inside the epoxy was done by etching of the epoxy by $H_2SO_4$ and by additional abrasive treatment. This finalized the preparation of the solar cell structure. Graphite paste was used for the back contacts.

The prepared solar cells have an area of about 0.04 cm$^2$ and their solar efficiency was measured in a Oriel class A solar simulator (19159A, Newport) to be in the range of 5%.

I–V curves were measured using an Autolab PGSTAT system. The solar cells were mounted on the cold finger of a closed-cycle He cryostat (Janis) and the temperature of the cell was changed from 300 to 170 K with $\Delta T = 5$ K. As a light source we used a standard halogen lamp with calibrated intensity. The maximum intensity was 100 mW/cm$^2$. Lower intensities were realized by using spectrally neutral net filters.

## 3. Theory

The main temperature dependence in solar cells arises from variation of three main parameters, which are usually used to characterize the solar cell outputs (Green, 1982), these are: $I_{sc}$, the short-circuit current, which usually has a negative sign; the open-circuit voltage $V_{oc}$ which in principal is characterized by $I_o$, the diode saturation current, and $n$, the diode ideality factor; and the fill factor $FF$, which in turn is a function of $V_{oc}$.

CZTSSe cells are not really ideal, and therefore it is necessary to take into account also series resistance $R_S$ and parallel conductance $G_{sh}$ of these cells. Then the solar cell equation will be given by

$$I = I_0 \left[ \exp\left( \frac{q(V - R_S I)}{nkT} \right) - 1 \right] + G_{sh}(V - R_S I) - I_L \qquad (1)$$

where $I_L$ is the photocurrent, $I_0$ is the dark saturation current and $n$ is the diode ideality factor, which can all be dependent on bias voltage and temperature. Usually, $n$ has a value between 1 and 2, but values larger than 2 are also possible. In the case where there is no recombination in the space-charge region, $n$ should have a value of 1. If on the other hand the current is dominated by recombination in the space-charge region, $n$ should be 2.

$V_{oc}$ we can obtain from Eq. (1) (taking $I = 0$):

$$V_{OC} = \frac{nkT}{q} \ln\left[ 1 - \frac{G_{sh}V_{oc}}{I_0} + \frac{I_L}{I_0} \right] \qquad (2)$$

According to theory, $I_0$ is a function of material properties and it is also sensitive to temperature. In general (Green, 1982; Rau and Schock, 1999)

$$I_0 = I_{00} \exp\left[ -\frac{E_A}{nkT} \right] \approx A T^3 \exp\left[ -\frac{E_A}{nkT} \right], \qquad (3)$$

where the activation energy $E_A$ and also $I_{00}$ depend mainly on the dominating recombination mechanism in the solar cell. In case of bulk recombination $E_A \approx E_g$ where $E_g$ is the bandgap energy of the absorber material.

According to (2) we expect a linear dependence of $V_{oc}$ on temperature, if $I_L \gg G_{sh}V_{oc}$ and $I_L \gg I_0$. Then from (2) and (3) we have

$$V_{oc} = \frac{E_A}{q} - \frac{nkT}{q} \ln\left[ \frac{I_{00}}{I_L} \right] \qquad (4)$$

At the same time we must take into account that the ideality factor $n$ and also $I_{00}$ have a small but certain temperature dependence (Rau and Schock, 1999).

The photocurrent $I_L$ of a solar cell generally increases slightly with increasing temperature, due to a decreasing bandgap energy. This decrease in the bandgap allows photons with longer wavelengths, lower energy, to be absorbed by the solar cell. As a result, the short-circuit current of the

cell increases. In good solar cells $-I_L \approx I_{sc}$. In general, from Eq. (1) we find for $I_{sc}$

$$I_{sc} = I_0 \left[ \exp \left( -\frac{qR_S I_{sc}}{nkT} \right) - 1 \right] - R_S I_{sc} G_{sh} - I_L \qquad (5)$$

It is practically impossible to calculate the T-dependence of $I_{sc}$, but in many cases we can assume a simple linear dependence. Again, if the series resistance of the cell becomes larger, then $|I_{sc}| < |I_L|$ and we will have a more complex dependence. The same is valid if the intensity (and therefore also $|I_{sc}|$) becomes larger and the exponential term in Eq. (5) starts to play a role.

In many cases it is possible to avoid complications from series resistance effects by using $I_{sc}$ vs. $V_{oc}$ curves measured for different light intensities and temperatures. Taking $I = 0$ Eq. (1) becomes

$$I_L = I_0 \left[ \exp \left( \frac{qV_{oc}}{nkT} \right) - 1 \right] + G_{sh} V_{oc} \qquad (6)$$

If the shunting current is small and $I_L = -I_{sc}$ then we will have a simple exponential function. Using Eq. (6) we are able to extract $I_0$ and the ideality factor $n$.

Fill factors FF depend on a range of cell parameters, including current and voltage operating levels, cell ideality factors and parasitic series and shunt resistances. As such, it is difficult to derive generic formulae for the temperature sensitivity of this parameter. At the same time the temperature dependence of the fill factor often determines the shape of the temperature dependence curve of the power outcome of the solar cell, because both $I_{sc}$ and $V_{oc}$ usually show nearly linear behavior on temperature. In good solar cells and at higher temperatures FF usually decreases with temperature (Würfel, 2005). At lower temperatures, when $R_{se}$ increases, FF usually shows an opposite dependence. Therefore we may expect a maximum value of FF somewhere below room temperatures.

## 4. Results and discussion

In Fig. 1, I–V curves measured at different temperatures under 100 mW/cm² illumination are presented. It can be seen that increasing the temperature leads to a decrease of $V_{oc}$ and an increase of $I_{sc}$.

The thermal behavior of the $V_{oc}$ under different light intensities is shown in Fig. 2. As shown here, with an illumination intensity of 100 mW/cm² the open-circuit voltage $V_{oc}$ increases with decreasing temperature by 1.91 mV/K. The linear behavior for all light intensities indicates that, according to Eq. (4), the temperature dependence of the ideality factor $n$ and of $I_{00}$ have only a minor effect on the temperature dependence of $V_{oc}$. According to theory, all $V_{oc}(T)$ curves measured for different intensities must show different slopes but the same $E_A$ at 0 K. The extrapolation to 0 K results in $E_A \approx 1.2$ eV for all intensities. This is consistent with the spectral response (Altosaar et al., 2008) and photoluminescence (Grossberg et al., 2009) measurements and shows that $E_A \approx E_g$ in this material. This in
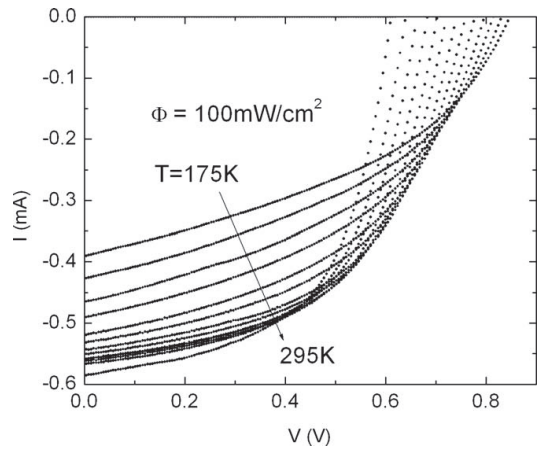


Fig. 1. Temperature dependence of I–V curves of CZTSSe monograin solar cells obtained in a light intensity of 100 mW/cm².
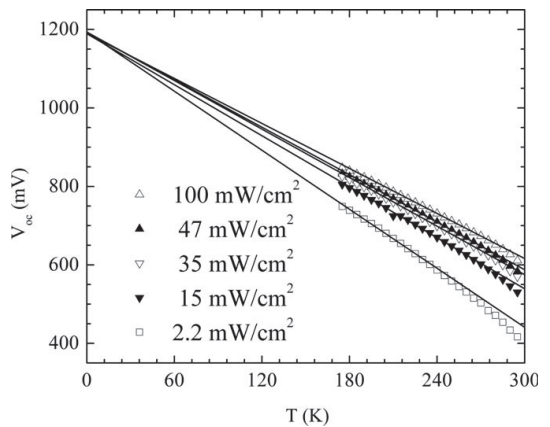


Fig. 2. Open circuit voltage $V_{oc}$ of the CZTSSe monograin cell as a function of temperature illuminated with different light intensities. The straight lines are linear fits of Eq. (4).

turn is direct evidence that in these CZTSSe monograin solar cells the dominating recombination (at least at temperatures close to room temperature) is a recombination in the space-charge region. All measured $V_{oc}(T)$ curves were fitted with linear functions and the corresponding fitting parameters are given in Table 1.

Table 1
Parameters obtained from fitting temperature dependent I/V-curves.

| $\Phi$ (mW/cm²) | $-\frac{dV_{oc}}{dT}$ (mV/K) | $E_A$ (meV) | $\frac{d\eta}{dT}$ (%/K) |
|---|---|---|---|
| 100 | 1.91 | 1190 | −0.013 |
| 47 | 2.02 | 1193 | −0.016 |
| 35 | 2.06 | 1193 | −0.020 |
| 15 | 2.17 | 1189 | −0.022 |
| 2.2 | 2.51 | 1193 | −0.025 |

We also observed linear increase of $I_{sc}$ with temperature in the range 200–300 K. For 100 mW/cm$^2$ we found $dI_{sc}/dT = 6 \times 10^{-4}$ mA/K. At lower intensities this slope is even smaller.

According to Eq. (6), a semilogarithmic plot of $I_{sc}$ versus $V_{oc}$ will yield a straight line for high-enough $V_{oc}$. From this slope $n$ can be calculated if one knows the temperature. $I_0$ can be found by taking the intercept of the straight part of the plot with the $I_{sc}$-axis. In Fig. 3 $I_{sc}$ ($V_{oc}$) curves for different temperatures were plotted. It can be seen that all curves show a simple exponential behavior. All experimental curves were fitted using the exponential part of Eq. (6). Fitting results shows that the diode ideality factor $n$ does not exhibits a remarkable temperature dependence and only slightly increases from $n = 1.85$ to $n = 2.05$ in the temperature range $T = 175$–300 K. This is a quite surprising result because in most solar cells the ideality factor decreases with temperature (Rau and Schock, 1999; Würfel, 2005). One reason for this different trend in our cells can be the temperature dependent bulk recombination current which increases at higher temperatures. Therefore we observe an ideality factor very close to $n = 2$.

From Fig. 3 we also extracted $I_0$ values and the temperature dependence of $I_0$ is shown in Fig. 4. We fitted these calculated points with Eq. (3), by using an average value on $n$ ($n = 1.87$). Although this fitting is not very accurate we still got $E_A = 1.24$ eV and this value is very close to the $E_A$ value we found using $V_{oc}$ ($T$) curves. This coincidence supports assumptions we made regarding the role of $G_{sh}$ and $R_{se}$ and the use of a simplified theoretical model where we did not directly take into account the decrease of the bandgap energy with temperature.

Especially important is the temperature dependence of the relative efficiency $\eta$ of solar cells. Therefore we plotted also $\eta$ ($T$) curves measured at different light intensities, see
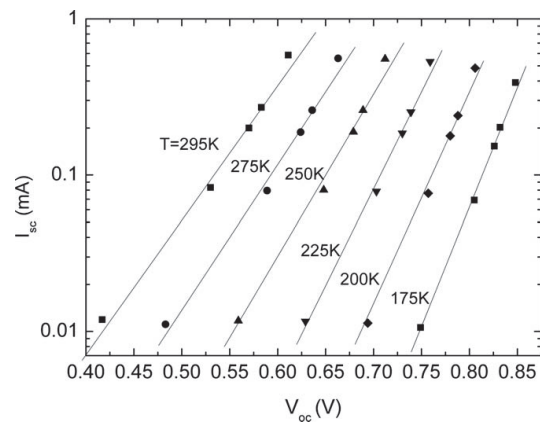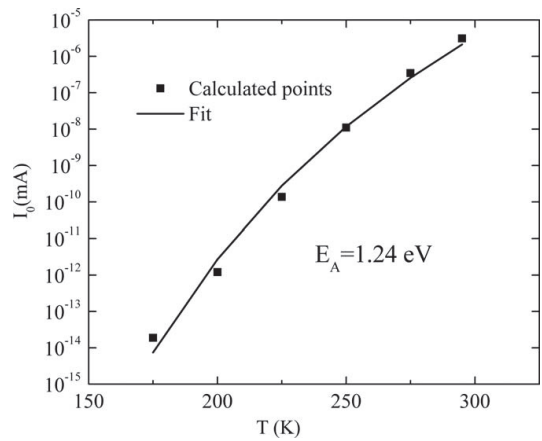


Fig. 4. $I_0/T$-graph. Experimental points were fitted using Eq. (3).
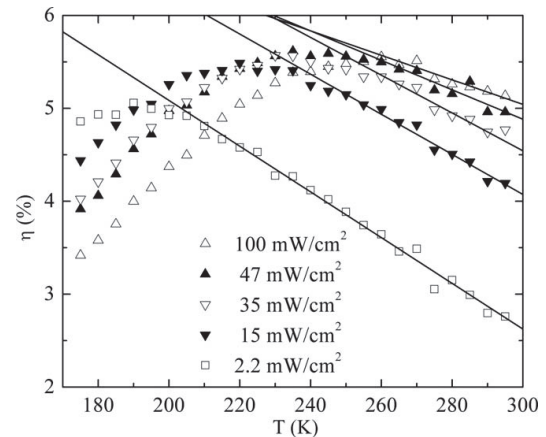


Fig. 5. Temperature dependence of the relative efficiency $\eta$ of a CZTSSe monograin solar cell illuminated with different light intensities. Linear fitting was used for the high temperature region and fitting results are presented as lines.

Fig. 5. Calculated efficiencies are not calibrated, because we used a simple halogen light source and therefore AM1.5 spectral conditions were not followed. It can be seen that the efficiencies have a maximum value below room temperature. The corresponding maximum efficiency temperature increases with light intensity and at 100 mW/cm$^2$ it is at about 250 K. At low temperatures the efficiency starts to decrease with decreasing temperature. The same decrease can be observed also with increasing the temperature above 250 K. At this "high" temperature region the decrease of the efficiency is nearly linear with temperature. Corresponding slopes are also given in Table 1. This curved $\eta$ ($T$) dependence is caused by the temperature dependence of the fill factor $FF$.



Fig. 3. $I_{sc}/V_{oc}$-curves for temperatures in the range of 175–295 K. Every measurement was done with five different illumination intensities ranging from 2.2 to 100 mW/cm$^2$. Lines represent the least square fit showing good correlation with Eq. (6).

Measured temperature coefficients of CZTSSe mono-grain solar cells indicate that in many cases they are lower than for other type of solar cells. For example Cu(In,-Ga)Se$_2$ cells usually show $dV_{oc}/dT$ values from $-2.01$ to $-3.3$ mV/K and $d\eta/dT$ values from $-0.017$ to $-0.064\%$/K (Kniese et al., 2003). Si cells show $dV_{oc}/dT$ values from $-2.07$ to $-2.17$ mV/K and $d\eta/dT$ value about $-0.042\%$/K (Singh, 2008). The same is the situation in CdTe cells, where $dV_{oc}/dT$ is typically in the range of $-2.1$ to $-2.2$ mV/K (Phillips et al., 1994). These low values of measured temperature coefficients of CZTSSe solar cells show a great potential of this compound.

## 5. Conclusions

In summary, from I–V measurements we have calculated the monograin Cu$_2$ZnSn(Se$_x$S$_{1-x}$)$_4$ solar cell parameters as a function of temperature. For a light intensity of 100 mW/cm$^2$ the $dV_{oc}/dT = -1.91$ mV/K and $E_A$ was close to the bandgap energy of 1.2 eV. The dominating recombination is related to recombination in the space-charge region. The solar cell relative efficiency decreases with temperature with a slope of 0.013%/K. The diode ideality factor $n$ was close to a value of 2 and showed very small increase with temperature.

## Acknowledgements

## References

Altosaar, M., Raudoja, J., Timmo, K., Danilson, M., Grossberg, M., Krustok, J., Mellikov, E., 2008. Cu$_2$ Zn$_{1-x}$ Cd$_x$ Sn(Se$_{1-y}$ S$_y$)$_4$ solid solutions as absorber materials for solar cells. Physica Status Solidi A 205, 167–170.

Amy de la Breteque, E., 2009. Thermal aspects of c-Si photovoltaic module energy rating. Solar Energy 83, 1425–1433.

Ennaoui, A., Lux-Steiner, M., Weber, A., Abou-Ras, D., Kötschau, I., Schock, H.-W., Schurr, R., Hölzing, A., Jost, S., Hock, R., Voß, T., Schulze, J., Kirbs, A., 2009. Cu$_2$ZnSnS$_4$ thin film solar cells from electroplated precursors: novel low-cost perspective. Thin Solid Films 517, 2511–2514.

Green, M.A., 1982. Solar Cells. Prentice-Hall, Inc., Englewood Cliffs.

Grossberg, M., Krustok, J., Timmo, K., Altosaar, M., 2009. Radiative recombination in Cu$_2$ZnSnSe$_4$ monograins studied by photoluminescence spectroscopy. Thin Solid Films 517, 2489–2492.

Jimbo, K., Kimura, R., Kamimura, T., Yamada, S., Maw, W.S., Araki, H., Oishi, K., Katagiri, H., 2007. Cu$_2$ZnSnS$_4$-type thin film solar cells using abundant materials. Thin Solid Films 515, 5997–5999.

Katagiri, H., Jimbo, K., Maw, W.S., Oishi, K., Yamazaki, M., Araki, H., Takeuchi, A., 2009. Development of CZTS-based thin film solar cells. Thin Solid Films 517, 2455–2460.

Kniese, R., Hariskos, D., Voorwinden, G., Rau, U., Powalla, M., 2003. High band gap Cu(In, Ga)Se2 solar cells and modules prepared with in-line co-evaporation. Thin Solid Films 431–432, 543–547.

Mellikov, E., Altosaar, M., Krunks, M., Krustok, J., Varema, T., Volobujeva, O., Grossberg, M., Kaupmees, L., Dedova, T., Timmo, K., Ernits, K., Kois, J., Acik, Oja, Danilson, M., Bereznev, S., 2008. Research in solar cell technologies at Tallinn University of Technology. Thin Solid Films 516, 7125–7134.

Mellikov, E., Meissner, D., Varema, T., Altosaar, M., Kauk, M., Volubujeva, O., Raudoja, J., Timmo, K., Danilson, M., 2009. Monograin materials for solar cells. Solar Energy Materials & Solar Cells 93, 65–68.

J.E. Phillips, W.N. Shafarman, E. Shan, Evidence for amorphous like behavior in small grain thin film polycrystalline solar cells, in: Proc. IEEE First WCPEC (24th IEEE PVSC), 1994, pp. 303–306.

Rau, U., Schock, H.W., 1999. Electronic properties of Cu(In, Ga)Se2 heterojunction solar cells–recent achievements, current understanding, and future challenges. Applied Physics A 69, 131–147.

Singh, P., Singh, S.N., Lal, M., Husain, M., 2008. Temperature dependence of I–V characteristics and performance parameters of silicon solar cell. Solar Energy Materials & Solar Cells 92, 1611–1616.

Skoplaki, E., Palyvos, J.A., 2009. On the temperature dependence of photovoltaic module electrical performance: a review of efficiency/power correlations. Solar Energy 83, 614–624.

Würfel, P., 2005. Physics of Solar Cells: From Principles to New Concepts. Wiley, VCH.

# Appendix A

## Paper II

J. Krustok, R. Josepson, T. Raadik, **M. Danilson**. Potential fluctuations in $Cu_2ZnSnSe_4$ solar cells studied by temperature dependence of quantum efficiency curves, Physica B 405 (2010) 3186-3189.

# Potential fluctuations in $Cu_2ZnSnSe_4$ solar cells studied by temperature dependence of quantum efficiency curves

J. Krustok *, R. Josepson, T. Raadik, M. Danilson

Tallinn University of Technology, Ehitajate tee 5, 19086 Tallinn, Estonia

## ARTICLE INFO

## ABSTRACT

A new method to study spatial potential fluctuations in compensated absorber materials used in solar cells is introduced. The method is based on the analysis of the temperature dependence of quantum efficiency curves in solar cells. As an example $Cu_2ZnSnSe_4$ monograin solar cell is studied at temperatures $T = 10$–$300$ K. It is shown that this absorber material has spatial potential fluctuations with an average energetic depth of 25 meV. The room temperature bandgap energy of $Cu_2ZnSnSe_4$ is found to be $E_g = 1.017$ eV.

© 2010 Elsevier B.V. All rights reserved.

## 1. Introduction

$Cu_2ZnSnSe_4$ (CZTSe) is a p-type semiconductor which could replace $CuInSe_2$ absorber in the future solar cells. In this compound expensive and resource-limited In is substituted by Zn and Sn. Recently a conversation efficiency as high as 9.3% was reported in CZTSe solar cells [1]. Latest studies have shown that the bandgap energy of this compound at room temperature is about 1 eV [2,3]. This is also confirmed by theoretical calculations [4]. An ideal thin-film solar cell absorber material should have a direct bandgap of around 1.3–1.4 eV and therefore one needs to adjust the bandgap energy. One possible way to do so is to use solid solutions with an overall stoichiometry of $Cu_2ZnSn(Se_xS_{1-x})_4$. Unfortunately, the fundamental physical properties of these solid solutions are not well understood. The same is true for CZTSe. Photoluminescence (PL) and Raman studies of this Cu-poor compound [2] showed rather high concentrations of charged point defects. A high defect concentration is typical also for Cu-poor $CuInSe_2$ and other compensated ternary compounds and usually leads to the formation of spatial potential fluctuations [5,6]. As a result, the density of states function for valence and conduction bands has an exponential tail. Potential fluctuations usually form potential wells for holes and thus localized states can be formed. These states can be detected by PL emission, which involves recombination of free electrons with holes localized in these tail states. Usually this emission shows asymmetrical PL bands and from the shape of these PL bands the average depth of potential fluctuations $\gamma$ can be found [5]. Typically in chalcopyrite ternaries $\gamma$ has a value below 30 meV [5–7]. Our recent PL studies show that in CZTSe $\gamma \approx 24$ meV [8]. The hole concentration in this absorber was always lower than $10^{16}$ cm$^{-3}$, as was detected by $C$–$V$ measurements. In the present paper we propose a new method to study spatial potential fluctuations in CZTSe. It is based on the analysis of temperature dependent quantum efficiency measurements of solar cells.

## 2. Experimental

In this study we used monograin solar cells, where the CZTSe absorber in the form of monograins was prepared from CuSe, ZnSe, and SnSe precursors in molten KI. The binary compounds in stoichiometric relation of CZTSe were mixed with KI and ground in a planetary ball mill. The mixture was degassed and sealed into quartz ampoules. The recrystallization temperature was 1000 K. The crystal size was controlled by the temperature and the duration of the recrystallization process. Crystals have a typical diameter of 50 μm. The chemical composition Cu/(Zn+Sn)=0.87; Zn/Sn=0.97 of the monograin powder was determined by the energy dispersive X-ray spectroscopy (EDS). In the record cells composition Cu/(Zn+Sn)=0.8; Zn/Sn=1.22 was reported [1]. In our experiment crystals were Cu-poor and slightly Sn-rich while in record cells [1] Zn-rich composition was used. The CZTSe phase was confirmed by the X-ray diffraction (XRD) measurements. All

* Corresponding author. Tel.: +372 620 3364; fax: +372 620 3367.
  E-mail address: krustok@staff.ttu.ee (J. Krustok).

powder crystals were covered with CdS thin layer by chemical bath deposition. For monograin layer (MGL) formation a mono-layer of sieved, nearly unisize grains was bound into a thin layer of epoxy resin, so that the contamination of the upper surfaces of the crystals with epoxy was avoided. After the polymerization of epoxy, a ZnO window layer was deposited onto the front side of the MGL by RF-sputtering. Solar cell structures were completed by vacuum evaporation of a 1–2 μm thick In grid contact onto the ZnO window layer. After glueing the structures on glass substrates, the back contact area of crystals covered with epoxy was opened by etching the epoxy with $H_2SO_4$ followed by an additional abrasive treatment. The back contact was made using graphite paste. More details about the solar cell preparation can be found in [3].

I–V curves of these solar cells were measured using a Keithley 2400 source meter with the Oriel class A solar simulator 91159A. The typical area of the cells was 3–4 mm². For the temperature dependent quantum efficiency measurements solar cells were mounted in a closed cycle He-cryostat (Janis) where the temperature of the cell can be controlled in the range of $T=10$–300 K. A 100 W calibrated halogen lamp was used as a light source together with the a SPM-2 prism monochromator. Monochromatic and modulated (120 Hz) light was focused on the front surface of the solar cell. The generated short circuit current was detected with a DSP Lock-In (SR 810).

## 3. Results and discussion

A typical I–V curve of a CZTSe cell is given in Fig. 1.

It can be seen that this CZTSe cell has quite low solar cell parameters. Especially low is the open circuit voltage $V_{oc}$. In this cell we assume to have quite big recombination losses. However, we see that even this "bad" cell generates current and therefore it is possible to use it to study the temperature dependence of its quantum efficiency.

The low-energy side of the quantum efficiency spectrum near the bandgap energy $E_g$ of the absorber can be fitted by the equation of Klenk and Schock [9]:

$$QE = K(1-\exp(-\alpha L_{eff})) \tag{1}$$

where $L_{eff}=w+L_d$ is the effective diffusion length of minority carriers, $L_d$ is their diffusion length in the absorber material, $w$ is the width of the depletion region, and $\alpha$ is the absorption coefficient of the absorber material. The constant $K$ is unity in absolute measurements. It is obvious that in the case of a
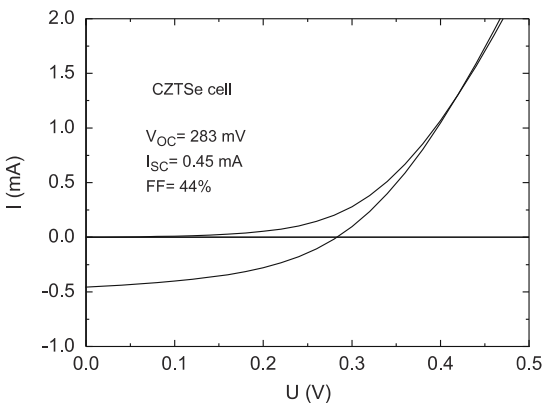
compensated absorber material also the effective diffusion length of majority carriers must be taken into account. Therefore in compensated CZTSe we expect to see a more pronounced role of the hole mobility on the temperature dependence of QE curves.

The fundamental absorption edge in most semiconductors follows an exponential law and for energies $E < E_g$ the absorption coefficient usually can be described by the so-called Urbach rule [10,11]:

$$\alpha(E) = \alpha_0 \exp\left[\frac{\sigma}{kT}(E-E_0)\right] \tag{2}$$

where $\sigma$ is a steepness parameter, and $E_0$ and $\alpha_0$ are characteristic parameters of the material.

Assuming that in this region QE is mostly determined by the absorption coefficient, i.e.

$$QE^*E(E) \propto \alpha(E) \tag{3}$$

the $QE^*E$ curves must also have an exponential part where we are able to find $\sigma$, $E_0$, and $\alpha_0$. Indeed, Fig. 2 shows the exponential part of the $QE^*E$ curves at different temperatures.

All these $QE^*E$ curves were fitted using Eq. (2). From these fits we found $E_0$ and the temperature dependence of the steepness parameter $\sigma$ as shown in Fig. 3. It should be mentioned that at low temperatures, where $T<60$ K we have slightly lower $E_0$ values. One reason for this could be a too low mobility of carriers on the QE curve at very low temperatures. Therefore the assumed relation (3) is not valid any more in this temperature region.

The data from Fig. 3 are fitted to the following empirical relation [10,11]:

$$\sigma = \sigma_0(2kT/\hbar\omega_P)\tan h(\hbar\omega_P/2kT) \tag{4}$$

where $\sigma_0$ is a constant and $\hbar\omega_P$ the energy of the phonons associated with Urbach's tail. According to fitting results we got $\hbar\omega_P=85$ meV (686 cm$^{-1}$) and $\sigma_0=1.46$. Our latest Raman measurements showed that the highest phonon energy in CZTSe is about 250 cm$^{-1}$ [2]. It was shown [12–14] that in the case of a structural and electronic disorder the corresponding phonon energy found from Urbach's tail always seems to be much higher than the energy of measured phonon modes. For example, in CuInSe$_2$ phonon energies as high as 60 meV were found from Urbach's tail measurements while the highest optical mode energy obtained from Raman measurements was only 29 meV [14]. Similarly, in our CZTSe crystals with their quite high defect concentrations, the high value of the observed phonon energy

Fig. 1. Dark and light *I–V* curves of CZTSe cell measured at room temperature.
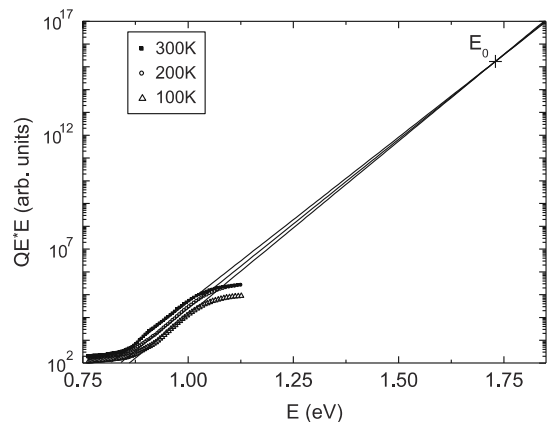
Fig. 2. Typical *QE*E* curves obtained at different temperatures showing the exponential Urbach behaviour with $E_0$ at 1.73 eV. Solid lines are the fitting results with Eq. (2).
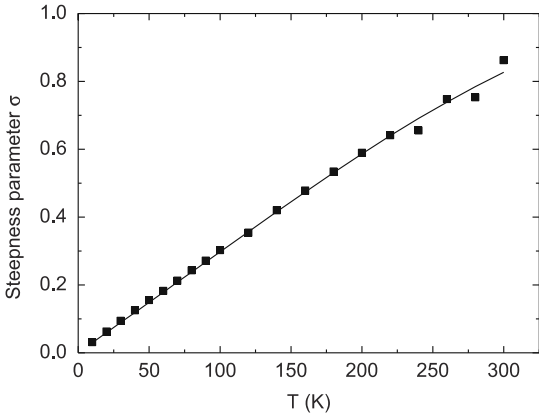
Fig. 3. Temperature dependence of steepness parameter $\sigma$. Solid line represents the fit using Eq. (4).



Fig. 4. Normalised QE curves vs. photon energy measured at different temperatures. Solid lines are fits using Eq. (5).



Fig. 5. The temperature dependence of the effective bandgap energy $E_g^*$.

seems to be realistic. The most important result of this kind of analysis is that we really can use QE curves to obtain information about the behaviour of the absorption coefficient.

Above the exponential tail, the absorption coefficient of direct band semiconductor has been observed to obey the equation: $\alpha(E) = B(E-E_g)^{1/2}$. If the absorption coefficient is small, i.e. near the bandgap energy $E \approx E_g$, then Eq. (1) can be simplified as

$$QE \approx K\alpha L_{eff} \approx A(E-E_g^*)^{1/2}/E \qquad (5)$$

where $E_g^*$ is an effective bandgap energy and constant $A$ includes all parameters that do not depend on $E$. Therefore $(E^*QE)^2$ vs. $E$ curves should have a linear segment from which one can find a value for $E_g^*$. In case of spatial potential fluctuations the effective bandgap energy is lower than the bandgap energy of the "ideal" semiconductor without potential fluctuations, because the shape of the $\alpha(E)$ curve does not completely follow the $E^{1/2}$ rule, see for example [15]. Especially at low temperatures, when electrons and holes can occupy localized states inside the potential wells, the difference between $E_g$ and $E_g^*$ can be quite big. At the same time when potential fluctuations are very small we often will find $E_g \approx E_g^*$ [15].

Typical QE curves measured at different temperatures are given in Fig. 4. All curves have an $E^{1/2}$ behaviour in the energy range of about $E=1.02$–$1.12$ eV. From these curves $E_g^*$ was found for every temperature used, see Fig. 5.

It can be seen from Fig. 5 that at low temperatures $E_g^*$ is almost constant but drops at $T=60$ K. At $T > 60$ K the effective bandgap energy increases with temperature until at $T \approx 250$ K it starts to decrease again. The overall increase of the $E_g^*$ at $T=60$–$250$ K is about 23 meV.

This kind of dependence can be explained if we take deep potential fluctuations into account in our sample. It is obvious that QE depends not only on the absorption coefficient but also on the ability of generated charge carriers to reach the front and back contacts. Especially at low temperatures the heavier holes tend to localize inside the potential wells. Although at low temperatures we probably have an absorption at $E < E_g$, here the QE curves do not show any remarkable current. The reason could be that this spectral region belongs to the deepest potential wells and the generated holes cannot move and hence the QE remains small. Therefore we start to measure a current only at higher photon energy, where the potential wells are not so deep and photo-generated holes can move. At higher temperatures also the current generated from the deepest wells increases. They can now
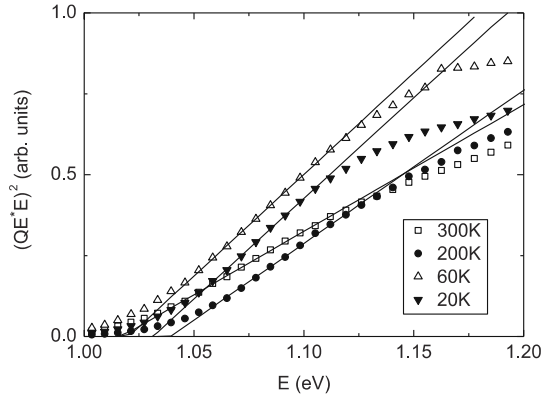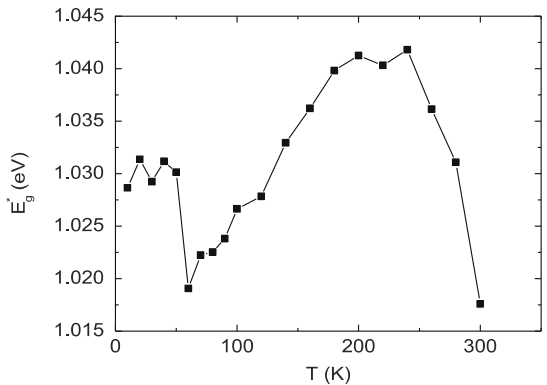
move and thus we see a small decrease of the effective bandgap energy at $T=60$ K. Because the concentration of these deep wells is small and only a fraction of all charges are liberated we should see here also a decrease in the integrated QE at the same temperature. The temperature dependence of the integrated quantum efficiency $\Phi$ is given in Fig. 6. In the range of $T=60$–$250$ K we see an increase of $\Phi$ with temperature. It is obvious that this increase is related to thermally activated liberation of charges from the potential wells. If we assume that the average depth of these energy wells is $\gamma$, then there must be a temperature region, where

$$\Phi = \Phi_0 \exp(\gamma/kT) \qquad (6)$$

Indeed, from the inset of Fig. 6 we see that the fit to Eq. (6) gives $\gamma=25 \pm 1$ meV. This energetic depth correlates with the shift of $E_g^*$ with temperature in the same region, if we also take the decrease of the bandgap energy with temperature into account. Therefore the observed shift of $E_g^*$ is slightly smaller than $\gamma$.

The value of $\gamma$ found from QE curves is actually very close to the corresponding value obtained from photoluminescence measurements, for which $\gamma=24$ meV was determined for our CZTSe crystals [8].

At higher temperatures all charges possess enough activation energy to be free and therefore $E_g^* \approx E_g$. From Fig. 5 we can find the bandgap energy for CZTSe at room temperature to be $E_g=1.017$ eV.
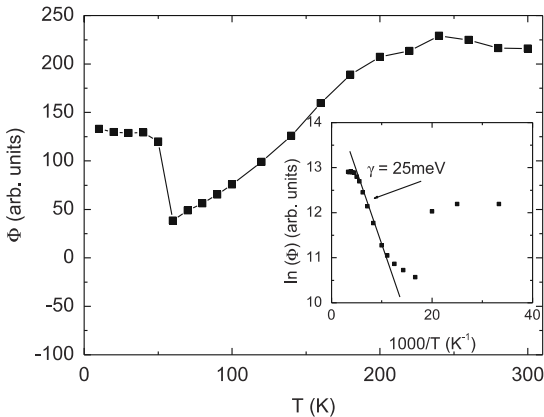
**Fig. 6.** Temperature dependence of the integrated quantum efficiency $\Phi$. The inset shows an exponential part fitted with Eq. (6).

Our previous PL studies [2] showed that the low temperature bandgap energy of CZTSe must be in the range of 1.02 eV. The bandgap energy obtained from $QE$ curves confirms this value. It is obvious that if the concentration of majority carriers (holes) is high, then $QE$ is mainly determined by the effective diffusion of minority carriers (electrons). At the same time electrons generally have a smaller effective mass and therefore they usually do not have localized states inside the potential wells. Therefore in this case the temperature dependence of $QE$ curves should not show such a pronounced shift of the effective bandgap energy with temperature. Thus this kind of analysis is more suitable for compensated absorber materials and can be used to study spatial potential and probably also compositional fluctuations in these materials.

## 4. Conclusions

Quantum efficiencies of photocurrent generation in $Cu_2ZnSnSe_4$ monograin solar cell were measured between 10 and 300 K. It was shown that these curves can be used to determine effective bandgap energies of the absorber. The temperature dependence of the effective bandgap energies and of the integrated quantum efficiency dependencies allows to calculate the average depth of potential wells for charge carriers. The such determined value of 25 meV agrees very well with the value determined in photoluminescence measurements. It was shown that the room temperature bandgap energy in $Cu_2ZnSnSe_4$ is $E_g = 1.017$ eV.

## References

[1] T.K. Todorov, K.B. Reuter, D.B. Mitzi, Adv. Mater. 22 (2010) Published Online: 8 February 2010.
[2] M. Grossberg, J. Krustok, K. Timmo, M. Altosaar, Thin Solid Films 517 (2009) 2489.
[3] M. Altosaar, J. Raudoja, K. Timmo, M. Danilson, M. Grossberg, J. Krustok E. Mellikov, Phys. Status Solidi (a) 205 (2008) 167.
[4] ShiYou Chen, X.G. Gong, A. Walsh, S.H. Wei, Appl. Phys. Lett. 94 (2009) 041903.
[5] J. Krustok, H. Collan, M. Yakushev, K. Hjelt, Phys. Scripta T79 (1999) 179.
[6] J. Krustok, J. Raudoja, M. Yakushev, R.D. Pilkington, H. Collan, Phys. Status Solidi (a) 173 (1999) 483.
[7] M. Grossberg, J. Krustok, A. Jagomägi, M. Leon, E. Arushanov, A. Nateprov I. Bodnar, Thin Solid Films 515 (2007) 6204.
[8] M. Grossberg, J. Krustok, J. Raudoja, K..Timmo, M. Altosaar, T. Raadik, Photoluminescence and Raman study of $Cu_2ZnSn(Se_xS_{1-x})_4$ monograins for photovoltaic applications (to be published).
[9] R. Klenk and H.W. Schock, Photocurrent collection in thin film solar cells—calculation and characterization for $CuGaSe_2/(Zn,Cd)S$, in: Proceedings of the 12th Euoropean Photovoltaic Solar Energy Conference, 1994, pp.1588–1591.
[10] F. Urbach, Phys. Rev. 92 (1953) 1324.
[11] G.D. Cody, T. Tiedje, B. Abeles, Y. Goldstein, Phys. Rev. Lett. 47 (1981) 1480.
[12] E. Arushanov, S. Levcenko, N.N. Syrbu, A. Nateprov, V. Tezlevan, J.M. Merino, M. León, Phys. Status Solidi (a) 203 (2006) 2909.
[13] I. Bonalde, E. Medina, M. Rodriguez, S.M. Wasim, G. Marin, C. Rincon A. Rincon, C. Torres, Phys. Rev. B 69 (2004) 195201.
[14] S.M. Wasim, I. Bonalde, E. Medina, G. Marin, C. Rincon, J. Phys. Chem. Solids 66 (2005) 1187.
[15] A.P. Levanyuk, V.V. Osipov, Sov. Phys. Usp. 24 (1981) 187.

# Appendix A

## Paper III

**M. Danilson**, E. Kask, N. Pokharel, M. Grossberg, M. Kauk-Kuusik, T. Varema, J. Krustok. Temperature dependent current transport properties in $Cu_2ZnSnS_4$ solar cells, Thin Solid Films 582 (2015) 162-165.

CrossMark

# Temperature dependent current transport properties in Cu$_2$ZnSnS$_4$ solar cells

Mati Danilson [a,*], Erkki Kask [b], Nikhil Pokharel [a,c], Maarja Grossberg [a], Marit Kauk-Kuusik [a], Tiit Varema [a], Jüri Krustok [a,b]

[a] Department of Materials Science, Tallinn University of Technology, Ehitajate tee 5, 19086 Tallinn, Estonia
[b] Department of Physics, Tallinn University of Technology, Ehitajate tee 5, 19086 Tallinn, Estonia
[c] Department of Natural Sciences (Physics), Kathmandu University, PO Box 6250 Dhulikhel, Nepal

## ARTICLE INFO

## ABSTRACT

Quaternary semiconductor compound Cu$_2$ZnSnS$_4$ (CZTS) is a promising non-toxic absorber material for solar cells made from earth abundant elements. In this study temperature dependencies ($T = 10$–300 K) of current–voltage (J–V) characteristics and external quantum efficiency (EQE) spectra of CZTS monograin layer solar cells were measured in order to clarify current transport in CZTS that is still not fully understood. Three different temperature ranges can be distinguished from the temperature dependence of the series resistance ($R_s$) obtained from J–V measurements and the effective bandgap energy ($E_g^*$) determined from the EQE spectra. Thermally activated conductivity, Mott's variable-range hopping conductivity, and very low temperature (<40 K) blocking of the interface recombination were observed.

© 2014 Elsevier B.V. All rights reserved.

## 1. Introduction

Multinary semiconductor compounds Cu$_2$ZnSn(Se$_x$S$_{1-x}$)$_4$ (CZTSSe) are promising non-toxic absorber materials for solar cells made from earth abundant elements. Currently, the power conversion efficiency record of Cu$_2$ZnSnS$_4$ (CZTS) device is 8.4% [1] and that of CZTSSe device −12.6% [2]. High series resistance and interface recombination are reported as the main limiting factors in CZTS-based solar cells [3,4]. Hence, almost all basic solar cell parameters are limited by recombination and parasitic losses. Moreover, most of CZTS absorbers used in solar cells show properties of so-called heavily doped semiconductors, where high concentration of charged defects leads to a formation of spatial potential fluctuations [5]. Accordingly, different type of current transport and recombination mechanisms can be observed [6–9].

In CZTS solar cells recombination losses are not only related to the interface between absorber and buffer layers but also to the bulk defects or band tails. The first-principle calculations have been made for CZTS by Chen et al. [10]. They found that the main acceptor defect in CZTS is Cu$_{Zn}$ antisite defect that has a quite deep level at $E_A = 0.12$ eV.

This acceptor was also found by admittance spectroscopy [11]. Even deeper acceptor ($E_A = 0.28$ eV) was detected in CZTS by photoluminescence spectroscopy [12]. These quite deep defects can be efficient recombination centers even at temperatures close to room temperature. At the same time, Chen et al. [13] have shown that the compensation between the dominant acceptor defect Cu$_{Zn}$ and the donor defect Sn$_{Zn}$ can significantly decrease the formation energies of the defect clusters (Cu$_{Zn}$ + Sn$_{Zn}$ and 2Cu$_{Zn}$ + Sn$_{Zn}$) leading to high concentrations of these clusters even in stoichiometric samples. It was shown that the recombination through these defect clusters dominates in most CZTS samples at low temperatures [14]. The presence of different defect complexes in CZTS was also proposed by Huang et al. [15]. According to their calculations these complexes can cause a significant local band gap decrease and boost the recombination.

The temperature-dependent conductivity of polycrystalline CZTS thin films [3,4,6–9] and single crystals [16] has been studied in many papers. However, in real solar cell structures many different recombination channels appear which are not present in bulk CZTS. Therefore, it is extremely interesting to study temperature dependence of these real structures. We already have studied the temperature dependencies of Cu$_2$ZnSnSe$_4$ monograin layer (MGL) solar cells and showed how potential fluctuations change the current transport in these structures [17]. In this study, current–voltage (J–V) characteristics and external quantum efficiency (EQE) curves were used for characterizing recombination and parasitic effects in order to identify loss mechanisms and reveal current transport properties in CZTS-based MGL solar cells.

---

* Corresponding author at: Ehitajate tee 5, 19086 Tallinn, Estonia. Tel.: +372 6203210; fax: +372 6203367.
E-mail addresses: mati.danilson@ttu.ee (M. Danilson), erkki.kask@ttu.ee (E. Kask), pokharel.nikhil@gmail.com (N. Pokharel), Maarja.Grossberg@ttu.ee (M. Grossberg), marit.kauk-kuusik@ttu.ee (M. Kauk-Kuusik), Tiit.Varema@ttu.ee (T. Varema), juri.krustok@ttu.ee (J. Krustok).

## 2. Experimental

CZTS monograins were synthesized from binaries and elemental S in molten flux by isothermal recrystallization process. The details of the monograin growth technology can be found elsewhere [18]. MGL solar cells with structure: graphite/MGL/CdS/ZnO/glass, were made from powder crystals with a diameter of 56–63 μm as selected by sieving. The analysis area of the solar cell is determined by the back contact area which is typically about 0.04 cm². More details about the solar cell preparation can be found in [19].

For the temperature dependent J–V and EQE measurements solar cells were mounted in a closed cycle He cryostat. J–V measurements were done by decreasing the temperature while EQE measurements were done by increasing the temperature in the range $T = 10$–300 K. For EQE measurements the generated photocurrent was detected at 0 V bias voltage. 250 W standard halogen lamp with calibrated intensity (100 mW cm⁻²) was used as a light source and spectrally neutral net filters for intensity dependence.

## 3. Results and discussion

Room temperature J–V characteristics of a studied CZTS-based MGL solar cell showed the following properties: open-circuit voltage $V_{oc} = 709$ mV, short-circuit current density $J_{sc} = 13.8$ mA/cm², fill factor $FF = 61.4\%$, and efficiency $\eta = 6.0\%$. Due to the peculiarity of the MGL solar cell structure, the active area where the photocurrent is actually produced is smaller than the analysis area. The active area is estimated to be 75% of the back contact area after excluding the area of the binder material between the absorber material powder crystals. After such consideration the current density per absorber material active area is estimated to be $J_{sc}^{abs.} = 18.4$ mA/cm² and the efficiency is estimated to be $\eta^{abs} = 8.0\%$. In spite of that, solar cell parameters are still limited due to recombination and parasitic losses. The series resistances obtained from the light and the dark J–V curves determined at room temperature by the process described by Hegedus and Shafarman [20] are rather high, $R_s^{light} = 3.6$ Ω cm² and $R_s^{dark} = 4.5$ Ω cm², accordingly.

The thermal behavior of the $V_{oc}$ under different light intensities is shown in Fig. 1. It is known [21] that the temperature dependence of $V_{oc}$ near room temperature can be presented as

$$V_{OC} = \frac{E_A}{q} - \frac{nkT}{q} \ln\left[\frac{I_{00}}{I_L}\right], \tag{1}$$

where $E_A$, $n$, $k$, $I_{00}$, and $I_L$ are the activation energy, diode ideality factor, Boltzmann constant, reverse saturation current prefactor, and the photocurrent, respectively. In general, the activation energy $E_A$ and also $I_{00}$ depend mainly on the dominating recombination mechanism in the solar cell. In case of bulk recombination $E_A \approx E_g$, where $E_g$ is the bandgap energy of the absorber material. The bandgap energy of CZTS slightly depends on the type of crystal structure [12], but is usually higher than 1.5 eV. In our sample $E_A \approx 1.26$ eV was determined from the $V_{oc}$ (T) plot (see Fig. 1). In general, according to the theory [22] in case of $E_A < E_g$, the interface recombination is a dominating recombination.

The temperature dependence of the series resistance $R_s$ found using Fig. 2 is shown in Fig. 3a where three different regions can be distinguished. At temperatures $T > 90$ K (region I) $R_s$ decreases with increasing temperature indicating the thermal activation of carriers [23]. In this region, the $R_s$ can be presented as:

$$R_S = R_{S0} \exp(E_A/kT) \tag{2}$$

where the exponential prefactor $R_{S0}$ contains all parameters that are independent or weekly dependent on temperature. Using Eq. (2) the activation energies $E_{A,d} = 87 \pm 3$ meV and $E_{A,l} = 43 \pm 1$ meV for dark and light curves were found, respectively. These activation energies are in the same range as found in [6,8,24]. At intermediate temperatures ($T = 90$–40 K, region II), the dependence of the series resistance on temperature changes and a typical Mott's variable-range hopping (VRH) conduction starts to dominate [25]. This type of behavior is expected in all heavily doped materials where spatial potential fluctuations create deep potential wells for holes [6,26,27]. At the same time, we also expect the increasing role of bulk recombination in this temperature region and therefore the VRH model is not completely valid here. At about $T = 40$ K, a rapid change of $R_s$ can be seen. In low temperature region ($T < 40$ K, region III), $R_s$ drops down more than one order of magnitude and remains almost constant down to the lowest measured temperature. At these very low temperatures, generated holes are not able to tunnel through the potential barrier into the interface region between CZTS and CdS and therefore the interface recombination rate must be very low.

Quantum efficiency measurement is a well-known method to describe optical and electronic losses in solar cell devices. From the low-energy side of the EQE curve i.e. near the bandgap energy $E \approx E_g$, the effective bandgap energy $E_g^*$ can be determined [17] by using an approximation proposed by Klenk and Schock [28]:

$$EQE \approx K\alpha L_{eff} \approx A\left(E - E_g^*\right)^{1/2}/E \tag{3}$$

where constant $A$ includes all energy independent parameters, $L_{eff} = w + L_d$ is the effective diffusion length of minority carriers, $L_d$ is their diffusion length in the absorber material, $w$ is the width of the depletion region, and $\alpha$ is the absorption coefficient of the absorber material. The constant $K$ is unity in absolute measurements. Consequently, the $E_g^*$ value can be determined from a plot of
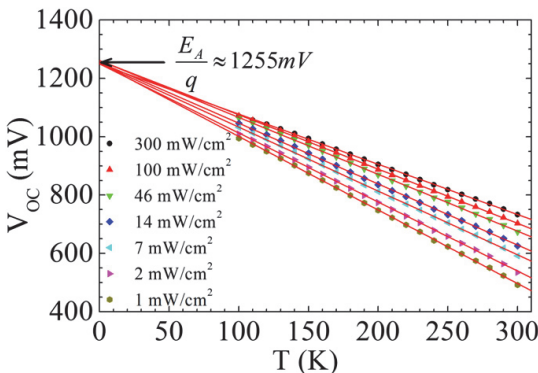


**Fig. 1.** Temperature dependence of $V_{oc}$ measured at different light intensities.
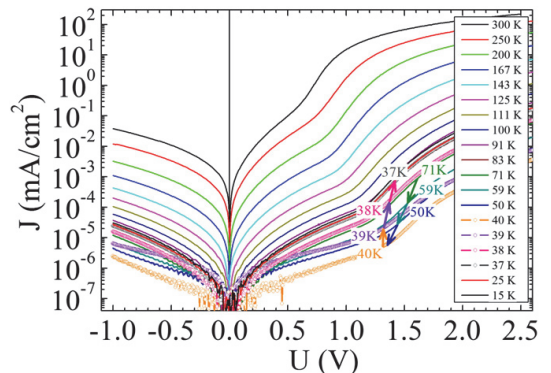


**Fig. 2.** Temperature dependence of dark J–V curves.
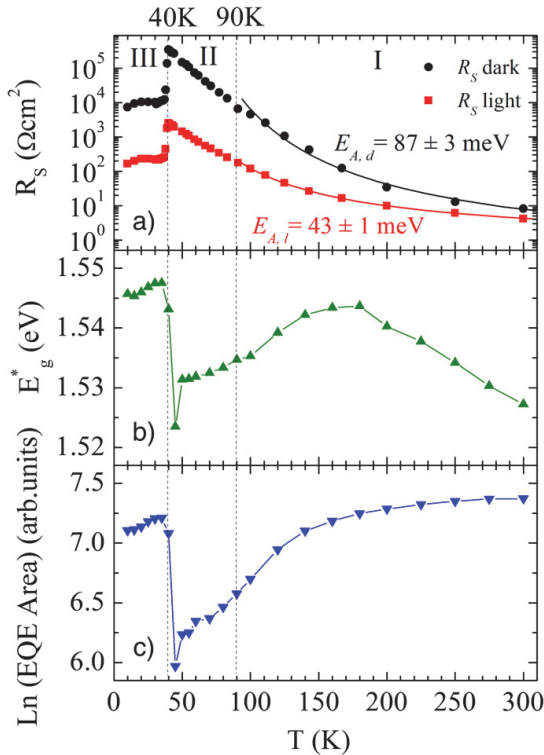
**Fig. 3.** Temperature dependencies of the series resistance $R_s$ obtained from the dark and light J–V curves (a), the effective bandgap energy $E_g^*$ (b), and integrated EQE area (c). Solid lines correspond to the fitting of Eq. (3) to the experimental data.

$(E \cdot EQE)^2$ vs. $E$ at the low energy side of the EQE spectrum. Therefore, temperature dependence of a quantum efficiency curve presented in Fig. 4 can be used to analyze the temperature dependence of the effective bandgap energy.

The temperature dependencies of the series resistance $R_s$, the effective bandgap energy $E_g^*$ and the integrated EQE are presented in Fig. 3. It can be seen (Fig. 3b) that in the temperature region from room
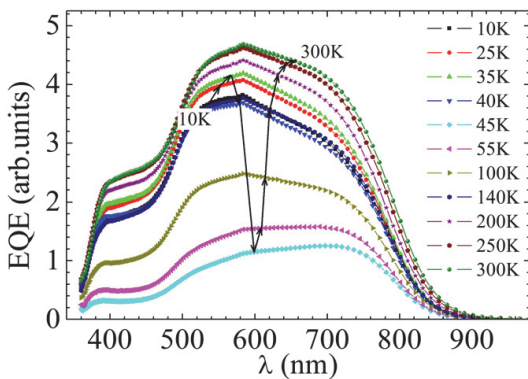


**Fig. 4.** Temperature dependence of EQE at 0 V. The arrows guide the trend of the EQE temperature dependence.

temperature to $T = 180$ K, $E_g^*$ follows the model of temperature dependence of the bandgap energy proposed by K.P. O'Donnell and X. Chen [29]. Then $E_g^*$ starts to decrease with further decreasing of the temperature until the "critical" temperature at about 40 K where the rapid increase of $E_g^*$ starts. Similar behavior can be seen for integrated EQE, see Fig. 3c. It was shown in [17] that the changes at 40 K < T < 180 K are related to localization of holes inside deep valence band potential wells. As a result, an exponential Urbach tail starts to affect the absorption and the effective bandgap $E_g^*$ starts to decrease due to holes localization in deeper potential wells. At the same time the hole mobility also decreases and the bulk recombination through these deep wells increases reducing the overall EQE. The observed sudden increase of $E_g^*$ to the "normal" bandgap value $E_g$ at 40 K together with the increase of the generated current (EQE) and decrease in $R_s$ has to be related to the step-like change in the Fermi level position at the interface. This change could cause the blocking of hole transport to the interface states and as a result the interface recombination decreases. This is why the photocurrent and $E_g^*$ increase. However, there might be also other processes taking place causing the same kind of behavior. Consequently further studies are needed to explain this peculiar behavior of the CZTS solar cell parameters at very low temperatures.

## 4. Conclusions

Temperature dependence of CZTS solar cell parameters was measured in the range of $T = 10$–300 K. It was shown that main recombination losses are related to interface recombination that was found to be blocked at $T < 40$ K. Part of the losses originate also from bulk recombination and is associated to potential fluctuations of the valence band edge.

## Acknowledgments

## References

[1] B. Shin, O. Gunawan, Y. Zhu, N.A. Bojarczuk, S.J. Chey, S. Guha, Thin film solar cell with 8.4% power conversion efficiency using an earth-abundant Cu₂ZnSnS₄ absorber, Prog. Photovolt. Res. Appl. 21 (2013) 72.
[2] W. Wang, M.T. Winkler, O. Gunawan, T. Gokmen, T.K. Todorov, Y. Zhu, D.B. Mitzi, Device characteristics of CZTSSe thin-film solar cells with 12.6% efficiency, Adv. Energy Mater. 4 (2013) 1301465.
[3] K. Wang, O. Gunawan, T. Todorov, B. Shin, S.J. Chey, N.A. Bojarczuk, D. Mitzi, S. Guha, Thermally evaporated Cu₂ZnSnS₄ solar cells, Appl. Phys. Lett. 97 (2010) 143508.
[4] O. Gunawan, T. Todorov, D. Mitzi, Loss mechanisms in hydrazine-processed Cu2ZnSn(Se, S)4 solar cells, Appl. Phys. Lett. 97 (2010) 233506.
[5] M. Grossberg, P. Salu, J. Raudoja, J. Krustok, Microphotoluminescence study of Cu₂ZnSnS₄ polycrystals, J. Photonics Energy 3 (2013) 030599.
[6] V. Kosyak, M.A. Karmarkar, M.A. Scarpulla, Temperature dependent conductivity of polycrystalline Cu₂ZnSnS₄ thin films, Appl. Phys. Lett. 100 (2012) 263903.
[7] M.A. Majeed Khan, S. Kumar, M. Alhoshan, A.S. Al Dwayyan, Spray pyrolysed Cu₂ZnSnS₄ absorbing layer: a potential candidate for photovoltaic applications, Opt. Laser Technol. 49 (2013) 196.
[8] J.C. González, G.M. Ribeiro, E.R. Viana, P.A. Fernandes, P.M.P. Salomé, K. Gutiérrez, A. Abelenda, F.M. Matinaga, J.P. Leitão, A.F. da Cunha, Hopping conduction and persistent photoconductivity in Cu₂ZnSnS₄ thin films, J. Phys. D. Appl. Phys. 46 (2013) 155107.
[9] M. Guc, R. Caballero, K.G. Lisunov, N. López, E. Arushanov, J.M. Merino, M. León, Disorder and variable-range hopping conductivity in Cu₂ZnSnS₄ thin films prepared by flash evaporation and post-thermal treatment, J. Alloys Compd. 596 (2014) 140.
[10] S. Chen, J.-H. Yang, X.G. Gong, A. Walsh, S.-H. Wei, Intrinsic point defects and complexes in the quaternary kesterite semiconductor Cu₂ZnSnS₄, Phys. Rev. B 81 (2010) 245204.

[11] E. Kask, T. Raadik, M. Grossberg, R. Josepson, J. Krustok, Deep defects in $Cu_2ZnSnS_4$ monograin solar cells, Energy Procedia 10 (2011) 261.

[12] M. Grossberg, J. Krustok, J. Raudoja, T. Raadik, The role of structural properties on deep defect states in $Cu_2ZnSnS_4$ studied by photoluminescence spectroscopy, Appl. Phys. Lett. 101 (2012) 102102.

[13] S. Chen, L.-W. Wang, A. Walsh, X.G. Gong, S.-H. Wei, Abundance of $Cu_{Zn} + Sn_{Zn}$ and $2Cu_{Zn} + Sn_{Zn}$ defect clusters in kesterite solar cells, Appl. Phys. Lett. 101 (2012) 223901.

[14] M. Grossberg, T. Raadik, J. Raudoja, J. Krustok, Photoluminescence study of defect clusters in $Cu_2ZnSnS_4$ polycrystals, Curr. Appl. Phys. 14 (2014) 447.

[15] D. Huang, C. Persson, Band gap change induced by defect complexes in $Cu_2ZnSnS_4$, Thin Solid Films 535 (2013) 265.

[16] K.G. Lisunov, M. Guk, A. Nateprov, S. Levcenko, V. Tezlevan, E. Arushanov, Features of the acceptor band and properties of localized carriers from studies of the variable-range hopping conduction in single crystals of $p$-$Cu_2ZnSnS_4$, Sol. Energy Mater. Sol. Cells 112 (2013) 127.

[17] J. Krustok, R. Josepson, T. Raadik, M. Danilson, Potential fluctuations in $Cu_2ZnSnSe_4$ solar cells studied by temperature dependence of quantum efficiency curves, Physica B 405 (2010) 3186.

[18] K. Muska, M. Kauk, M. Grossberg, J. Raudoja, O. Volobujeva, Influence of compositional deviations on the properties of $Cu_2ZnSnSe_4$ monograin powders, Energy Procedia 10 (2011) 323.

[19] K. Muska, M. Kauk-Kuusik, M. Grossberg, M. Altosaar, M. Pilvet, T. Varema, K. Timmo, O. Volobujeva, A. Mere, Impact of $Cu_2ZnSn(Se_xS_{1-x})_4$ ($x = 0.3$) compositional ratios on the monograin powder properties and solar cells, Thin Solid Films 535 (2013) 35.

[20] S.S. Hegedus, W.N. Shafarman, Thin-film solar cells: device measurements and analysis, Prog. Photovolt. Res. Appl. 12 (2004) 155.

[21] J. Krustok, R. Josepson, M. Danilson, D. Meissner, Temperature dependence of $Cu_2ZnSn(Se_xS_{1-x})_4$ monograin solar cells, Sol. Energy 84 (2010) 379.

[22] V. Nadenau, U. Rau, A. Jasenek, H.W. Schock, Electronic properties of $CuGaSe_2$-based heterojunction solar cells. Part I. Transport analysis, J. Appl. Phys. 87 (2000) 584.

[23] J.T. Asubar, Y. Jinbo, N. Uchitomi, Impurity band conduction and negative magneto-resistance in $p$-$ZnSnAs_2$ thin films, Phys. Status Solidi C 6 (2009) 1158.

[24] P.A. Fernandes, P.M.P. Salome, A.F. Sartori, J. Malaquias, A.F. da Cunha, B.-A. Schubert, J.C. González, G.M. Ribeiro, Effects of sulphurization time on $Cu_2ZnSnS_4$ absorbers and thin films solar cells obtained from metallic precursors, Sol. Energy Mater. Sol. Cells 115 (2013) 157.

[25] N.F. Mott, Impurity band conduction. Experiment and theory. The metal–insulator transition in an impurity band, J. Phys. Colloques 37 (1976) C4.

[26] S. Siebentritt, N. Papathanasiou, M.Ch. Lux-Steiner, Potential fluctuations in compensated chalcopyrites, Physica B 831 (2006) 376.

[27] M. Grossberg, J. Krustok, J. Raudoja, K. Timmo, M. Altosaar, T. Raadik, Photoluminescence and Raman study of $Cu_2ZnSn(Se_xS_{1-x})_4$ monograins for photovoltaic applications, Thin Solid Films 519 (2011) 7403.

[28] R. Klenk, H.-W. Schock, W.H. Bloss, Photocurrent collection in thin film solar cells — calculation and characterization for $CuGaSe2/(Zn,Cd)S$, Proc. of the 12th EU PVSEC, 1994, p. 1588.

[29] K.P. O'Donnell, X. Chen, Temperature dependence of semiconductor band gaps, Appl. Phys. Lett. 58 (1991) 2924.

**Elulookirjeldus**

| | |
|---|---|
| Ees-ja perekonnanimi | Mati Danilson |
| Sünniaeg ja -koht | 25. september 1980, Võru |
| E-post | mati.danilson@ttu.ee |

Haridus  2005 – ... Tallinna Tehnikaülikool, Keemia- ja materjalitehnoloogia õppekava, doktorantuur.
2003 – 2005 Tallinna Tehnikaülikool, Keemia- ja materjalitehnoloogia teaduskond, Loodusteaduste Magister.
1999 – 2003 Tallinna Tehnikaülikool, Matemaatika–loodusteaduskond, Loodusteaduste Bakalaureus.
1987 – 1999 Võru Kesklinna Gümnaasium, kesk-Haridus.

Teenistuskäik  2006 – ... Tallinna Tehnikaülikool, Materjaliteaduse instituut, teadur.
2005 – 2006 Tallinna Tehnikaülikool, Materjaliteaduse instituut, erakorraline teadur.
2003 – 2005 Tallinna Tehnikaülikool, Materjaliteaduse instituut, insener.

Täiendõpe  13.11.2014 – 14.11.2014 Tallinn, 5th European Kesterite Workshop.
25.06.2014 – 27.06.2014 Helmholz Zentrum Berlin, Workshop on Analytical Tools for PV.
22.11.2012 – 23.11.2012 Luxembourg, 3rd European Kesterite Workshop.
24.11.2011 – 25.11.2011 Barcelona, 2nd European Kesterite Workshop.
20.06.2011 – 22.06.2011 Pühajärve, FMTDK suvekool "G. Tammanni osa kaasaegse tehnoloogia kujunemises".
18.11.2010 – 19.11.2010 Pärnu, FMTDK talvekool "Nanomaterjalid ja –tehnoloogiad".
28.06.2010 – 30.06.2010 Pühajärve, FMTDK suvekool "Funktsionaalsed materjalid ja tehnoloogiad".
11.06.2010 Strasbourg, E-MRS Young Scientist Tutorial on Characterization Techniques for Thin-Film Solar Cells.
16.10.2008 Uppsala, Nordic seminar on modeling of

CIGS devices.
26.05.2008 – 30.05.2008 Uppsala, International course on "Thin Film Deposition at the Nanoscale: Mechanisms and Applications.
26.06.2007 – 28.06.2007 Pühajärve, MMTDK suvekool "Funktsionaalsed materjalid".
03.10.2006 – 20.12.2006 Berliin, täiendõpe röntgenfotoelektronspektroskoopia meetod.
21.08.2006 – 25.08.2006 Pärnu, European Union Centre of Excellence in PV materials and Devices, "YSSS-2006 on PV".
22.11.2005 – 25.11.2005 Ispra, Fullspectrum and Solar electricity Joint Scientific Workshop on the Utilization of the Solar Spectrum.
juuni – juuli 2004, Varssavi, täiendõpe AS, DLTS, DLCP analüüsi meetodid.

| | |
|---|---|
| Tunnustused | 2014, SA Archimedes programm Kristjan Jaagu Välissõidu stipendium.<br>2010, ESF DoRa T8 programmi "Noorteadlaste osalemine rahvusvahelises teadmisteringluses" stipendium.<br>2009, World Federation of Scientists stipendium. |
| Kaitstud lõputööd | "CuInSe$_2$-l baseeruvate päikesepatareide karakteristikute uurimine", magistritöö, juhendaja prof. Jüri Krustok<br>"CuInSe$_2$ päikesepatareide mahtuvuslik spektroskoopia", bakalaureusetöö,<br>juhendaja prof. Jüri Krustok |

**Curriculum Vitae**

| | |
|---|---|
| First name and surname | Mati Danilson |
| Date and place of birth | 25. September 1980, Võru |
| E-mail | mati.danilson@ttu.ee |

Education

2005 – ... Tallinn University of Technology, Faculty of Chemical and Materials Technology, doctoral studies.
2003 – 2005 Tallinn University of Technology, Faculty of Chemical and Materials Technology, Master of Natural Sciences.
1999 – 2003 Tallinn University of Technology, Faculty of Science, Bachelor of Natural Sciences.
1987 – 1999 Võru Downtown High School, secondary education.

Employment

2006 – ... Tallinn University of Technology, Department of Materials Science, Researcher.
2005 – 2006 Tallinn University of Technology, Department of Materials Science, Extraordinary Researcher.
2003 – 2005 Tallinn University of Technology, Department of Materials Science, Engineer.

Training

13.11.2014 – 14.11.2014 Tallinn, 5th European Kesterite Workshop.
25.06.2014 – 27.06.2014 Helmholz Zentrum Berlin, Workshop on Analytical Tools for PV.
22.11.2012 – 23.11.2012 Luxembourg, 3rd European Kesterite Workshop.
24.11.2011 – 25.11.2011 Barcelona, 2nd European Kesterite Workshop.
20.06.2011 – 22.06.2011 Pühajärve, FMTDK Summer school "The part of G. Tammann in development of modern technology".
18.11.2010 – 19.11.2010 Pärnu, FMTDK Winter school "Nanomaterials and technologies".
28.06.2010 – 30.06.2010 Pühajärve, FMTDK Summer school "Functional materials and application".
11.06.2010 Strasbourg, E-MRS Young Scientist Tutorial on Characterization Techniques for Thin-Film Solar Cells.

| | 16.10.2008 Uppsala, Nordic seminar on modelling of CIGS devices. |
| --- | --- |
| | 26.05.2008 – 30.05.2008 Uppsala, International course on "Thin Film Deposition at the Nanoscale: Mechanisms and Applications. |
| | 26.06.2007 – 28.06.2007 Pühajärve, MMTDK Summer school "Functional materials". |
| | 03.10.2006 – 20.12.2006 Berliin, training X-ray Photoelectron Spectroscopy method. |
| | 21.08.2006 – 25.08.2006 Pärnu, European Union Centre of Excellence in PV materials and Devices, "YSSS-2006 on PV". |
| | 22.11.2005 – 25.11.2005 Ispra, Fullspectrum and Solar electricity Joint Scientific Workshop on the Utilization of the Solar Spectrum. |
| | juuni – juuli 2004, Warssav, training AS, DLTS, DLCP analysis methods. |
| Recognitions | 2014, SA Archimedes program Kristjan Jaak Scholarship grant for foreign visits. |
| | 2010, ESF DoRa T8 program "Participation of Young Researchers in the International Circulation of Knowledge" Scholarship. |
| | 2009, World Federation of Scientists stipend. |
| Defended dissertations | "Device characteristics of $CuInSe_2$ based solar cells", master's thesis, supervisor Prof. Jüri Krustok |
| | "Capacitance spectroscopy of CIS solar cells", bachelor's thesis, supervisor Prof. Jüri Krustok |

**List of publications**

1. **M. Danilson**, E. Kask, N. Pokharel, M. Grossberg, M. Kauk-Kuusik, T. Varema, J. Krustok, Temperature dependent current transport properties in $Cu_2ZnSnS_4$ solar cells. Thin Solid Films 582 (2015) 162−165.
2. M. Pilvet, M. Kauk-Kuusik, M. Altosaar, M. Grossberg, **M. Danilson**, K. Timmo, A. Mere, V. Mikli, Compositionally tunable structure and optical properties of $Cu_{1.85}(Cd_xZn_{1-x})_{1.1}SnS_{4.1}$ ($0 \leq x \leq 1$) monograin powders. Thin Solid Films 582 (2015) 180−183.
3. M. Kauk-Kuusik, K. Timmo, **M. Danilson**, M. Altosaar, M. Grossberg, K. Ernits, p–n junction improvements of $Cu_2ZnSnS_4$/CdS monograin layer solar cells. Applied Surface Science 357 (2015) 795−798.
4. O. Volobujeva, E. Mellikov, K. Timmo, **M. Danilson**, S. Bereznev, $Cu_2ZnSnSe_4$ films from binary precursors. Journal of Renewable and Sustainable Energy 5 (2013) 031618.
5. I. Oja Acik, V. Kiisk, M. Krunks, I. Sildos, A. Junolainen, **M. Danilson**, M. Mere, V. Mikli, Characterisation of samarium and nitrogen co-doped $TiO_2$ films prepared by chemical spray pyrolysis. Applied Surface Science 261 (2012) 735−741.
6. **M. Danilson**, M. Altosaar, M. Kauk, A. Katerski, J. Krustok, J. Raudoja, XPS study of CZTSSe monograin powders. Thin Solid Films 519 (21) (2011) 7407−7411.
7. E. Mellikov, M. Altosaar, J. Raudoja, K. Timmo, O. Volobujeva, M. Kauk, J. Krustok, T. Varema, M. Grossberg, **M. Danilson**, K. Muska, K. Ernits, F. Lehner, D. Meissner, $Cu_2(Zn_xSn_{2-x})(S_yS_{1-y})_4$ Monograin Materials for Photovoltaics. Materials Challenges in Alternative and Renewable Energy. Ceramic Transactions 224 (2011) 137−141.
8. K. Timmo, M. Altosaar, J. Raudoja, K. Muska, M. Kauk, M. Pilvet, T. Varema, **M. Danilson**, O. Volobujeva, E. Mellikov, Sulfur-containing $Cu_2ZnSnSe_4$ monograin powders for solar cells. Solar Energy Materials and Solar Cells, 94 (11) (2010) 1889−1892.
9. J. Krustok, R. Josepson, T. Raadik, **M. Danilson**, Potential fluctuations in $Cu_2ZnSnSe_4$ solar cells studied by temperature dependence of quantum efficiency curves. Physica B: Condensed Matter 405 (15) (2010) 3186−3189.
10. A. Katerski, **M. Danilson**, A. Mere, M. Krunks, Effect of the growth temperature on chemical composition of spray-deposited $CuInS_2$ thin films. Energy Procedia 2 (1) (2010) 103−107.
11. J. Krustok, R. Josepson, **M. Danilson**, D. Meissner, Temperature dependence of $Cu_2ZnSn(Se_xS_{1-x})_4$ monograin solar cells. Solar Energy 84 (3) (2010) 379−383.
12. K. Timmo, M. Altosaar, J. Raudoja, M. Grossberg, **M. Danilson**, O. Volobujeva, E. Mellikov, Chemical etching of $Cu_2ZnSn(S,Se)_4$ monograin powder. In: 35th IEEE Photovoltaic Specialists Conference,

Honolulu, HI, June 20-25, 2010: Conference Proceedings (2010) 1982−1985.

13. M. Kauk, K. Muska, M. Altosaar, **M. Danilson**, O. Volobujeva, T. Varema, ZnO Grown by Chemical Solution Deposition. In: Proceedings of the 35th IEEE Photovoltaics Specialists: 35th Photovoltaic Specialist Conference, Hawaii Convention Center Honolulu, Hawaii, June 20-25, 2010. IEEE (2010) 002452−002456.

14. E. Mellikov, M. Altosaar, J. Raudoja, K. Timmo, O. Volobujeva, M. Kauk, J. Krustok, T. Varema, M. Grossberg, **M. Danilson**, K. Muska, K. Ernits, F. Lehner, D. Meissner, $Cu_2(Zn_xSn_{2-x})(S_ySe_{1-y})_4$ monograin materials for photovoltaics. In: George G. Wicks, Jack Simon, Ragaiy Zidan, Edgar Lara-Curzio, Thad Adams, Jose Zayas, Abhi Karkamkar (Ed.). Materials Challenges in Alternative and Renewable Energy (2010) 137−142. The American Ceramic Society, Wiley-Blackwell. (Ceramic Transactions; 224).

15. I. Oja Acik, A. Junolainen, V. Mikli, **M. Danilson**, M. Krunks, Growth of ultra-thin $TiO_2$ films by spray pyrolysis on different substrates. Applied Surface Science 256 (5) (2009) 1391−1394.

16. E. Mellikov, D. Meissner, T. Varema, M. Altosaar, M. Kauk, O. Volobujeva, J. Raudoja, K. Timmo, **M. Danilson**, Monograin materials for solar cells. Solar Energy Materials and Solar Cells 93 (1) (2009) 65−69.

17. K. Ernits, K. Muska, M. Kauk, **M. Danilson**, J. Raudoja, T. Varema, O. Volobujeva, M. Altosaar, Chemical bath deposition of ZnS films using different Zn-salts. In: Physics Procedia: EMRS Spring meeting 2009, Strasbourg, France, 8 - 12 of June 2009. Elsevier, BP4-10.

18. M. Altosaar, J. Raudoja, K. Timmo, **M. Danilson**, M. Grossberg, J. Krustok, E. Mellikov, $Cu_2Zn_{1-x}Cd_xSn(Se_{1-y}S_y)_4$ solid solutions as absorber materials for solar cells. Physica Status Solidi A - Applications and Materials Science 205 (1) (2008) 167−170.

19. E. Mellikov, M. Altosaar, M. Krunks, J. Krustok, T. Varema, O. Volobujeva, M. Grossberg, L. Kaupmees, T. Dedova, K. Timmo, K. Ernits, J. Kois, I. Oja Acik, **M. Danilson**, S. Bereznev, Research in solar cell technologies at Tallinn University of Technology. Thin Solid Films 516 (20) (2008) 7125−7134.

20. M. Kauk, M. Altosaar, J. Raudoja, K. Timmo, T. Varema, **M. Danilson**, M. Grossberg, E. Mellikov, The influence of doping with donor type impurities on the properties of $CuInSe_2$. Physica Status Solidi (c) 5 (2) (2008) 609−611.

21. J. Krustok, M. Grossberg, A. Jagomägi, **M. Danilson**, J. Raudoja, Analysis of the edge emission of highly conductive $CuGaTe_2$. Thin Solid Films 515 (15) (2007) 6192−6195.

22. K. Timmo, M. Altosaar, J. Raudoja, E. Mellikov, T. Varema, **M. Danilson**, M. Grossberg, The effect of sodium doping to $CuInSe_2$ monograin powder properties. Thin Solid Films 15 (2007) 5887−5890.

23. M. Kauk, M. Altosaar, J. Raudoja, A. Jagomägi, **M. Danilson**, T. Varema, The performance of CuInSe$_2$ monograin layer solar cells with variable indium content. Thin Solid Films 515 (2007) 5880−5883.
24. A. Jagomägi, J. Krustok, M. Grossberg, **M. Danilson**, J. Raudoja, Deep defect related photoluminescence in heavily doped GuGaTe$_2$ crystals. Physica Status Solidi A-Applied Research 203 (5) (2006) 949−955.
25. J. Krustok, A. Jagomägi, M. Grossberg, J. Raudoja, **M. Danilson**, Photoluminescence properties of polycrystalline AgGaTe$_2$. Solar Energy Materials and Solar Cells 90 (13) (2006) 1973−1982.
26. M. Altosaar, J. Raudoja, K. Timmo, **M. Danilson**, M. Krunks, E. Mellikov, Cu$_2$ZnSnSe$_4$ Monograin Powders for Solar Cell Application. In: Conference Record of the 2006 IEEE 4th World Conference on Photovoltaic Energy Conversion: 4th World Conference on Photovoltaic Energy Conversion, Waikoloa, HI, MAY 07-12, 2006. IEEE Electron Devices Society, 468−470.
27. M. Altosaar, **M. Danilson**, M. Kauk, J. Krustok, E. Mellikov, J. Raudoja, K. Timmo, T. Varema, Further developments in CIS monograin layer solar cells technology. Solar Energy Materials and Solar Cells 87 (2005) 25−32.
28. A. Jagomagi, J. Krustok, J. Raudoja, M. Grossberg, I. Oja, M. Krunks, **M. Danilson**, Photoluminescence and Raman spectroscopy of polycrystalline AgInTe$_2$. Thin Solid Films 480 (2005) 246−249.
29. A. Jagomägi, J. Krustok, J. Raudoja, M. Grossberg, **M. Danilson**, Deep and edge photoluminescence emission of CuInTe$_2$. Physica Status Solidi (b) 237 (2) (2003) R3−R5.
30. A. Jagomägi, J. Krustok, J. Raudoja, M. Grossberg, **M. Danilson**, M. Yakushev, Photoluminescence studies of heavily doped CuInTe$_2$ crystals. Physica B: Condensed Matter 337 (2003) 369−374.

# DISSERTATIONS DEFENDED AT
# TALLINN UNIVERSITY OF TECHNOLOGY ON
## *NATURAL AND EXACT SCIENCES*

1. **Olav Kongas**. Nonlinear Dynamics in Modeling Cardiac Arrhytmias. 1998.

2. **Kalju Vanatalu**. Optimization of Processes of Microbial Biosynthesis of Isotopically Labeled Biomolecules and Their Complexes. 1999.

3. **Ahto Buldas**. An Algebraic Approach to the Structure of Graphs. 1999.

4. **Monika Drews**. A Metabolic Study of Insect Cells in Batch and Continuous Culture: Application of Chemostat and Turbidostat to the Production of Recombinant Proteins. 1999.

5. **Eola Valdre**. Endothelial-Specific Regulation of Vessel Formation: Role of Receptor Tyrosine Kinases. 2000.

6. **Kalju Lott**. Doping and Defect Thermodynamic Equilibrium in ZnS. 2000.

7. **Reet Koljak**. Novel Fatty Acid Dioxygenases from the Corals *Plexaura homomalla* and *Gersemia fruticosa*. 2001.

8. **Anne Paju**. Asymmetric oxidation of Prochiral and Racemic Ketones by Using Sharpless Catalyst. 2001.

9. **Marko Vendelin**. Cardiac Mechanoenergetics *in silico*. 2001.

10. **Pearu Peterson**. Multi-Soliton Interactions and the Inverse Problem of Wave Crest. 2001.

11. **Anne Menert**. Microcalorimetry of Anaerobic Digestion. 2001.

12. **Toomas Tiivel**. The Role of the Mitochondrial Outer Membrane in *in vivo* Regulation of Respiration in Normal Heart and Skeletal Muscle Cell. 2002.

13. **Olle Hints**. Ordovician Scolecodonts of Estonia and Neighbouring Areas: Taxonomy, Distribution, Palaeoecology, and Application. 2002.

14. **Jaak Nõlvak**. Chitinozoan Biostratigrapy in the Ordovician of Baltoscandia. 2002.

15. **Liivi Kluge**. On Algebraic Structure of Pre-Operad. 2002.

16. **Jaanus Lass**. Biosignal Interpretation: Study of Cardiac Arrhytmias and Electromagnetic Field Effects on Human Nervous System. 2002.

17. **Janek Peterson**. Synthesis, Structural Characterization and Modification of PAMAM Dendrimers. 2002.

18. **Merike Vaher**. Room Temperature Ionic Liquids as Background Electrolyte Additives in Capillary Electrophoresis. 2002.

19. **Valdek Mikli**. Electron Microscopy and Image Analysis Study of Powdered Hardmetal Materials and Optoelectronic Thin Films. 2003.

20. **Mart Viljus**. The Microstructure and Properties of Fine-Grained Cermets. 2003.

21. **Signe Kask**. Identification and Characterization of Dairy-Related *Lactobacillus*. 2003

22. **Tiiu-Mai Laht**. Influence of Microstructure of the Curd on Enzymatic and Microbiological Processes in Swiss-Type Cheese. 2003.

23. **Anne Kuusksalu**. 2–5A Synthetase in the Marine Sponge *Geodia cydonium*. 2003.

24. **Sergei Bereznev**. Solar Cells Based on Polycristalline Copper-Indium Chalcogenides and Conductive Polymers. 2003.

25. **Kadri Kriis**. Asymmetric Synthesis of $C_2$-Symmetric Bimorpholines and Their Application as Chiral Ligands in the Transfer Hydrogenation of Aromatic Ketones. 2004.

26. **Jekaterina Reut**. Polypyrrole Coatings on Conducting and Insulating Substracts. 2004.

27. **Sven Nõmm**. Realization and Identification of Discrete-Time Nonlinear Systems. 2004.

28. **Olga Kijatkina**. Deposition of Copper Indium Disulphide Films by Chemical Spray Pyrolysis. 2004.

29. **Gert Tamberg**. On Sampling Operators Defined by Rogosinski, Hann and Blackman Windows. 2004.

30. **Monika Übner**. Interaction of Humic Substances with Metal Cations. 2004.

31. **Kaarel Adamberg**. Growth Characteristics of Non-Starter Lactic Acid Bacteria from Cheese. 2004.

32. **Imre Vallikivi**. Lipase-Catalysed Reactions of Prostaglandins. 2004.

33. **Merike Peld**. Substituted Apatites as Sorbents for Heavy Metals. 2005.

34. **Vitali Syritski**. Study of Synthesis and Redox Switching of Polypyrrole and Poly(3,4-ethylenedioxythiophene) by Using *in-situ* Techniques. 2004.

35. **Lee Põllumaa**. Evaluation of Ecotoxicological Effects Related to Oil Shale Industry. 2004.

36. **Riina Aav**. Synthesis of 9,11-Secosterols Intermediates. 2005.

37. **Andres Braunbrück**. Wave Interaction in Weakly Inhomogeneous Materials. 2005.

38. **Robert Kitt**. Generalised Scale-Invariance in Financial Time Series. 2005.

39. **Juss Pavelson**. Mesoscale Physical Processes and the Related Impact on the Summer Nutrient Fields and Phytoplankton Blooms in the Western Gulf of Finland. 2005.

40. **Olari Ilison**. Solitons and Solitary Waves in Media with Higher Order Dispersive and Nonlinear Effects. 2005.

41. **Maksim Säkki**. Intermittency and Long-Range Structurization of Heart Rate. 2005.

42. **Enli Kiipli**. Modelling Seawater Chemistry of the East Baltic Basin in the Late Ordovician–Early Silurian. 2005.

43. **Igor Golovtsov**. Modification of Conductive Properties and Processability of Polyparaphenylene, Polypyrrole and polyaniline. 2005.

44. **Katrin Laos**. Interaction Between Furcellaran and the Globular Proteins (Bovine Serum Albumin β-Lactoglobulin). 2005.

45. **Arvo Mere**. Structural and Electrical Properties of Spray Deposited Copper Indium Disulphide Films for Solar Cells. 2006.

46. **Sille Ehala**. Development and Application of Various On- and Off-Line Analytical Methods for the Analysis of Bioactive Compounds. 2006.

47. **Maria Kulp**. Capillary Electrophoretic Monitoring of Biochemical Reaction Kinetics. 2006.

48. **Anu Aaspõllu.** Proteinases from *Vipera lebetina* Snake Venom Affecting Hemostasis. 2006.

49. **Lyudmila Chekulayeva**. Photosensitized Inactivation of Tumor Cells by Porphyrins and Chlorins. 2006.

50. **Merle Uudsemaa**. Quantum-Chemical Modeling of Solvated First Row Transition Metal Ions. 2006.

51. **Tagli Pitsi**. Nutrition Situation of Pre-School Children in Estonia from 1995 to 2004. 2006.

52. **Angela Ivask**. Luminescent Recombinant Sensor Bacteria for the Analysis of Bioavailable Heavy Metals. 2006.

53. **Tiina Lõugas**. Study on Physico-Chemical Properties and Some Bioactive Compounds of Sea Buckthorn (*Hippophae rhamnoides* L.). 2006.

54. **Kaja Kasemets**. Effect of Changing Environmental Conditions on the Fermentative Growth of *Saccharomyces cerevisae* S288C: Auxo-accelerostat Study. 2006.

55. **Ildar Nisamedtinov**. Application of $^{13}$C and Fluorescence Labeling in Metabolic Studies of *Saccharomyces* spp. 2006.

56. **Alar Leibak**. On Additive Generalisation of Voronoï's Theory of Perfect Forms over Algebraic Number Fields. 2006.

57. **Andri Jagomägi**. Photoluminescence of Chalcopyrite Tellurides. 2006.

58. **Tõnu Martma**. Application of Carbon Isotopes to the Study of the Ordovician and Silurian of the Baltic. 2006.

59. **Marit Kauk**. Chemical Composition of $CuInSe_2$ Monograin Powders for Solar Cell Application. 2006.

60. **Julia Kois**. Electrochemical Deposition of $CuInSe_2$ Thin Films for Photovoltaic Applications. 2006.

61. **Ilona Oja Açik**. Sol-Gel Deposition of Titanium Dioxide Films. 2007.

62. **Tiia Anmann**. Integrated and Organized Cellular Bioenergetic Systems in Heart and Brain. 2007.

63. **Katrin Trummal**. Purification, Characterization and Specificity Studies of Metalloproteinases from *Vipera lebetina* Snake Venom. 2007.

64. **Gennadi Lessin**. Biochemical Definition of Coastal Zone Using Numerical Modeling and Measurement Data. 2007.

65. **Enno Pais**. Inverse problems to determine non-homogeneous degenerate memory kernels in heat flow. 2007.

66. **Maria Borissova**. Capillary Electrophoresis on Alkylimidazolium Salts. 2007.

67. **Karin Valmsen**. Prostaglandin Synthesis in the Coral *Plexaura homomalla*: Control of Prostaglandin Stereochemistry at Carbon 15 by Cyclooxygenases. 2007.

68. **Kristjan Piirimäe**. Long-Term Changes of Nutrient Fluxes in the Drainage Basin of the Gulf of Finland – Application of the PolFlow Model. 2007.

69. **Tatjana Dedova**. Chemical Spray Pyrolysis Deposition of Zinc Sulfide Thin Films and Zinc Oxide Nanostructured Layers. 2007.

70. **Katrin Tomson**. Production of Labelled Recombinant Proteins in Fed-Batch Systems in *Escherichia coli*. 2007.

71. **Cecilia Sarmiento**. Suppressors of RNA Silencing in Plants. 2008.

72. **Vilja Mardla**. Inhibition of Platelet Aggregation with Combination of Antiplatelet Agents. 2008.

73. **Maie Bachmann**. Effect of Modulated Microwave Radiation on Human Resting Electroencephalographic Signal. 2008.

74. **Dan Hüvonen**. Terahertz Spectroscopy of Low-Dimensional Spin Systems. 2008.

75. **Ly Villo**. Stereoselective Chemoenzymatic Synthesis of Deoxy Sugar Esters Involving *Candida antarctica* Lipase B. 2008.

76. **Johan Anton**. Technology of Integrated Photoelasticity for Residual Stress Measurement in Glass Articles of Axisymmetric Shape. 2008.

77. **Olga Volobujeva**. SEM Study of Selenization of Different Thin Metallic Films. 2008.

78. **Artur Jõgi**. Synthesis of 4'-Substituted 2,3'-dideoxynucleoside Analogues. 2008.

79. **Mario Kadastik**. Doubly Charged Higgs Boson Decays and Implications on Neutrino Physics. 2008.

80. **Fernando Pérez-Caballero**. Carbon Aerogels from 5-Methylresorcinol-Formaldehyde Gels. 2008.

81. **Sirje Vaask**. The Comparability, Reproducibility and Validity of Estonian Food Consumption Surveys. 2008.

82. **Anna Menaker**. Electrosynthesized Conducting Polymers, Polypyrrole and Poly(3,4-ethylenedioxythiophene), for Molecular Imprinting. 2009.

83. **Lauri Ilison**. Solitons and Solitary Waves in Hierarchical Korteweg-de Vries Type Systems. 2009.

84. **Kaia Ernits**. Study of $In_2S_3$ and ZnS Thin Films Deposited by Ultrasonic Spray Pyrolysis and Chemical Deposition. 2009.

85. **Veljo Sinivee**. Portable Spectrometer for Ionizing Radiation "Gammamapper". 2009.

86. **Jüri Virkepu**. On Lagrange Formalism for Lie Theory and Operadic Harmonic Oscillator in Low Dimensions. 2009.

87. **Marko Piirsoo**. Deciphering Molecular Basis of Schwann Cell Development. 2009.

88. **Kati Helmja**. Determination of Phenolic Compounds and Their Antioxidative Capability in Plant Extracts. 2010.

89. **Merike Sõmera**. Sobemoviruses: Genomic Organization, Potential for Recombination and Necessity of P1 in Systemic Infection. 2010.

90. **Kristjan Laes**. Preparation and Impedance Spectroscopy of Hybrid Structures Based on $CuIn_3Se_5$ Photoabsorber. 2010.

91. **Kristin Lippur**. Asymmetric Synthesis of 2,2'-Bimorpholine and its 5,5'-Substituted Derivatives. 2010.

92. **Merike Luman**. Dialysis Dose and Nutrition Assessment by an Optical Method. 2010.

93. **Mihhail Berezovski**. Numerical Simulation of Wave Propagation in Heterogeneous and Microstructured Materials. 2010.

94. **Tamara Aid-Pavlidis**. Structure and Regulation of BDNF Gene. 2010.

95. **Olga Bragina**. The Role of Sonic Hedgehog Pathway in Neuro- and Tumorigenesis. 2010.

96. **Merle Randrüüt**. Wave Propagation in Microstructured Solids: Solitary and Periodic Waves. 2010.

97. **Marju Laars**. Asymmetric Organocatalytic Michael and Aldol Reactions Mediated by Cyclic Amines. 2010.

98. **Maarja Grossberg**. Optical Properties of Multinary Semiconductor Compounds for Photovoltaic Applications. 2010.

99. **Alla Maloverjan**. Vertebrate Homologues of Drosophila Fused Kinase and Their Role in Sonic Hedgehog Signalling Pathway. 2010.

100. **Priit Pruunsild**. Neuronal Activity-Dependent Transcription Factors and Regulation of Human *BDNF* Gene. 2010.

101. **Tatjana Knjazeva**. New Approaches in Capillary Electrophoresis for Separation and Study of Proteins. 2011.

102. **Atanas Katerski**. Chemical Composition of Sprayed Copper Indium Disulfide Films for Nanostructured Solar Cells. 2011.

103. **Kristi Timmo.** Formation of Properties of $CuInSe_2$ and $Cu_2ZnSn(S,Se)_4$ Monograin Powders Synthesized in Molten KI. 2011.

104. **Kert Tamm**. Wave Propagation and Interaction in Mindlin-Type Microstructured Solids: Numerical Simulation. 2011.

105. **Adrian Popp**. Ordovician Proetid Trilobites in Baltoscandia and Germany. 2011.

106. **Ove Pärn**. Sea Ice Deformation Events in the Gulf of Finland and This Impact on Shipping. 2011.

107. **Germo Väli**. Numerical Experiments on Matter Transport in the Baltic Sea. 2011.

108. **Andrus Seiman**. Point-of-Care Analyser Based on Capillary Electrophoresis. 2011.

109. **Olga Katargina**. Tick-Borne Pathogens Circulating in Estonia (Tick-Borne Encephalitis Virus, *Anaplasma phagocytophilum*, *Babesia* Species): Their Prevalence and Genetic Characterization. 2011.

110. **Ingrid Sumeri**. The Study of Probiotic Bacteria in Human Gastrointestinal Tract Simulator. 2011.

111. **Kairit Zovo**. Functional Characterization of Cellular Copper Proteome. 2011.

112. **Natalja Makarytsheva**. Analysis of Organic Species in Sediments and Soil by High Performance Separation Methods. 2011.

113. **Monika Mortimer**. Evaluation of the Biological Effects of Engineered Nanoparticles on Unicellular Pro- and Eukaryotic Organisms. 2011.

114. **Kersti Tepp**. Molecular System Bioenergetics of Cardiac Cells: Quantitative Analysis of Structure-Function Relationship. 2011.

115. **Anna-Liisa Peikolainen**. Organic Aerogels Based on 5-Methylresorcinol. 2011.

116. **Leeli Amon**. Palaeoecological Reconstruction of Late-Glacial Vegetation Dynamics in Eastern Baltic Area: A View Based on Plant Macrofossil Analysis. 2011.

117. **Tanel Peets**. Dispersion Analysis of Wave Motion in Microstructured Solids. 2011.

118. **Liina Kaupmees**. Selenization of Molybdenum as Contact Material in Solar Cells. 2011.

119. **Allan Olspert**. Properties of VPg and Coat Protein of Sobemoviruses. 2011.

120. **Kadri Koppel**. Food Category Appraisal Using Sensory Methods. 2011.

121. **Jelena Gorbatšova**. Development of Methods for CE Analysis of Plant Phenolics and Vitamins. 2011.

122. **Karin Viipsi**. Impact of EDTA and Humic Substances on the Removal of Cd and Zn from Aqueous Solutions by Apatite. 2012.

123. **David Schryer**. Metabolic Flux Analysis of Compartmentalized Systems Using Dynamic Isotopologue Modeling. 2012.

124. **Ardo Illaste**. Analysis of Molecular Movements in Cardiac Myocytes. 2012.

125. **Indrek Reile**. 3-Alkylcyclopentane-1,2-Diones in Asymmetric Oxidation and Alkylation Reactions. 2012.

126. **Tatjana Tamberg**. Some Classes of Finite 2-Groups and Their Endomorphism Semigroups. 2012.

127. **Taavi Liblik**. Variability of Thermohaline Structure in the Gulf of Finland in Summer. 2012.

128. **Priidik Lagemaa**. Operational Forecasting in Estonian Marine Waters. 2012.

129. **Andrei Errapart**. Photoelastic Tomography in Linear and Non-linear Approximation. 2012.

130. **Külliki Krabbi**. Biochemical Diagnosis of Classical Galactosemia and Mucopolysaccharidoses in Estonia. 2012.

131. **Kristel Kaseleht**. Identification of Aroma Compounds in Food using SPME-GC/MS and GC-Olfactometry. 2012.

132. **Kristel Kodar**. Immunoglobulin G Glycosylation Profiling in Patients with Gastric Cancer. 2012.

133. **Kai Rosin**. Solar Radiation and Wind as Agents of the Formation of the Radiation Regime in Water Bodies. 2012.

134. **Ann Tiiman**. Interactions of Alzheimer's Amyloid-Beta Peptides with Zn(II) and Cu(II) Ions. 2012.

135. **Olga Gavrilova**. Application and Elaboration of Accounting Approaches for Sustainable Development. 2012.

136. **Olesja Bondarenko**. Development of Bacterial Biosensors and Human Stem Cell-Based *In Vitro* Assays for the Toxicological Profiling of Synthetic Nanoparticles. 2012.

137. **Katri Muska**. Study of Composition and Thermal Treatments of Quaternary Compounds for Monograin Layer Solar Cells. 2012.

138. **Ranno Nahku**. Validation of Critical Factors for the Quantitative Characterization of Bacterial Physiology in Accelerostat Cultures. 2012.

139. **Petri-Jaan Lahtvee**. Quantitative Omics-level Analysis of Growth Rate Dependent Energy Metabolism in *Lactococcus lactis*. 2012.

140. **Kerti Orumets**. Molecular Mechanisms Controlling Intracellular Glutathione Levels in Baker's Yeast *Saccharomyces cerevisiae* and its Random Mutagenized Glutathione Over-Accumulating Isolate. 2012.

141. **Loreida Timberg**. Spice-Cured Sprats Ripening, Sensory Parameters Development, and Quality Indicators. 2012.

142. **Anna Mihhalevski**. Rye Sourdough Fermentation and Bread Stability. 2012.

143. **Liisa Arike**. Quantitative Proteomics of *Escherichia coli*: From Relative to Absolute Scale. 2012.

144. **Kairi Otto**. Deposition of $In_2S_3$ Thin Films by Chemical Spray Pyrolysis. 2012.

145. **Mari Sepp**. Functions of the Basic Helix-Loop-Helix Transcription Factor TCF4 in Health and Disease. 2012.

146. **Anna Suhhova**. Detection of the Effect of Weak Stressors on Human Resting Electroencephalographic Signal. 2012.

147. **Aram Kazarjan**. Development and Production of Extruded Food and Feed Products Containing Probiotic Microorganisms. 2012.

148. **Rivo Uiboupin**. Application of Remote Sensing Methods for the Investigation of Spatio-Temporal Variability of Sea Surface Temperature and Chlorophyll Fields in the Gulf of Finland. 2013.

149. **Tiina Kriščiunaite**. A Study of Milk Coagulability. 2013.

150. **Tuuli Levandi**. Comparative Study of Cereal Varieties by Analytical Separation Methods and Chemometrics. 2013.

151. **Natalja Kabanova**. Development of a Microcalorimetric Method for the Study of Fermentation Processes. 2013.

152. **Himani Khanduri**. Magnetic Properties of Functional Oxides. 2013.

153. **Julia Smirnova**. Investigation of Properties and Reaction Mechanisms of Redox-Active Proteins by ESI MS. 2013.

154. **Mervi Sepp**. Estimation of Diffusion Restrictions in Cardiomyocytes Using Kinetic Measurements. 2013.

155. **Kersti Jääger**. Differentiation and Heterogeneity of Mesenchymal Stem Cells. 2013.

156. **Victor Alari**. Multi-Scale Wind Wave Modeling in the Baltic Sea. 2013.

157. **Taavi Päll**. Studies of CD44 Hyaluronan Binding Domain as Novel Angiogenesis Inhibitor. 2013.

158. **Allan Niidu**. Synthesis of Cyclopentane and Tetrahydrofuran Derivatives. 2013.

159. **Julia Geller**. Detection and Genetic Characterization of *Borrelia* Species Circulating in Tick Population in Estonia. 2013.

160. **Irina Stulova**. The Effects of Milk Composition and Treatment on the Growth of Lactic Acid Bacteria. 2013.

161. **Jana Holmar**. Optical Method for Uric Acid Removal Assessment During Dialysis. 2013.

162. **Kerti Ausmees**. Synthesis of Heterobicyclo[3.2.0]heptane Derivatives *via* Multicomponent Cascade Reaction. 2013.

163. **Minna Varikmaa**. Structural and Functional Studies of Mitochondrial Respiration Regulation in Muscle Cells. 2013.

164. **Indrek Koppel**. Transcriptional Mechanisms of BDNF Gene Regulation. 2014.

165. **Kristjan Pilt**. Optical Pulse Wave Signal Analysis for Determination of Early Arterial Ageing in Diabetic Patients. 2014.

166. **Andres Anier**. Estimation of the Complexity of the Electroencephalogram for Brain Monitoring in Intensive Care. 2014.

167. **Toivo Kallaste**. Pyroclastic Sanidine in the Lower Palaeozoic Bentonites – A Tool for Regional Geological Correlations. 2014.

168. **Erki Kärber**. Properties of ZnO-nanorod/$In_2S_3$/$CuInS_2$ Solar Cell and the Constituent Layers Deposited by Chemical Spray Method. 2014.

169. **Julia Lehner**. Formation of $Cu_2ZnSnS_4$ and $Cu_2ZnSnSe_4$ by Chalcogenisation of Electrochemically Deposited Precursor Layers. 2014.

170. **Peep Pitk**. Protein- and Lipid-rich Solid Slaughterhouse Waste Anaerobic Co-digestion: Resource Analysis and Process Optimization. 2014.

171. **Kaspar Valgepea**. Absolute Quantitative Multi-omics Characterization of Specific Growth Rate-dependent Metabolism of *Escherichia coli*. 2014.

172. **Artur Noole**. Asymmetric Organocatalytic Synthesis of 3,3'-Disubstituted Oxindoles. 2014.

173. **Robert Tsanev**. Identification and Structure-Functional Characterisation of the Gene Transcriptional Repressor Domain of Human Gli Proteins. 2014.

174. **Dmitri Kartofelev**. Nonlinear Sound Generation Mechanisms in Musical Acoustic. 2014.

175. **Sigrid Hade**. GIS Applications in the Studies of the Palaeozoic Graptolite Argillite and Landscape Change. 2014.

176. **Agne Velthut-Meikas**. Ovarian Follicle as the Environment of Oocyte Maturation: The Role of Granulosa Cells and Follicular Fluid at Pre-Ovulatory Development. 2014.

177. **Kristel Hälvin**. Determination of B-group Vitamins in Food Using an LC-MS Stable Isotope Dilution Assay. 2014.

178. **Mailis Päri**. Characterization of the Oligoadenylate Synthetase Subgroup from Phylum Porifera. 2014.

179. **Jekaterina Kazantseva**. Alternative Splicing of *TAF4*: A Dynamic Switch between Distinct Cell Functions. 2014.

180. **Jaanus Suurväli**. Regulator of G Protein Signalling 16 (RGS16): Functions in Immunity and Genomic Location in an Ancient MHC-Related Evolutionarily Conserved Synteny Group. 2014.

181. **Ene Viiard**. Diversity and Stability of Lactic Acid Bacteria During Rye Sourdough Propagation. 2014.

182. **Kristella Hansen**. Prostaglandin Synthesis in Marine Arthropods and Red Algae. 2014.

183. **Helike Lõhelaid**. Allene Oxide Synthase-lipoxygenase Pathway in Coral Stress Response. 2015.

184. **Normunds Stivrinš**. Postglacial Environmental Conditions, Vegetation Succession and Human Impact in Latvia. 2015.

185. **Mary-Liis Kütt**. Identification and Characterization of Bioactive Peptides with Antimicrobial and Immunoregulating Properties Derived from Bovine Colostrum and Milk. 2015.

186. **Kazbulat Šogenov**. Petrophysical Models of the $CO_2$ Plume at Prospective Storage Sites in the Baltic Basin. 2015.

187. **Taavi Raadik**. Application of Modulation Spectroscopy Methods in Photovoltaic Materials Research. 2015.

188. **Reio Põder**. Study of Oxygen Vacancy Dynamics in Sc-doped Ceria with NMR Techniques. 2015.

189. **Sven Siir**. Internal Geochemical Stratification of Bentonites (Altered Volcanic Ash Beds) and its Interpretation. 2015.

190. **Kaur Jaanson**. Novel Transgenic Models Based on Bacterial Artificial Chromosomes for Studying BDNF Gene Regulation. 2015.

191. **Niina Karro**. Analysis of ADP Compartmentation in Cardiomyocytes and Its Role in Protection Against Mitochondrial Permeability Transition Pore Opening. 2015.

192. **Piret Laht**. B-plexins Regulate the Maturation of Neurons Through Microtubule Dynamics. 2015.

193. **Sergei Žari**. Organocatalytic Asymmetric Addition to Unsaturated 1,4-Dicarbonyl Compounds. 2015.

194. **Natalja Buhhalko**. Processes Influencing the Spatio-temporal Dynamics of Nutrients and Phytoplankton in Summer in the Gulf of Finland, Baltic Sea. 2015.

195. **Natalia Maticiuc**. Mechanism of Changes in the Properties of Chemically Deposited CdS Thin Films Induced by Thermal Annealing. 2015.

196. **Mario Öeren**. Computational Study of Cyclohexylhemicucurbiturils. 2015.

197. **Mari Kalda**. Mechanoenergetics of a Single Cardiomyocyte. 2015.

198. **Ieva Grudzinska**. Diatom Stratigraphy and Relative Sea Level Changes of the Eastern Baltic Sea over the Holocene. 2015.

199. **Anna Kazantseva**. Alternative Splicing in Health and Disease. 2015.

200. **Jana Kazarjan**. Investigation of Endogenous Antioxidants and Their Synthetic Analogues by Capillary Electrophoresis. 2016.

201. **Maria Safonova**. SnS Thin Films Deposition by Chemical Solution Method and Characterization. 2016.

202. **Jekaterina Mazina**. Detection of Psycho- and Bioactive Drugs in Different Sample Matrices by Fluorescence Spectroscopy and Capillary Electrophoresis. 2016.